DOTTORATO DI RICERCA IN
ATOMIC AND MOLECULAR PHOTONICS

International Ph.D. - CICLO XXVII

Excited State Dynamics of Carbonyl Carotenoids Investigated by Ultrafast Vibrational and Electronic Spectroscopies

Settore Scientifico Disciplinare CHIM/02

Dottorando

Ragnoni Elena

Tutore e Co-tutore

Prof. *Foggi Paolo*

Dott. Di Donato Mariangela

Coordinatore

Prof. Righini Roberto

Anni 2012/2014

Contents

Introduction

In the last decades private industries as well as public funds have supported many laboratory research activities on solar energy all over the world, in order to provide an alternative source of energy to carbon fossils and satisfy the increasing energy demand. The overall amount of energy the Sun leaves on Earth is well above human consumption, but its conversion in electricity is limited to the visible spectral range and at has low efficiency. Likely, solar power could never provide all the electrical supply each country needs, but in combination with other green and renewable resources like wind, geothermal gases, biomasses and hydroelectric power a remarkable decrease of carbon fossil exploitation is possible.

Solar energy is nowadays transformed in several ways: from photovoltaic (PV) devices, in which the radiative energy is directly transformed in electricity, to thermal systems, where sun light collectors increase the temperature of a mineral oil up to gasification, thus activating turbine engines for elec-

tricity production. Nowadays commercial PV panels, made of mono-crystalline Si wafers, have an efficiency (calculated as produced electrical power divided by the absorbed sun energy intensity per panel unit) close to 15% and an average lifetime of 30 years.[1] Despite the large-scale production, their costs are still not competitive with carbon fossil fuels, thus further improvements on their efficiency and long-time stability are needed.

Several hypothesis are under study.[2] On the inorganic side, improvements are expected from the substitution of the Si wafers with thin films of less expensive CdTe and $CuInSe_2$ and from the modification of the solar cell morphology, from single wafer to multi n-p junctions (presently the best laboratory efficiency is around 30%). However, the most promising alternatives in transforming sun energy mix the organic and the inorganic fields. Hybrid technologies involve new knowledge in nano-science, conductive polymers and bio-molecular science. A deep knowledge on the electronic and dynamical properties of natural pigments may help in mimicking the natural photosynthesis processes of light-harvesting, energy transfer, charge separation and energy storage[3,4]. If natural or artificial dyes, with optimal characteristics in all these processes, were found, they could be used as sensitizer in polymeric or solid semi-conductive matrices, as already implemented in Grätzel solar cells to functionalize nano-particles of TiO_2.[5] The first dye-sensitized solar cells (DSSC) have

been realized in 1991 and their production has been rapidly industrialized because of their lightweight and flexibility in terms of materials they are made of. Dye-sensitized materials could find in a close future wide application: from small rechargeable electronic devices to eco-friendly houses and self-powered design elements.

In this Ph.D. thesis, the attention has been focussed on the electronic properties and the relaxation dynamics of a selected class of natural pigments: the carbonyl carotenoids.

Carotenoids are present in all antenna protein complexes and act mainly as accessory light harvesting pigments of chlorophylls, since they absorb the blue-green visible region of the solar spectrum, or as photo-activity regulator and photo-protector against free radicals and harmful singlet oxygen. In many marine algae proteins, however, a larger number of carbonyl carotenoids than chlorophylls has been detected, like in the Peridinin-Chlorophyll a-Protein (PCP) complex of the dinoflagellate *Amphidinium Carterae*[6], suggesting a key-role of this pigment in light-harvesting and a high efficient energy transfer to the photosynthetic reaction center. These simple organisms live in low-illumination conditions, and their photosynthetic apparatus has evolved to absorb in the blue-green spectral region, being the red-most part of the solar spectrum strongly absorbed by water. An energy transfer efficiency approaching the 90% has been ob-

served in PCP,[7–9] so that there is an increasing interest in exploiting carotenoids as dye-sensitizers or as donor groups in artificial push-pull compounds. However, the photo-dynamics of carbonyl carotenoids is not yet fully understood. Contrarily to non-polar carotenoids (such as the *all* trans β-carotene, see figure), the excited state lifetime of carbonyl carotenoids is very sensitive to the polarity of the environment. Furthermore, many of the naturally occurring carbonyl carotenoids present more than a polar functional group, thus complicating the symmetry of their chemical structure and the electronic properties of their excited states.

In case of natural antennas, significant insights about the role of the protein environment in determining the energy transfer properties of the system was gained from high temporal resolution pump-probe measurements. It is known from previous studies,[10] that specific pigment-protein interactions as well as the dielectric heterogeneity of the protein domains are important to tune the pigment site energies and influence the energy transfer. The high level of organization in terms of displacement and orientation of the chromophores within proteins and of the antennas around reaction centers, certainly, has an influence on the observed high efficiency of energy transfer.

In this thesis, as a preliminary step towards the analysis of the photo-dynamics of Peridinin, we considered a sim-

pler molecule, the trans-β-apo-8'-carotenal. This carotenoid presents a single carbonyl group, what allows us to investigate the effects of the polyene chain symmetry breakdown on the excited state relaxation dynamics, and to clarify the influence of the external medium polarity. Then we analyzed the photo-dynamics of Peridinin in several solvents, using time resolved spectroscopies mostly based on the use of infrared pulses.

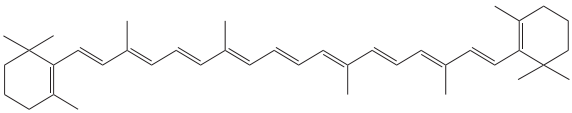

1) *all* trans beta-carotene

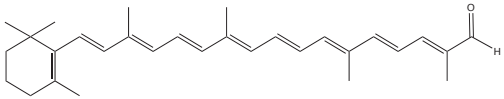

2) *all* trans beta-apo-8'-carotenal

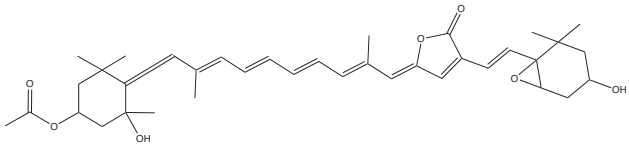

3) Peridinin

The thesis is organized as follows: a brief description of the photosynthetic apparatus and of the pigment properties is reported in chapter 1; the second chapter outlines some theoretical aspects regarding the spectroscopic techniques and describes the instrumental set-ups. The experimental results on the analyzed carbonyl carotenoids, namely the *all* trans-β-apo-8'-carotenal and Peridinin, are presented and discussed in chapters 3 and 4, respectively. Finally, a model that explains the experimental evidences, including polarity and polarizability solvation effects, is proposed in chapter 5.

1 The Photosynthesis

$$6\,CO_2 + 12\,H_2O \underset{\text{cellrespiration}}{\overset{\text{photosynthesis}}{\rightleftharpoons}} C_6H_{12}O_6 + 6\,O_2 + 6\,H_2O$$

Scheme 1

Photosynthesis is the basic process allowing plants and microorganisms (e.g. algae and bacteria) to convert light into chemical energy. The photosynthetic organisms are able to store the harvested light in the chemical bonds of ATP, which drives the synthesis of glucose, essential for their sustainment. In this way, they fix carbon atoms of CO_2 molecules of the air and deliver O_2 as a side product. The overall process is a reduction-oxidation reaction, in which carbon atoms of CO_2 molecules are reduced and oxygen atoms of water are oxidized. The opposite eso-ergodic reaction is the cellular respiration, in which the biochemical energy of nutrients (the glucose) is converted in ATP, NADPH or equivalent cell en-

ergy carriers. In both processes, the overall chemical reaction shown in scheme 1 hides several steps.

The photosynthesis is usually divided in two stages: in the first *light-dependent reactions* stage several pigments harvest sunlight and funnel the energy to the reaction center, where the first photo-induced charge separation starts the electron transportation chain. The latter process ends up in the reduction of a $NADP^+$ molecule and in the activation of the ATP-synthase by the transmembrane electro-chemical potential. In the second *dark reactions* stage, these molecules provide the energy to fix three CO_2 molecules in the glyceraldehyde 3-phosphate (G3P), the metabolic intermediate of a glucose molecule. This second stage is also known as Calvin Cycle or C3 cycle in plants and green algae. In the following, we will focus on the first stage.

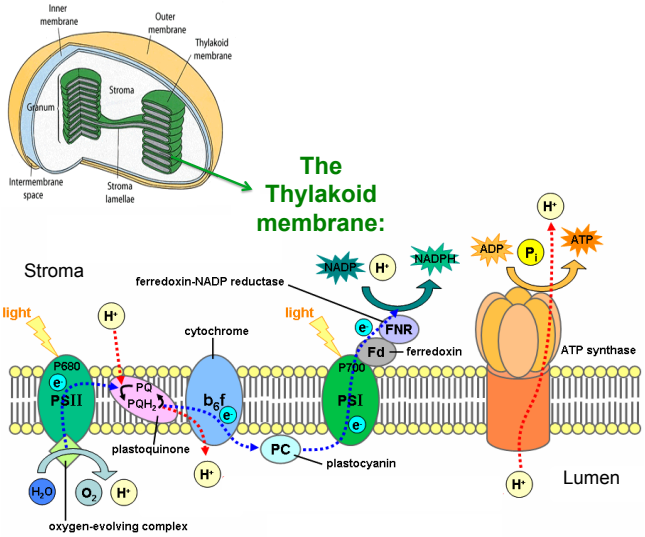

Figure 1.1: Schematic view of a chloroplast and the thylakoid membrane.

Photosynthetic reactions occur inside chloroplasts (figure 1.1), the engine-subunits of vegetal cells, like mitochondria in animal cells. This organelle has two external membranes which contain a semi-gel fluid called *stroma*, where thylakoid membranes organized in grana and lamellae float. While the Calvin cycle takes place in the stroma, most part of the bright reactions happen in embedded proteins of the thylakoid membrane. These large protein complexes are, in the order, the

photosystem II (PSII), a cytochrome complex responsible of the transmembrane electrochemical potential, the photosystem I (PSI) and the ATP-synthase. The cytochrome is directly involved in the electron transportation chain from PSII to PSI, together with the plastoquinone pool and the plastocyanin protein. This redox reactions cascade activates a protonic pump which transfers H^+ from the stroma to the inner thylakoid space, the *lumen*. As a consequence of the electrochemical gradient between the two faces of the membrane, H^+ ions pass back to the stroma through the channel of the ATP-synthase, thus activating the phosphorylation of an ADP molecule. In this way, part of the initial photon energy, which seems to be lost along the electron chain, is recovered.

Figure 1.1 reports the characteristic scheme of the thylakoid membrane of the oxygenic photosynthesis of green plants, however, in many algae and bacteria, photosynthetic reactions take place even in the absence of water, thus without producing oxygen. Photosystems I and II are very similar protein complexes, composed of many antenna systems and coenzymes surrounding the central reaction center (RC) protein. Antenna complexes are rich of pigments, such as chlorophylls and carotenoids, which harvest light and transfer energy to the reaction center. Here, the so-called special pair P680 or P700 (respectively in the PSII and PSI of green plants), consisting of a dimer of Chl-a molecules, is excited

through energy transfer from nearby antennae or by direct absorption of photons at 680 and 700 nm. This energy activates a charge separation process, which finally results in the oxidation of the special pair and the reduction of a quinone molecule. The D1 and D2 domains of the RC protein are highly symmetric, with two pathways for electron transfer almost equivalent, however only the D1 domain results to be active.[11] Once excited, the special pair P680 transfers the electron to a Pheophytin (Ph) molecule, which has the same porphyrin structure of a Chlorophyll molecule with the central Magnesium ion replaced by two protons; then the charge passes to a primary tightly protein-bound quinone (Q_A) and finally to a second exchangeable one (Q_B). At each round, Q_B gains a negative charge and binds an H^+ ion taken from the stroma, increasing the electro-chemical transmembrane gradient. After two rounds, it leaves PSII as QH_2 and diffuses through the membrane to the cytochrome complex. The re-oxidation of QH_2 provides the energy for the transmembrane protonic transfer and the charge to oxidize a copper atom of the plastocyanin protein, which transports the electron to PSI. Here, the special pair P700 starts a sequence of electron transfer processes similar to those occurring in PSII. The charge finally proceeds to the Ferredoxin protein, attached to PSI on the stroma side, where the reduction of a $NADP^+$ molecule takes place. Up to now, it has not been explained how the charge recombination is avoided after the

first photo-induced separation charge in the $P680^+Ph^-$ complex. Even though thermodynamically favorited, the charge recombination does not take place because Ph^- transfers the electron to the close quinone Q_A faster than recombination. The remaining $P680^+$ is a strong oxidant, which extracts an electron from a protein attached on the lumen side called oxygen-evolving complex. The active site of this protein contains 4 atoms of Mn at different oxidation state and coordinates two water molecules. The electron extraction forced by the special-pair catalyzes the water splitting: every four electrons an oxygen molecule is produced and four H^+ are released on the lumen side.

In photosynthetic bacteria the thylakoid membrane structure is homologous to that of green plants, however the number of cofactors and coenzymes in each photosystem is smaller. Many antenna and reaction center photo-systems have been determined at atomic resolution.[12] (and ref. 139-140,154-156,159 therein). In purple and green bacteria D1 and D2 domains are historically named as M and L branches, with L as active branch. Bacterial special pairs are dimers of bacteriochlorophylls (BChl), which absorb around 800-900 nm, in a red-shifted region with respect to P680 and P700, likely due to stronger pigment-protein interactions in the bacterial RC. In the first photo-induced separation charge, a BChl mediates the charge transfer from the special pair to the bacterio-pheophytin (BPh).[13] The striking difference from

green plants is the way the electron is replaced in the special pair after the photo-induced separation. No water splitting coenzyme are attached to the reaction center, however a cytochrome type c provides the needed electron at each cycle, avoiding the charge recombination.

1.1 The Light-Harvesting Proteins

As seen in the previous paragraph, the PSII and PSI supercomplexes contain many proteins with different functionalities: from cytochromes involved in the electron chain transport up to the core reaction center surrounded by many light-harvesting (LH) antennae, which contain several chlorophylls and carotenoid chromophores. It has been observed through atomic force microscopy [14] that the number of the antenna systems per reaction center is strictly correlated with the available light and increases in low-light conditions, together with the overall cross-section of photon absorption. Indeed, in order to fully reduce the quinone Q_B two electrons are needed. Therefore, the photo-excitation rate of the RC must exceed a certain threshold to completely avoid charge recombination.

In order to optimize the light-harvesting, in highly evolved organisms such as green plants, antenna proteins can be dis-

tinguished in peripheral (LHCII and LHCI, respectively in the PSII and PSI), semi-peripheral (CP29, CP26 and CP24) and core antenna (CP43 and CP47) (figure 1.2), with different value of energy transfer yield toward the RC.[10,12] Bacterial photosystems are less complex, thus light harvesting proteins are simply distinguished in LH2 and LH1 proteins for the two photosystems. The antennas are either embedded across the phospholipid thylakoid membrane, or dissolved in water and chemically anchored on the lumen or on the stroma side of the membrane. Moreover these systems present a great variety in their 3D structures as well as in the inner disposition of their pigments (figure 1.3).

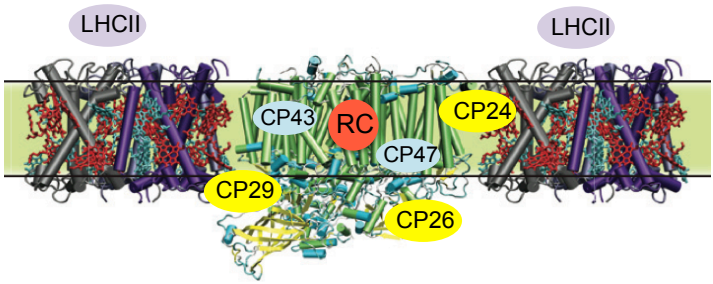

Figure 1.2: Light Harvesting Proteins in the Photosystem II supercomplex of green plants.

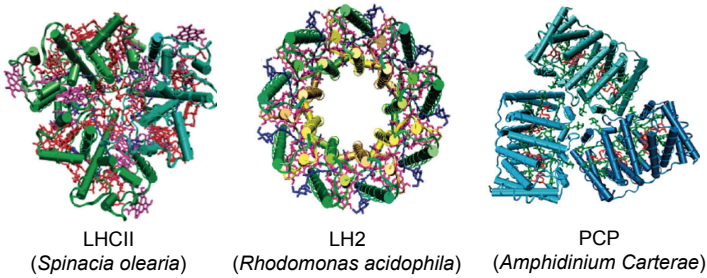

Figure 1.3: Structural variety of antenna proteins.

LH protein	Carotenoids
LHCII of *green plants*	Beta-carotene
	Lutein
	Violaxanthin
	Neoxanthin
	Zeaxanthin
LH2 *Rhodomonas acidophila*	Rhodopin glucoside
PCP *Amphidinium Carterae*	Peridinin

Table 1.1: Carotenoid contents of some LH complexes.

In light-harvesting complexes, chlorophylls are generally present in larger number than carotenoids, which mainly act as photo-protector against harmful oxygen singlet and chlorophyll triplet states[15–17] . One of the most studied photoprotective mechanisms is the non-photochemical quenching (NPQ)[18–20] in which the Chl fluorescence is quenched by the Xanthophyll Cycle. Here, a sequence of reactions triggered by the high-light conditions, converts violaxanthin in zeaxanthin, thus dissipating the excess of energy as thermal energy.

As reported in table 1.1, in plants different types of carotenoids are present within the LHCII protein[21]. They execute different functions and are not necessarily optimized for light-harvesting and energy-transfer. In bacteria, the type of carotenoid contained in LH complexes is different for each species. Since only one type of carotenoid is present, it is usually able to efficiently absorb light and transfer energy to BChlorophylls. The determination of the ET yield is here easier than in plant antennae: selective excitation of carotenoids is accessible since the visible absorption band around 400-550 nm results to be narrower and generally does not overlap with the BChl absorption below 400 nm (the so called Soret band). As reported in greater details in the next paragraph, the Car-Chl ET proceeds from both the first and the second carotenoid excited states, however, while in LHC protein family the main transfer pathway ($\sim 80\%$) is from the second excited state, in marine algae it originates from the

first excited state. Different type of ET mechanisms have been hypothesized accordingly to the different analyzed antenna systems.

1.1.1 The Peridinin-Chlorophyll a Protein

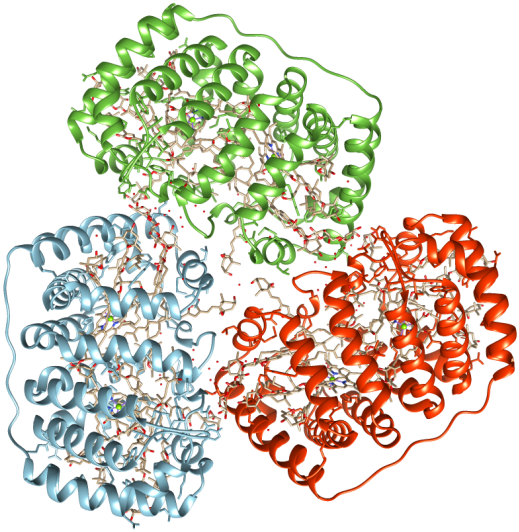

Figure 1.4: Trimeric structure of the water soluble PCP protein (PDB-ID: 1PPR).

Here we focus the attention on the Peridinin-Chlorophyll a Protein (PCP) reported in figure 1.4. The uniqueness of the PCP protein is in its chromophoric composition. The PCP protein is a water soluble protein extracted from the dinoflagellate *Amphidinium Carterae*, a unicellular organism that lives in under-illuminated conditions in tropic coastal waters, commonly found as phyto-plankton up to 20-30 m in depths. This protein contains only one type of carotenoid, the Peridinin, and in a larger number than Chlorophyll molecules. Therefore, Peridinin acts as primary light absorbers and transfers the energy to chlorophylls with a yield which has been found to reach 90% .[7–9] The X-ray structure of this protein was determined[6] at high resolution (2Å) in 1996; it reveals a trimeric form in which each monomeric unit contains two identical pseudo-twofold symmetric domains: in each domain 1 Chl-a and 4 Peridinin molecules are in Van der Waals contact through Peridinin conjugated chains and Chl-a tetrapyrrole ring (figure 1.5). Furthermore, Peridinins are two-by-two H-bonded across the two domains. It is worth pointing out that the quaternary structure of the all protein is based on a central water molecule, which coordinates three Peridinin molecules from each monomer through the OH groups placed on the terminal epoxy-ring.

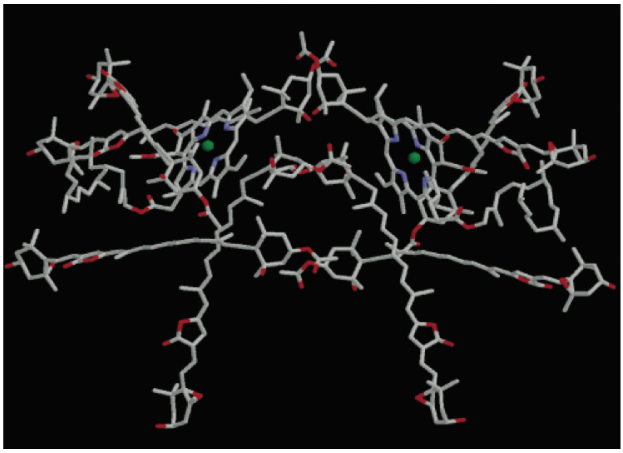

Figure 1.5: Symmetric two-fold disposition of 2 Chlorophyll-a and 8 Peridinin molecules in a monomer of PCP.

1.1.2 Energy-Transfer mechanisms in Light-Harvesting Proteins

In natural antennas pigments are generally geometrically arranged in the protein scaffold, but even when they seems to be randomly disposed their orientation and distance are optimized for ET.

Two mechanisms are generally invoked to explain ET: the Förster mechanism (or FRET, Förster Resonance Energy Trans-

fer), active when the inter-chromophoric distance is between 1 and 10 nm, and the Dexter mechanism, operating when molecules are in close Van der Waals contact (<10Å). Both mechanisms are non-radiative and their efficiency depends on the overlap integral of the donor fluorescence and acceptor absorption spectra. The substantial difference is the strength of the electronic coupling between the energy donor and the acceptor. In the Förster mechanism each molecule maintains its own electrons. This mechanism is based on the resonance between a donor and an acceptor molecule, which are dipole-dipole coupled. The maximum ET efficiency is reached when the fluorescence transition dipole moment of the donor and the absorption dipole moment of the acceptor are parallel, thus, generally, a geometrical disposition among pigments is preferred, considering also the $\frac{1}{r^6}$ dependence on the inter-chromophoric distance. In the Dexter mechanism, instead, molecules are in Van der Waals contact and a physical exchange of electrons between donor and acceptor molecules, in the excited and in the ground states, is possible.

Both mechanisms correspond to an incoherent hopping of energy, through electronic displacement or electron energy excitation resonance. Only very recently, the presence of quantum-mechanical electronic coherences has been observed thanks to development of new techniques as 2D-Electronic Spectroscopy (2D-ES). Analysis of coherent energy transfer in many photosynthetic systems is actually a cutting-edge

topic.[22–25]

1.2 Electronic properties of Carotenoids

Carotenoids are naturally occurring pigments characterized by a long conjugated carbon chain with conjugation length N = 7-13. They can be classified in xanthophylls, containing oxygen atoms, and neutral carotenes. Excited state properties of carotenoids largely depend on the chain conjugation length, on their molecular symmetry, on the presence of terminal β-rings and attached side-groups. The simplest energy level scheme used for carotenoids is based on the electronic properties of all-trans-polyenes with conjugation length N$\geq$ 7 (see Appendix)[26,27]. Their C_{2h} symmetry leads to a first singlet $S_1(2A_g^-)$ excited state, whose direct excitation from the $S_0({1A_g}^-)$ ground state is forbidden by selection rules. The visible band between 400 and 550 nm is therefore ascribed to the second singlet $S_2(1B_u^+)$ excited state, which rapidly relaxes via conical intersection to S_1 within a few hundred femtosecond (figure 1.6)[28].

Together with chlorophylls, carotenoids cover almost all the visible spectral range of the incident solar radiation on Earth. It is worth noting that carotenoids, absorbing the

green-blue light, cover the highest efficient part of the sun radiation scattering across deep water: $I_{scattering} \propto \frac{1}{\lambda^4}$. Figure 1.6 reports the absorption spectrum of a typical photosynthetic antenna. Besides carotenoids bands, Chlorophylls absorptions are also identifiable: a doublet Q_y peak around 700-850 nm, whose frequency position shifts according to the strong coupling between chlorophyll molecules arranged in different position inside the protein, a Q_x band around 600 nm and the Soret peak in the UV spectral region. In many cases, the carotenoid-chlorophyll ET yield is close to unity: as already mentioned, both S_2 and S_1 carotene excited states can be involved in the energy transfer, however there is also computational and experimental evidence that other dark states could take part to the ET, especially in the pigment-protein bound form.[23,27,29–31]

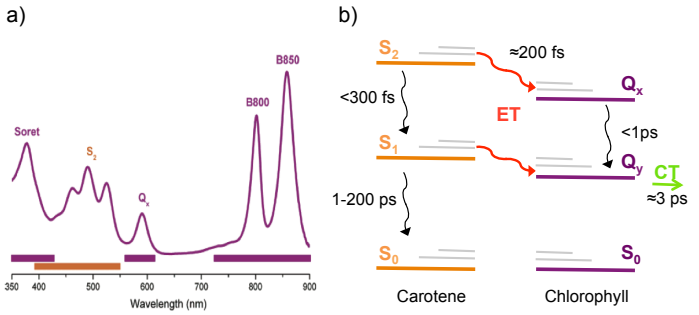

Figure 1.6: a) From ref. [12]: Vis absorption spectrum of the LH2 complex of Rps. Acidophila. Horizontal bars show spectral regions of carotenoid (orange) and chlorophyll (purple) absorption bands. **b)** Possible ET pathways from carotene to chlorophyll molecules. The CT arrow and the 3 ps time constant are proper of the charge separation in the special pair-Pheophitin complex.

To analyze the role of dark states in the ET and in the relaxation dynamics of carotenoids many quantum-mechanical (QM) calculations on carotenoid excited states have been carried on over decades, with increasing computational power and technical sophistication. [27,32] QM calculations pose substantial problems due to the very high electron correlation along the polyenic chain. When multiple excited configurations (IC) at the Franck Condon geometry are considered, $S_1(2A_g^-)$ and $S_2(1B_u^+)$ states loose their specific covalent and ionic characters and mix between them and with other con-

figurations. Considering only singly and doubly excited configurations is enough to push the $2A_g^-$ state below the $1B_u^+$ in carotenoids with N≥7. On the contrary, only if higher orders of interaction are included, the $1B_u^-$ and the $3A_g^-$ dark states, which supposedly lie close in energy to S_2 and S_1, exceed in energy S_2.[33]

Excited state wave-functions can be visualized in terms of molecular orbitals through the predominant configuration: in this sense the $S_0 \rightarrow S_2$ transition can be described as a single electron promotion from the HOMO to the LUMO state, while the $S_0 \rightarrow S_1$ transition as a double excitation of two electrons to the same state (note that the S_1 absorption is indeed two-photon allowed).[34,35]

Non-linear spectroscopies, like two-photon absorption or the pump-dump-probe technique, allow for the direct energy determination of S_1 state. First attempts to energetically localize S_1 were carried out by measuring Raman excitation profiles.[36] The visible excitation wavelength was scanned, looking for the amplified Resonant Raman signal of the C=C symmetric stretching. Steady-state fluorescence quantum yield and time-correlated single photon counting experiments were also performed.[37,38] The fluorescence quantum yields of carotenoids in solution are on the order of 10^{-5}, because of the forbidden nature of the S_1-S_0 transition, and decrease with increasing N. In carotenoids with conjugation length N≥ 8,

a clear switch to the S_2 fluorescence was observed[37], therefore a violation of the Kasha's rule. Both S_1 and S_2 energies decrease with increasing conjugation length, however the S_1 decrease is slightly steeper, so that the S_2-S_1 energy gap increases with N and the S_2 fluorescence overcomes that from S_1. Nevertheless, non-radiative S_2-S_1 and S_1-S_0 internal conversions, which follow the energy gap law[38], represent the main relaxation pathways, especially in longer carotenoids.

1.2.1 Carbonyl Carotenoids

While non-radiative relaxation dynamics of non-polar carotenoids are insensitive to solvent polarity, in carbonyl carotenoids the S_1 lifetime strongly decreases in polar solvents, going from hundreds of picoseconds to a few picoseconds.[39–43] The solvent dependence of the fluorescence lifetime of Peridinin was initially attributed to the presence of the lactone ring. However, the dependence of the S_1 lifetime on the solvent polarity was observed also in apocarotenals and dicyanoapocarotenes and attributed to the presence of an electron withdrawing substituent on the conjugated chain in an asymmetric position.[44,45]

Transient absorption measurement on a series of apocarotenals, differing for the conjugation length N, showed that the S_1 lifetime (τ) dependence on the polarity of the solvent increases with decreasing N.[46,47] Going from non-polar to polar solvents, τ decreases from 200 to 8 ps in apo-12'-carotenal (N=6), and from 25 to 8 ps in apo-8'-carotenal (N=8). Finally, no solvent polarity dependence (τ = 4-5 ps) is observed in apo-4'-carotenal (N=10). As for non-polar carotenoids, the internal conversion rate between low-lying excited states and the ground state increases with the chain length.

Dual fluorescence is also observed for carbonyl carotenoids;[46,48,49] it shows a predominance of the S_1 emission, inde-

pendently of the conjugation length. The fluorescence from S_1 increases with respect to that from S_2 at increasing solvent polarity,[49] although involved S_1 and S_0 states should be totally symmetric and insensitive to the solvent property in an idealized C_{2h} symmetry.

All these observations suggest the breakdown of the $2A_g^-$ symmetry in S_1 and the presence of an intramolecular charge transfer (ICT) character, induced by the electron withdrawing substituent. In polar carotenoids the low-lying state is generally referred as the S1/ICT state, however its exact electronic nature still remains unclear. Two are the hypothesis proposed: the existence of a separate dark singlet ICT state, coupled to the $2A_g^-$ state and whose molecular nature does not rise from the C_{2h} polyenic frame, or the existence of a low-lying $2A_g^-/1B_u^+$ strongly mixed state, whose covalent/ionic nature is solvent dependent.[33,50–52]

Characteristic bands of the ICT state, whose band shape and evolution is sensitive to the solvent polarity, are localized in two regions of the transient visible spectra. Around 600-700 nm a broad positive signal is assigned to ICT $\rightarrow$ Sn excited state absorption; at 900-950 nm a negative bleaching band, which grows in few picoseconds, is assigned to the ICT $\rightarrow$ S0 stimulated emission.[42,53] The effects of solvent polarity, viscosity, temperature, excitation wavelength[54], conjugation length[42,52,55] and of substituents[45,50,56] on transient vis-

ible spectra of carbonyl carotenoids have been largely studied and several hypothesis on the relaxation dynamics have been reported. Different electronic level scheme have been suggested, like, for instance, the one proposing an initial branching from S_2 populating two S_1 and ICT separate states. However proposed models mainly diverge for the involvement of different hot states and for the presence of possible equilibrium dynamics between S_1 and ICT.[47,57] The low-lying potential energy surface of carbonyl carotenoids turns to be quite complex: the simultaneous presence of the $2A_g^-$ excited state absorption band around 500 nm and that of the ICT transient bands in polar solvents demonstrates the existence of at least two local minima out of the Franck Condon region.

Infrared and Raman spectroscopies, being sensitive to molecular rearrangements, should provide more insights, however only limited transient Infrared and Raman measurements on carbonyl carotenoids are reported in literature.[58–60] One of the most informative infrared frequency region is that around 6-7 μm, where the C=O ($\sim$1650 cm^{-1}) and C=C ($\sim$1550 cm^{-1}) stretching modes fall. The frequencies of the vibrational modes in excited states can be higher or lower than in the ground state, depending on the vibronic coupling with the specific electronic transition. From time resolved Resonant Raman measurements,[61] later confirmed by Femtosecond Stimulated Raman experiments,[62] the symmetric C=C

stretching mode was observed to shift from 1525 cm^{-1} in the ground state up to 1750 cm^{-1} in S_1, both in the non-polar β-carotene and in the carbonyl β-apo-8'-carotenal, because of the strong vibronic coupling between the symmetric $S_0(1Ag^-)$ and $S_1(2Ag^-)$ states. Also in the steady state Resonant Raman spectra, the band shape and intensity of the excited state C=C stretching mode of β-apo-8'-carotenal resulted very sensitive to the solvent polarity. Due to the low molecular symmetry, this mode is infrared active too, however the literature on the solvent dependence of this band is quite limited.

In the next chapters, we will present new measurements based on the use of infrared femtosecond pulses, and we will discuss extensively the possible localization of fingerprint vibrational modes in the excited states.

2 Spectroscopic techniques and set-ups

2.1 Steady-state UV-Vis and IR Absorption

All the steady-state Uv-Vis absorption spectra reported in this thesis have been recorded with a Perkin Elmer Lambda 950 spectrophotometer at 1 nm resolution. IR spectra, acquired on a Bruker Alpha-T FT-IR spectrophotometer at 0.2 cm^{-1} resolution, have been used as calibration reference of transient infrared spectra. The sample integrity was checked by infrared and visible absorption before and after all time-resolved measurements.

2.2 Transient UV-Vis Absorption

Transient UV-Vis absorption spectroscopy (TAS) is an optical pump-probe technique that makes use of ultrashort laser pulses to investigate reaction paths, energy and electron transfers and excited state relaxation dynamics. In this experiment a first short and energetic beam promotes molecules from the ground to a specific electronic excited state. At different time delays, a second broad and weaker pulse, i.e. the probe pulse, which extends from 350 to 750 nm, monitors the system evolution. The probe arrival measures the bleaching of the ground state, stimulates emission from excited molecules or it can be further absorbed toward higher electronic resonant states. Since transient spectra are usually plotted as absorption difference spectra

$$\Delta \mathrm{A} = \mathrm{A}_{pumpON} - \mathrm{A}_{pumpOFF}$$

positive absorbance changes are associated with excited state absorption dynamics, while negative signals correspond to bleaching and stimulated emission phenomena. All dynamics are reconstructed by recording transient spectra at different pump-probe time delays.

2.2.1 Set-up

The signal measured in a pump-probe experiment originates from the 3^{rd} order polarization, and depends quadratically on the intensity of the pump and linearly on that of the probe. In order to have high temporal resolution and large tunability of the excitation wavelength, which is usually generated by non-linear parametric amplification, a short pulsed laser source with high peak power is needed.

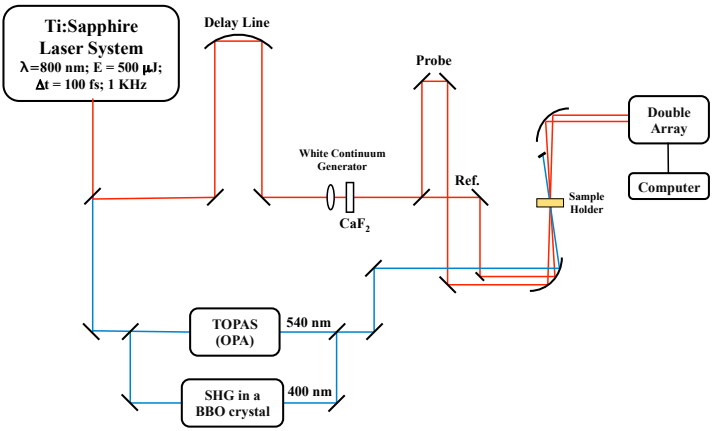

Figure 2.1: Transient UV-Vis absorption set-up.

Transient visible spectra reported in this thesis were acquiredemploying a femtosecond Ti-Sapphire laser system (BMI

Alpha 1000), which produces 100 fs pulses, centered at 800 nm (FWHM 20 nm), with 500 μJ energy per pulse, at 1kHz repetition rate (figure 3.5).[63,64] All measurements were carried out at two excitation wavelengths, in order to be on the blue and red edge of the static absorption spectrum of carotenoids in the different analyzed solvents. The "blue" excitation was set at 400 nm independently on the solvent and was generated by frequency doubling a portion of the laser fundamental in a BBO crystal. The "red" excitation was instead finely tuned between 520 and 540 nm, accordingly to the solvent, and was obtained as the sum frequency of the signal output of a commercial optical parametric amplifier (TOPAS, Light Conversion) with a portion of the fundamental output of the laser. The probe white light continuum was generated by focusing a fraction of the 800 nm fundamental on a CaF_2 window. It was split into two equally intense beams by a 50/50 beam splitter; the beam acting as the probe was spatially and temporally overlapped with the excitation beam in the sample by a parabolic mirror in an almost collinear scheme, while the second beam was delayed to provide a convenient reference signal. Finally, probe and reference beams were spectrally dispersed in a flat-field 25 cm Czerny-Turner spectrometer, and detected by means of a back illuminated CCD camera with spectral response in the region 350-750 nm. A moveable delay line made it possible to vary the time-of-arrival-difference of the pump and probe

beams up to 2.0 ns. The pump beam polarization was set to magic angle with respect to the probe beam by rotating a $\lambda/2$ plate. In order to avoid photo-degradation, the pump energy was adjusted at 150-200 μJ at the sample. This latter was continuously stirred by a micro-magnet held in a 2 mm quartz cuvette.

2.2.2 Data Analysis

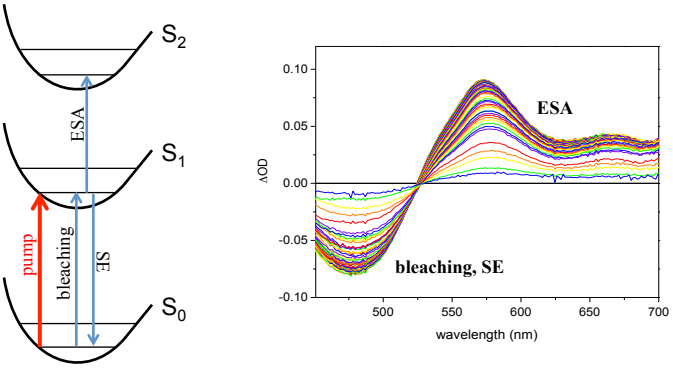

Figure 2.2: Transient UV-Vis absorption signals: positive excited state absorption (ESA) and negative bleaching and stimulated emission (SE) signals.

In the measurement, part of the probe light is scattered by the sample, while the pump pulse naturally induces flu-

orescence. Photons from both undesired phenomena enter into the spectrometer. In order to correct for these effects, reference spectra are acquired in the absence of the pump (to correct for the probe light scattering) and in the absence of the probe (to correct for the fluorescence), before starting the experiment. Home-written LabVIEW software manages the large amount of data and saves the corrected and averaged spectra for each pump-probe delay. The two-way matrix (spectral intensity as a function of wavelengths and pump-probe delays) is then reconstructed in Matlab and serves as the input of the GLOTARAN package (http://glotaran.org) [65,66] used for the global analysis of the data. In the global analysis process, spectra at different delays together with kinetic traces at different wavelengths are simultaneously fitted to extrapolate time-independent spectra and wavelength independent kinetics.[67] As the first step, the single value decomposition (SVD) procedure extracts the number of significant components from the diagonalization of the input matrix. These components can be seen as compartments (e.g. excited states) that have to be linked through a convenient kinetic scheme. Applying a preliminary sequential first order kinetic scheme, one obtains the Evolution Associated Difference Spectra (EADS, or simply EAS), which are indicative of each compartment and highlight the featuring evolving bands. Often, however, EADS are not the representative spectra of the species involved in the photo dynamics of the

analyzed system. Departing from EADS, a more complex kinetic scheme can be applied in the so-called target analysis, to obtain the Decay Associated Difference Spectra (DADS), which are real spectra associated to compartments. However, if the kinetic scheme of the studied system is not known from other experiments, the application of the target analysis can bring to wrong interpretation of data. In the Glotaran fitting algorithm, several parameters are adjustable according to the technical characteristics of the set-up, like the position and the width of the instrumental function and the group velocity dispersion (GVD) of the "white" probe, which is fitted by an adjustable polynomial function. The experimental zero time (i.e. the time corresponding to the pump-probe temporal overlap) is thus affected by some uncertainty, because each probe wavelength overlaps the pump pulse at a slightly different time (figure 2.3). Its polynomial estimation is therefore mandatory to correct data and locate a common zero for all kinetic traces.

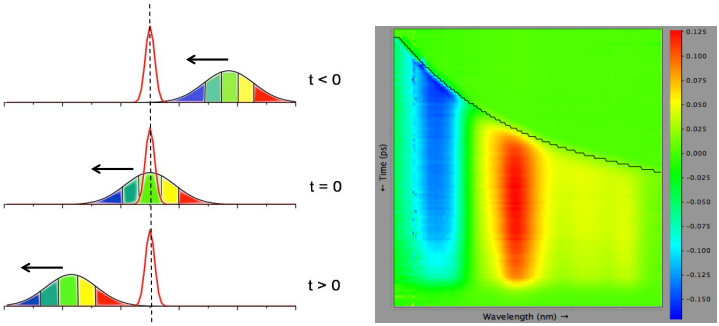

Figure 2.3: A positive chirped probe causes a negative chirped signal. On the right, an example of the polynomial fit of the probe dispersion obtained by Glotaran.

2.3 Transient IR Absorption

Information on the electronic excited states ladder is easily accessible by means of transient absorption spectroscopy in the Visible range; structural information is, instead, hardly achievable. Broad transient Vis bands span over hundred wavelengths in the ten thousand wavenumber region, they often overlap and are usually featureless and not informative about the active vibrational modes in excited states. The detection of structural changes in excited states is interesting for the characterization of meta-stable transition states along a reaction coordinate, as well as for the identification of predominant vibrational modes in non-radiative deactivation pathways. Non-radiative transitions always proceed through vibrations (e.g. internal conversion through vibronic coupling or thermal relaxation through coupled vibrations with the bath) and often this leads to a departing from the Franck Condon region. Structural information can be retrieved from Infrared and Raman Spectroscopies, which are sensitive to different microscopic properties: in the infrared any change in the orientation, intensity and energy of the transition dipole moment associated to a specific nuclear rearrangement is probed. Complementary to infrared absorption, vibrational modes can be probed also by Raman effect, which, similarly to an electronic spectroscopy, involves visible beams and is sensitive to any change in the electronic

density distribution over the entire molecule, namely to any change of the molecular polarizability anisotropy. While the transition dipole moment is a vector, the polarizability is a tri-dimensional tensor which can be considered as a rough estimate of the molecular shape.

2.3.1 Set-up

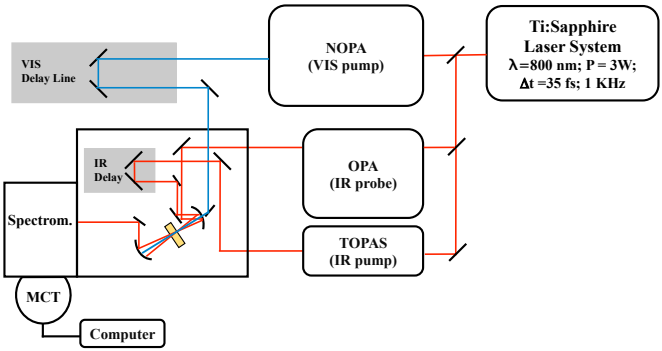

Figure 2.4: Schematic view of the set-up for Transient IR Absorption, 2D-IR, Transient 2D-IR and Labeling measurements.

The experimental set-up used for time resolved infrared measurements has been extensively described before.[68,69]

Briefly, a portion of the output of a Ti:Sapphire oscillator/regenerative amplifier, operating at 1 kHz, centered at

800 nm, with pulse duration less than 50 fs (Legend Elite, Coherent), was split in order to generate the mid-IR probe and the Visible (VIS) pump. The infrared probe had a spectral width of 200 cm^{-1} in the 6 μm region and was obtained from difference frequency generation in a $AgGaS_2$ crystal of the signal and idler beams from a homebuilt two-stage optical parametric amplifier (OPA). The mid-infrared output was further split into two beams of equal intensity, which were respectively used as probe and reference and focused in two different spots on the sample. The VIS pump at 400 nm was generated by frequency doubling another portion of the laser fundamental beam in a BBO crystal, while the excitation at 540 nm was generated by a home-made non-collinear optical parametric amplifier (NOPA). At both excitation wavelengths the VIS-pump pulse was attenuated to 100-300 nJ at the sample and focused in a 150 micrometers diameter spot. The polarization of the pump was set to the magic angle with respect to that of the probe by rotating a $\lambda/2$ plate. A moveable delay line along the pump path made it possible to vary the time delay with respect to the probe up to 1.8 ns. After the sample, both probe and reference were spectrally dispersed in a spectrometer (TRIAX 180, HORIBA Jobin Yvon) and imaged separately on a 32 channels double array HgCdTe detector (InfraRed Associated Inc., Florida USA) under nitrogen. All spectra were recorded in two spectral windows covering from 1450 to 1800 cm^{-1} with a resolution

of 6 cm^{-1}.

2.3.2 Data Analysis

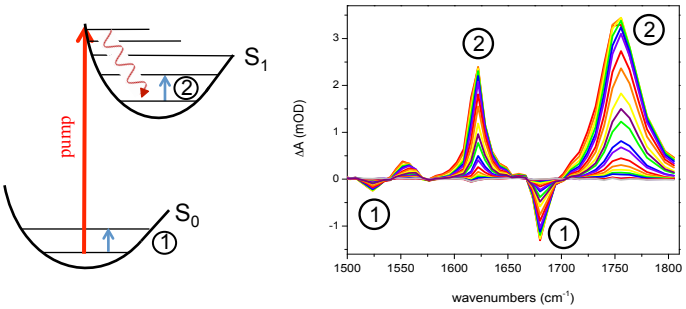

Figure 2.5: Transient IR absorption signals: negative signals (1) correspond to the bleaching caused by the pump of the vibrational modes in the ground state; pump absorption is followed by vibrational cooling on the electronic excited state in few picoseconds (undulated arrow); positive signals (2) rise from excited state IR absorption (ESA).

As reported for transient Vis measurements, all data were first accumulated, downloaded and saved through the LABVIEW programmed interface and then averaged over multiple scans in Matlab. Once the two-way matrix was ob-

tained, the spectral and kinetic analysis was done using both Glotaran and Origin softwares. The direct visualization of the two-dimensional data obtained from Glotaran highlights the striking different probe dispersion in the infrared, where it is almost flat, with respect to the visible region.

In average, the transition dipole moment of vibrational modes is about one order of magnitude smaller than that of electronic transitions. Then highly concentrated samples need to be prepared for infrared spectroscopy ($\sim 10^{-2}M$). The sample cell consists of two 1 mm thick fluorite windows, separated by a Teflon spacer of 50 or 100 μm. The small optical path length avoids self-absorption phenomena of the Vis pump and limits the pump beam attenuation along with the optical path. Therefore, the best signal-to-noise ratio is achieved by keeping concentration close to the solubility limit but avoiding in the meanwhile scattering over-saturated solution.

The frequency resolution does not exceed 6 cm^{-1} due to the limited number of active elements (32) in each MCT array. The spectral calibration is obtained by measuring the absorption spectrum of a standard polystyrene sample for all the frequency regions considered. Calibration is conducted taking as a reference its 0.2 cm^{-1} resolved FT-IR spectrum.

2.4 2D-IR Spectroscopy

Two-dimensional infrared (2D-IR) spectroscopy is a ground state technique that provides a powerful tool to study transient molecular structure and dynamics. As a vibrational spectroscopy, it directly watches at vibrating molecular bonds and how those vibrations interact with one another and with the sorroundings.

Similarly to the two-dimensional techniques first developed and widely applied in nuclear magnetic resonance (NMR), 2D-IR spectroscopy spreads a vibrational spectrum over two frequency axes. From such a 2D spectrum one learns how excitation of a vibration influences all other vibrations (within a given spectral window); if short infrared pulses are used, direct information on the system time evolution becomes accessible.

Spectral features, namely frequencies, amplitudes, line-shapes, and their evolution in time are used to understand structural connectivity in space and time, thus offering new possibilities for studying molecular structure and dynamics. If we do precede a visible pulse, in resonance with some molecular electronic transition, to the 2D-IR pulse sequence, we realize a non-equilibrium variant of the technique, from which we learn about the molecular dynamics in the excited state.

In the following, we briefly outline two different approaches to the realization of a 2D-IR experiment:

- *the frequency domain*: this it is the method (also known as "dynamic hole burning") that was realized first.[70] It makes use of a conventional pump-probe geometry with a narrow band pump selected by a Fabry-Perot interferometer that scans the frequency across the broad band of the IR pulse. Two electric fields from the pump pulse impinge simultaneously and collinearly on the sample; a second delayed pulse, the probe, induces a collinear response signal. The probe field acts as carrier wave of the weak signal (self-heterodyne detection), which is spectrally dispersed and recorded in the frequency domain. The two axes of the absorptive 2D spectrum correspond to the frequencies of the pump and probe pulses, respectively. This is the experimental approach adopted in this thesis work; the used set-up will be described in details in the next section.

- *the time domain*: it is a Fourier Transform method also known as "Photon-Echo". Three beams impinge on the sample from different directions with district arrival times: the first two pulses act as the IR pump, the 3^{rd} one is the probe. The response signal is emitted in a direction that does not coincide with any of the incoming beams; the heterodyne detection can be realized by

adding an external local field coincident with the signal. A two-dimensional interferogram is collected by scanning the time delay between the first two pulses and that between the third and the local field . A double Fourier transformation gives back the pump and probe frequencies.

Advantages and disadvantages of the methods and the technical details are deeply discussed in ref. [71].

2.4.1 Set-up

2D-IR spectra were recorded on the system of figure 2.4 in the frequency domain. The pump and probe mid-IR beams were generated by two optical parametric amplifiers, as previously described (see paragraph 2.3.1). From both parametric amplifiers a gaussian beam of 100 fs, 200 cm^{-1} broad and centered at 6 μm was obtained. The spectral bandwidth of the intense IR pump was narrowed to 15-17 cm^{-1} by means of a Fabry-Perot interferometer (etalon); correspondently, the pulse duration increases to about 800 fs (τ) and the pulse energy after the interferometer was about five times smaller than before. The pump beam was finally sent to a moveable delay line; its polarization was set to the magic angle with respect to the probe by means of a $\lambda/2$ waveplate. The focusing at the sample and the detection system was the same

as that reported in section 2.3.1 for the transient infrared absorption set-up.

2.4.2 Data Analysis

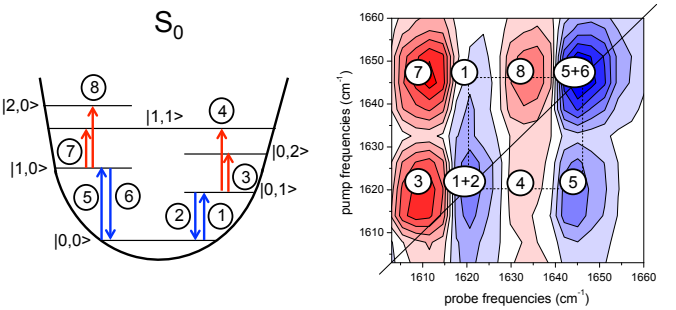

Figure 2.6: 2D-IR spectrum in presence of strongly coupled modes (Phenol Blue in dichloro-methane): negative signals are in blue and correspond to bleaching and stimulated emission processes, positive signals are in red and correspond to excited state absorption.

The two axes of a 2D-IR spectrum correspond to the pump and the probe frequencies. Each 2D spectrum is measured at a given pump-probe delay and results from the interpolation of side-by-side 1D spectra of the probe acquired for different

frequencies of the narrow-band pump. The spectral narrowing of the pump causes a Fourier intrinsic loss in the time resolution.

Two types of measurements on this set-up are possible. If both pump and probe beams are broad-band, i.e. if the Fabry Perot is removed from the pump pathway, experiments can reach the best time resolution, but it will be impossible to selectively excite the individual modes. On the other side, if a narrow-band pump is used, dynamics within the first picosecond will be lost, but it will be possible to follow the time evolution of the individual modes and to disentangle the inter-mode couplings.

2.5 5^{th} order spectroscopies

In the case that a typical 3rd order non linear spectroscopic technique, like 2D-IR, is used to probe the properties and the evolution of an electronic excited state prepared by a visible pulse, the overall experiment can be described as an example of 5th order spectroscopy. In such an experiment, two electromagnetic fields are contributed by the visible pump pulse; two more fields are involved in the action of the second pump, and the fifth is brought by the probe pulse.

In the following, we consider two different 5^{th} order spectroscopic techniques that use, with a different time ordering, one visible pump, one infrared pump and one infrared probe. The set-up reported in figure 2.4 was properly adapted in order to accommodate the pulse sequence for the appropriate three beams experiment. In the last part of the chapter, a third 5th order experiment, the Time Resolved Stimulated Raman, will be described. This set-up was built in collaboration with Dr. Tomasz Kardas from the University of Warsaw.

2.5.1 Transient 2D-IR Absorption: Vis pump-IR pump-IR probe

As previously discussed, electronic excited state dynamics can be studied by visible and infrared transient spectroscopies. It is also apparent that adding a second dimension to transient spectra opens the access to relevant information, concerning the presence of hidden peaks as well as of cross peaks that may be important to unveil the nature of the excited states. In transient 1D infrared spectra, ground state bleachings are often hidden by positive excited state bands. In the electronic excited state some vibrational modes can show very large frequency shift with respect to their frequency position in the ground state, as a result of large vibronic coupling (i.e. the coupling of the dipole moment associated to the vibration with the electronic dipole moment of the electronic excited state). The analysis of active vibrational modes in the electronic excited state allows monitoring structural changes associated with the relaxation. Bredenbeck et al.[72,73] were the first to add a second dimension to transient IR spectra. They applied a 2D-IR pulse sequence after a visible excitation pulse, so that, repeating the experiment at different delays between the visible pump and the infrared sequence, they obtained 2D spectra of an evolving non-equilibrated system.

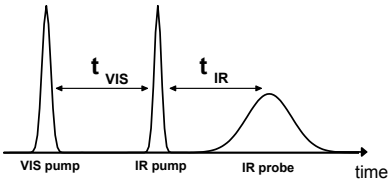

Figure 2.7: Pulse sequence in a Transient 2D Infrared experiment.

In our experiment, based on the Transient Infrared and 2D-IR set-up (figure 2.4), we combine the visible pump generated by the home-made NOPA, the infrared pump from the commercial TOPAS, followed by the Fabry Perot interferometer, and the infrared probe from the home-made OPA. Measurements were conducted at 400 and 520-540 nm excitation wavelengths. The excitation pulses at 400 nm were obtained from second harmonic generation (SHG) of a portion of the laser fundamental in a BBO crystal, resulting in a bandwidth of 6 nm. The excitation wavelength around 520-540 nm was finely tuned by controlling the NOPA generation, so that it was centered at half height of the steep slope on the red side of the carotene static Vis absorption spectrum; its bandwidth was 20 nm. A $\lambda/2$ plate was used to set the polarization of the visible beam at the magic angle with respect to IR beams, whose relative polarization was set parallel. the pulse energy of the visible pump was attenuated

to provide 100-300 nJ at the sample, in a focused spot of 150 μm diameter.

As shown in figure 2.7, two time delays can be varied: we fixed the IR delay at the maximum of the pump-probe IR signal (t_{IR}= 500 fs) and scanned the delay t_{VIS} of the visible pump with respect to both IR beams. In this way, single snapshot (in the form of 2D infrared spectra) are caught during the relaxation of the electronic excited state.

The necessary steps involved in measuring transient 2D spectra can be summarized as follows:

1. optimization of the narrow-band IR signal at the ground state (VIS pump blocked). The IR pump is chopped to extract the difference absorption spectra. Fix the IR delay between pump and probe at the maximum of signal intensity.

2. optimization of the transient IR signal (IR pump blocked). The VIS pump is chopped and the linear transient infrared difference spectrum is measured. At this step, excited state vibrations are visible: take note of their frequency position.

3. repositioning of the chopper in the IR pump path. The central frequency of the excited state vibration will be the target position of the narrow-band IR pump. Close

the sample chamber and flux nitrogen for at least 15 minutes. Open both VIS and IR pump beams and look for the difference signal at the excited state vibrational frequency.

Generally, expected signals are weak, obviously depending on concentration and on the spacer used in the cell (i.e. the optical path length). A great stability of the baseline, which depends on the laser source stability and on the quality of the IR probe generation, is strongly recommended to increase the signal to noise ratio together with the lack of humidity inside the sample chamber.

Excited state 2DIR spectra result from a double difference absorption signal: $\Delta\Delta A = \Delta A_{IR}^{VISon} - \Delta A_{IR}^{VISoff}$. Using a single chopper placed along the IR pump path, the double difference spectra is post-processed by subtracting the background, in other words by subtracting the 2D spectrum collected at negative delays ($t_{VIS} = -10ps$) from the ones measured at positive delays. Note that at negative delays both IR beams impinge on the sample before the Vis pulse. Hence, in T2D-IR spectra, the ground state signals result with inverted signs: the bleaching and the stimulated emission are positive, while vibrational excited state absorptions are negative.

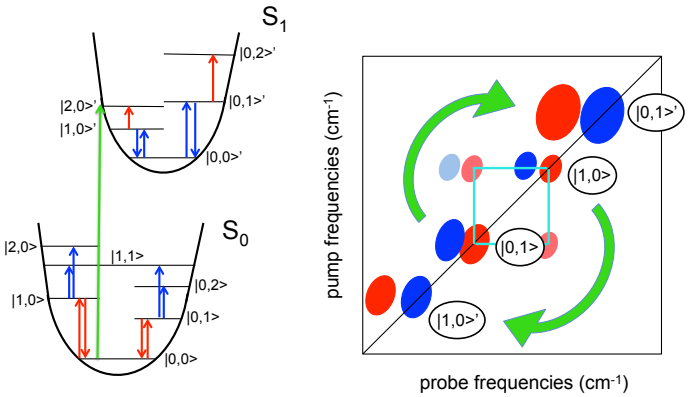

Figure 2.8: Exemple of transient 2D-IR spectrum: coupled modes in the ground state loose their coupling in the excited state and shift to opposite directions.

Usually diagonal peaks are easily identified by comparison to the FT-IR and transient 1D-IR spectra, however, the interpretation is not so obvious in the off-diagonal regions, especially in highly coupled systems. Since three beams are used, one could decide to fix the first delay between the Vis and the IR pump and scan the IR pump-probe delay, as reported by Bredenbeck et al.[72] If the electronic excited state lives longer than the cooling on its vibrational manifold, a complete spectral diffusion analysis of an excited state vibrational mode is possible and the solvent rearrangement around the excited solute molecule can be monitored.

2.5.2 Excited State Vibrational Labeling: IR pump-Vis pump-IR probe

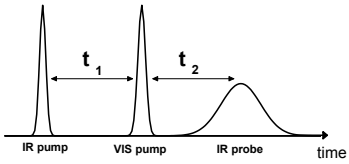

Figure 2.9: Pulse sequence in a Vibrational Labeling experiment.

In this technique, the order of the Vis and IR excitations is inverted with respect to the T2D-IR pulse sequence (figure 2.9). A first narrow IR pulse excites, or in other words "labels", a vibrational mode in the ground state. Right after it (t_1), a VIS pump pulse transfers the system from a non-thermally equilibrated ground state to an electronic excited state. In this way, the vibrational population distribution of the ground state is directly projected into the electronic excited state (figure 2.10). Finally, the IR broad band probe pulse interrogates the excited system. In order to maintain memory of the labelled vibration, the time-of-arrival of the probe with respect to the IR pump (t_{IR}=t_1+t_2) has to be set within short lifetime of the vibration in the excited or in the ground state. In this case, the probe unambiguously identifies the frequency of the vibrational mode in the electronic

excited state.

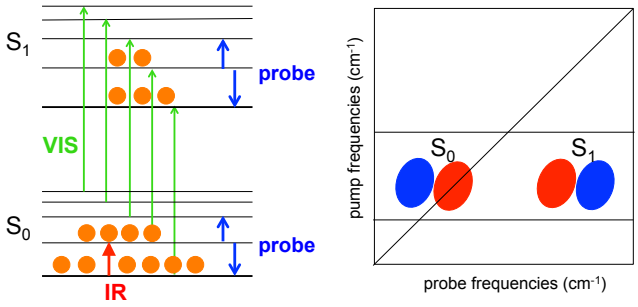

Figure 2.10: A visible excitation projects the out-of-equilibrium population of the ground state to an electronic excited state within the vibrational lifetime.

The excited state signal is expected in the off-diagonal region, as shown in the example sketched in figure 2.10. The IR pump is tuned at the frequency of the ground state vibration, while the broad IR probe reveals simultaneously the ground state vibration (on the diagonal) and the shifted electronic excited state vibration (at higher frequencies in this case). The intensity of the excited state vibration in the off-diagonal region is enhanced by the vibronic coupling and decays with increasing t_1+t_2 delay (see figure 2.9), according to the lifetime of the vibrational mode. The labeling spectra reported in this thesis were measured at fixed delay t_{IR}= t_1+t_2= 1

ps, scanning the Vis pump-IR probe t_2 delay within the t_{IR}= 1 ps delay. Background spectra were acquired without the Vis pump and correspond to equilibrium ground state 2D-IR spectra recorded at 1 ps. We observe an increase of the off-diagonal peak intensity when the Vis pump was moved closer in time to the IR pump. The relative polarizations of the three beams were set parallel. By keeping the Vis pump IR pump delay fixed at 500 fs we avoided artefacts due to the temporal overlap to the pump, still maintaining a reasonably good signal intensity. Indeed, for small values of t_1, the out-of-equilibrium population in the ground state is frozen by the Vis pump before vibrational cooling takes place.

This technique was successfully applied for the first time by Bredenbeck et al. [72,74] to assign the symmetric and asymmetric stretching modes of equatorial and axial C=Os of a bipyridyl- Rhenium(I) complex upon *metal to ligand charge transfer* (MLCT) transition. Here, we re-propose tho method to unambiguously assign the C=O stretching vibration of carotenoids in the electronic excited states and, consequently, to confirm the assignment of the largely upshifted chain C=C stretching.

2.5.3 Transient Stimulated Raman Spectroscopy

In the literature this technique is better known as Femtosecond Stimulated Raman Spectroscopy (FSRS). First developed by R. A. Mathies at the University of California, Berkeley, in 2003[75,76], it consists of a Stimulated Raman experiment in the electronic excited states. The word "Femtosecond" refers to the time resolution that can be reached when the two simultaneous Raman pulses that impinge on the sample are delayed with respect to the visible *actinic* pulse. Time-resolved Stimulated Raman spectra are thus recorded at different "actinic pump - stimulated Raman probe" delays. Since its first implementation, this technique has been applied for a variety of topics: molecules involved in photosynthesis, like β-carotene[77], molecules involved in the mechanism of vision[78,79] (rhodopsin), photo-induced spin crossover in iron complexes[80] and, recently, excited state proton transfer[81]. In 2013, thanks to Dr. Kardas, we built a FSRS set-up in our laboratory, thus implementing the transient linear and two-dimensional infrared spectroscopic instrumentation with the complementary transient Raman counterpart.

The Raman scattering effect can be seen in a classical approach as an inelastic collision between a photon and a molecule, in which a small part of the overall collision energy

can be left on the molecule or given to the photon. Microscopically, a molecule is defined as "Raman active" when the applied external electric field causes a variation in its polarizability at least along one of its molecular coordinates. From a macroscopic point of view, instead, the overall polarization $\vec{P}$ reacts instantaneously to the light perturbation accordingly to the electric susceptivity of the solution. Although spontaneous Raman effect is usually described as a linear spectroscopic technique, since the recorded signal intensity is ultimately proportional to the intensity of the applied excitation beam, all Raman techniques are better described as 3^{rd} order non-linear spectroscopies.[82,83] In the following, we will focus on the differences between the spontaneous and the stimulated Raman spectroscopies to then up-grade to the excited state time-resolved technique.

- *Spontaneous Raman Scattering*

  Only one visible non-resonant beam is focused on the sample. The light is then incoherently scattered in the entire solid angle and detected in a back-scattering geometry, orthogonally or possibly with an integrating sphere. On both sides of the strong elastic scattering Rayleigh line, the weak Raman lines appear, separated from the Rayleigh line by vibrational energy quanta. In figure 2.11, the Raman intensity is plotted versus the vibrational difference frequencies $\Delta\omega = \omega_{scatt} - \omega_0$,

expressed in wavenumbers. On the Stokes side photons are scattered at lower frequencies than the Rayleigh line: $\omega_{scatt} < \omega_0$ because part of the photon energy is left to the molecule. On the anti-Stokes side, instead, an excess of energy initially in the molecule is transferred to the photon which is scattered at higher frequencies: $\omega_{scatt} > \omega_0$. Exchanged quanta between molecules and photons correspond to the characteristic vibrational energies of the investigated molecular system, therefore, Stokes and Anti-Stokes transitions are specular with respect to the Rayleigh line. The two branches differ in intensity because of the Boltzman factor: while Stokes transitions depart from the ground state, i.e from the minimum energy configuration where almost all the molecules are at thermal equilibrium, the Anti-Stokes intensities depend on the population of hot vibrational levels (at room temperature only modes with E < 200 cm^{-1} are active). Note that from the perturbation theory, virtual states $|n_1>$ and $|n_2>$, which are not stationary eigenstates of the system, can instantaneously exist as superposition of all the eigenstates.

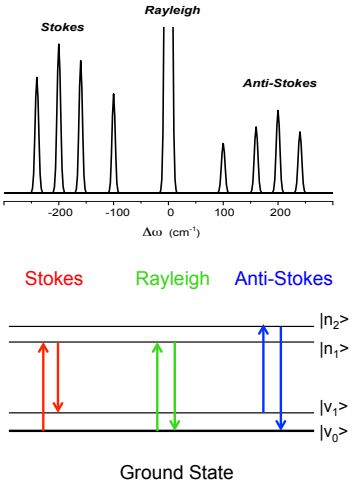

Figure 2.11: Schematic view of a spontaneous vibrational Raman spectrum and corresponding level diagrams with Stokes, anti-Stokes and Rayleigh transitions.

- *Stimulated Raman Scattering*

  As reported in figure 2.12, two beams from different directions, the Raman pump (red) and the probe (blue), impinge on the sample at the same instant generating a vibrational Raman coherence in the electronic ground state of the molecule. Due to the phase-matching condition ($\vec{k}_{signal} = \vec{k}_{pump} - \vec{k}_{pump} + \vec{k}_{probe}$), the signal

is coherently scattered along the probe direction and self-heterodyne detected, as in a normal pump-probe geometry.

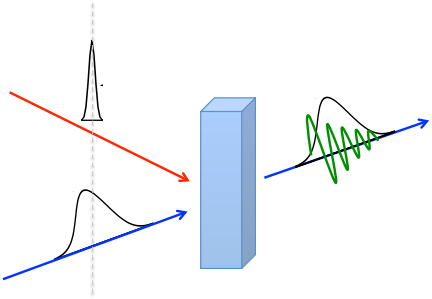

Figure 2.12: Two beams, the Raman pump (red) and the probe (blue) hit the sample at the same instant. The light is coherently scattered by the sample along the probe direction.

The sensitive of the method is much higher than that of spontaneous Raman; for instance, differently from its spontaneous counterpart, it allows to measure the Raman spectrum of diluted solutions. The probe bandwidth is generally made as broad as possible and centered at the same frequency as the Raman pump; in most cases Raman transitions can be revealed in the range of ± 1500 cm^{-1} with respect to the frequency of the Raman pump. At frequencies lower than that of the Raman pump (Stokes side) the bands corre-

spond to an increased probe intensity (Raman Gain); at higher frequencies (anti-Stokes side) bands correspond to a depleted probe intensity (Raman Loss). Similarly to the spontaneous Raman, in a Stimulated Raman spectrum Raman Gain and Loss bands appear symmetrically with respect to the Raman Pump. Usually the spectral profile of the probe is subtracted to obtain a zero baseline. As a consequence, the resulting spectrum consists of negative Anti-Stokes and positive Stokes bands. Division rather than subtraction is usually preferred, since it ensures that signal magnitude does not depend on the intensity profile of the probe, which can vary day by day. Differently from spontaneous Raman, Stokes and anti-Stokes intensities are the same, as in both cases the intensity dependence on the thermal population is the same.

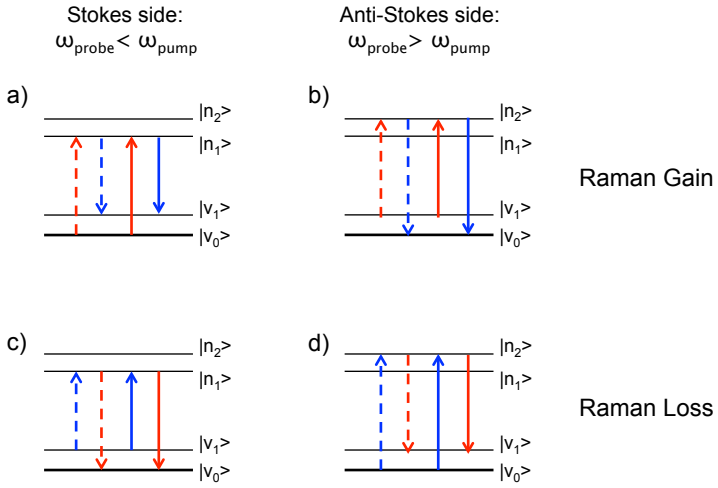

Figure 2.13: Raman pump (red) and probe (blue) interactions on the <bra| (dashed arrows) and |ket> (solid arrows) wavefunctions. Raman Gain and the Raman Loss signals are defined with the detector placed along the probe direction. At the molecular level is not possible to distinguish between diagrams a-c) and b-d), because all interactions take place at the same instant. Due to the Boltzmann factor, a) and d) diagrams respectively determine positive bands on the Stokes side and negative bands on the anti-Stokes side of the SRS spectrum.

- *Time-Resolved Stimulated Raman Scattering*

  By applying a visible ultrashort excitation prior to the stimulated Raman pulses, electronic relaxation dynamics as well as photochemical reactions can be monitored. Raman techniques present several advantages with respect to the infrared ones: in the visible wavelength range the set-up is definitely less expensive and more stable; low frequencies vibrations, hardly accessible in IR, can be easily measured; the experiment is not disturbed by the presence of atmospheric humidity; the interferences of the solvent bands, water *in primis*, are often negligible. In resonant condition, desired signals can be strongly enhanced over the background by tuning the Raman pump and thus increasing the selectivity (e.g. in proteins, chromophore signals can be enhanced over the protein background). These features are equally valuable in out-of-equilibrium transient experiments. Nonetheless, the real power of the Transient Stimulated Raman Spectroscopy relies on its high temporal and frequency resolution:

  - the temporal resolution ($\sim$100 fs) results from the cross correlation between the femtosecond actinic pump and the probe;

  - the frequency resolution depends on the convolution

of the narrowband Raman pump (1-2 nm, ∼1 ps) with the natural linewidth of the vibration.

A Raman pump bandwidth of 1-2 nm around 800 nm corresponds to a frequency resolution of about 20 cm^{-1}. Several methods of spectrally narrowing the Raman pump have been developed,[84] for Ti:Sapph laser output (centered at 800 nm, with a <50 fs pulse duration) as well as for OPA or NOPA (Non-collinear Optical Parametric Amplifier) outputs, usually used in Transient Resonant Raman experiments to make the Raman pump tunable.

Both bandwidth and temporal profile of the Raman pump have to be controlled. Indeed, the shape of the Raman bands result from the FT transformation of the product of the Raman pump time profile and the dephasing of the molecular vibration. Thus, a truncated temporal profile of the Raman pump would result in side-bands around Raman lines.[84] The shape of FSRS bands also depends on the dynamics of the molecule in the excited state. If, along with the relaxation process, the vibration in the excited state undergoes a frequency shift faster than its dephasing time, a broad and dispersive line shape is expected. In other words, only when excited state dynamics is slower than vibrational dephasing, well-defined and sharply peaked Raman bands

will appear in FSRS spectra.[85,86]

Set-up:

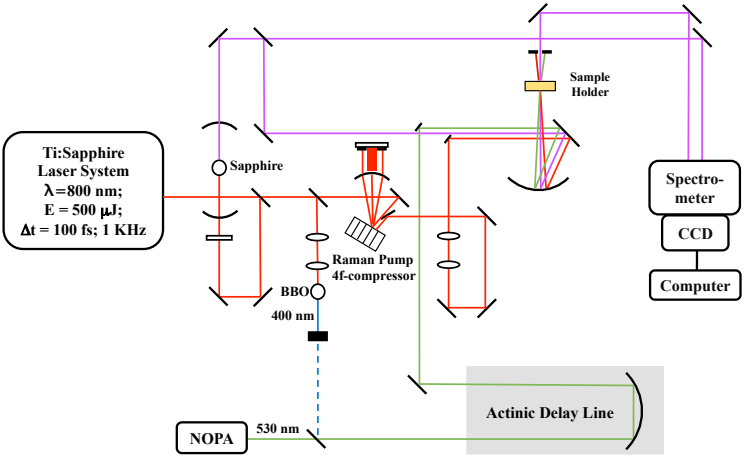

Figure 2.14: Femtosecond Stimulated Raman Spectroscopy set-up: the Visible Actinic is reported in green, the Raman Pump at 800 nm in red and the white-probe in violet.

A 350 mW portion of the 800 nm laser source, already described in paragraph 2.3, is used to pump the Raman set-up of figure 2.14. Three pulses are needed in this experiment:

- the *Actinic* beam

- the *Raman Pump*

- a *super-continuum probe*

The visible actinic excitation was generated at 400 nm by second harmonic generation in a 1 mm thick BBO crystal (type I to maintain the horizontal polarization) or taken from the non-collinear optical amplifier NOPA (figure 2.4), which can be tuned from 450-750 nm range. The visible pump passed through a motorized translation stage (maximum delay 1.2 ns), then through a telescope and finally was focused on the sample with a spot size of 100 μm diameter, maintaining the pulse duration below 100 fs. The power at the sample was adjusted around 100-200 nJ/pulse to avoid photo-degradation and ensure a stable baseline. Higher pulse energy would increase the ground state depletion and the intensity of the excited state signals only within the linear regime. Too high power of the actinic beam results in persistent negative ground state signals in FSRS spectra.[81]

In order to obtain the Raman pump, a faction of the 800 nm fundamental ($\sim$300 mW, bandwidth 20 nm), was passed through a 4f-diffraction grating spectral filter,[87] which narrowed its band to 1-2 nm, corresponding at 800 nm to about 20 cm^{-1} of frequency amplitude

and to a pulse duration of 800 fs. The "4f-grating spectral filter" consists of a grating with 1250 grooves/mm, blazed at 780 nm (first order) placed at the Littrow configuration, which angularly disperses the frequency components of the incoming beam toward a cylindrical lens, placed at its focal distance (10 cm). The lens focusses the spectral components on a flat mirror, placed right behind an adjustable slit entrance, which selects the needed spectral components. In the back reflected pathway, selected frequencies are recombined and collimated in a single beam with minimized GVD dispersion. Finally, it passed through a movable delay line to set at zero the time of arrival with respect to the probe, then through a telescope and finally it was focused on the sample with a spot of 80 μm diameter, at *ca.*2μJ/pulse.

The Raman probe consisted of a super continuum pulse generated by tightly focusing a small portion ($\sim$7%) of the entering 800 nm fundamental in a 1 mm Sapphire plate. A spectrally broad probe (the super-continuum) was generated centered at 800 nm; then, it was split into the probe and reference beams. The reference was directly focused at the entrance slit of the monochromator, while the probe beam was focused at the sample with a 70 μm spot size.

All three beams lie on the same horizontal plane, with parallel polarization and close to each other ($<$ 2 mm distant) in order to optimize the overlap in the focus of a 150 mm concave mirror (focus length *ca.* 2 mm, with a crossing angle $<$ 1 degree). The sample was held in a 2 mm thick quartz cuvette and moved to avoid degradation. After the sample, the probe beam was selected through an iris aperture, re-collimated and finally focused at the entrance slit of the monochromator, on the vertical of the reference beam. Probe and reference were spectrally dispersed by the 25 cm Jobin Yvon HR250 spectrometer and detected by a 512 pixels double array CCD detector (S8380-512Q Hamamatsu). A chopper in front of the detector, synchronized with a second chopper placed in the Raman pump path,allowed collecting the signal with the Raman pump on and off, alternatively. The temporal and spatial overlap of the Raman pulses and the actinic pulse was optimized looking at the transient absorption signal around 700-800 nm (on the anti-Stokes side, with the Raman pump closed and the chopper placed in the actinic beam path) of a 4,7-dithien-2-yl-2,1,3-benzothiadiazole (DTBT) solution in acetonitrile.

The Stimulated Raman Signal was finally obtained as:

$$SRS = \frac{I_{probe}^{RPon}}{I_{probe}^{RPoff}} \cdot \frac{I_{ref}^{RPoff}}{I_{ref}^{RPon}} \tag{2.1}$$

where I^{RPon} and I^{RPoff} are the intensities measured with the Raman pump on and off, respectively.

The amplitude of the transmitted signal was recorded in a two-way matrix: frequency vs actinic pump delay. At negative delays, the Raman pump and probe pulses arrive before the actinic pulse, thus Stimulated Raman spectrum of the ground state is measured. By subtraction of this background to spectra collected at positive delays, the Femtosecond Stimulated Raman Signal was retrieved.

$$FSRS = SRS_{ACTon} - SRS_{ACToff} \tag{2.2}$$

Femtosecond Stimulated Raman spectra reported in this thesis were corrected in order to obtain a uniform zero baseline by fitting, at each time delay, row spectra baseline with a 3^{rd} order polynomial function. Transient absorption experiments performed in the visible range on the same sample demonstrated that the non-zero baseline originates from an underlying transient absorption of the probe, due to the actinic pump excitation.

3 Excited State Dynamics of trans-β-apo-8' Carotenal *

The *all* trans-β-apo-8'-carotenal, also known as E160e, is used as additive for its red-orange color in foods, pharmaceuticals and cosmetic products. It can be found in spinach and citrus skin, but it mainly results from oxidative degradation of β-carotene. Like the latter, it is a precursor of retinol (Vit A). Here, it is studied as a model compound of more complex carbonyl carotenoids such as peridinin, fucoxanthin and siphonaxanthin. This simple molecule with only one carbonyl substituent allows to rationalize the effect of the conjugated electron withdrawing group on the excited state electron density distribution. The molecular structure

*This chapter is based on ref. [69]

of the *all* trans-β-apo-8'-carotenal is very similar to that of retinal (figure 3.1), which is not classified among carotenoids because of its short conjugation length (N=4). Retinal is known to isomerize when bound to the opsin protein.[43,78] The conformational change is crucial in the mechanism of vision, however, the study of excited state dynamics along the torsional coordinate in longer aldehydic analogues, such as in the *all*-trans-apo-12' carotenal (N=6) and in the 8' carotenal (N=8), has been less investigated so far.

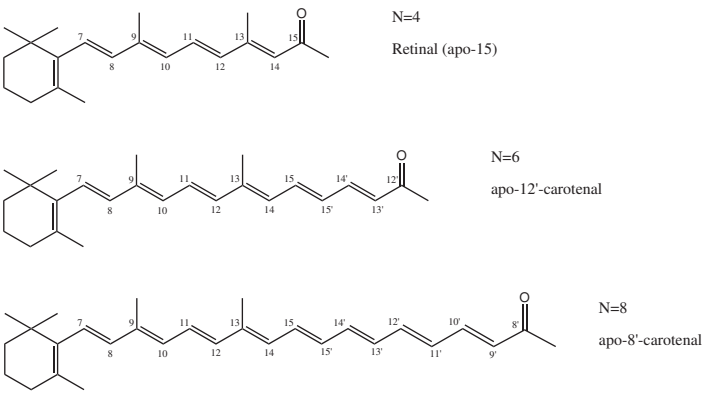

Figure 3.1: Apo-N'-carotenals analogues of retinal.

In order to investigate the sensitivity of carbonyl carotenoids to the polarity of the environment and the nature of the intramolecular charge transfer (ICT) state, supposed involved in the excited state relaxation, we carried out ultrafast time-resolved visible and infrared measurements in several solvents, differing both for polarity and polarizability, and at different excitation wavelengths. By comparing the spectral evolution observed in the visible and in the infrared regions, we identified bands attributable to the ICT state. The nature of the excited state vibrations was finally investigated by means of Labeling and Transient Raman experiments.

3.1 Sample Handling

All trans-β-apo-8'-carotenal was purchased from Sigma Aldrich and used without further purification. For infrared measurements, samples were highly concentrated and held between two CaF_2 windows of 2 mm of thickness, separated by a 50 μm Teflon spacer. The sample cell was mounted on a movable stage in order to minimize degradation and placed in a sample chamber under nitrogen flux. For transient visible absorption measurements, more diluted samples with an absorbance of 0.2-0.4 OD (optical path 2 mm) at the excitation wavelength were used and held in a 2 mm thick quartz cell kept under constant stirring by a small magnet inserted

inside the cell. All measurements were carried out at room temperature.

Solvents were purchased from Sigma-Aldrich at HPLC grade of purity and used without further purification. In table 5.1 used solvents are listed according to increasing polarizability R(η). Solvent polarity and polarizability have been calculated respectively through the solvent refractive index η and the relative dielectric constant ε_r values taken at 293 K. The Clausius-Mossotti (eq.3.1) and the Lorentz-Lorenz (eq.3.2) equations have been used in order to compare results with previous studies on carotenoids.[39,41,42,47]

$$P(\varepsilon_r) = \frac{\varepsilon_r - 1}{\varepsilon_r + 2} \tag{3.1}$$

$$R(\eta) = \frac{\eta^2 - 1}{\eta^2 + 2} = \frac{4}{3}\pi N\alpha \tag{3.2}$$

The dielectric constant ε_r and the refractive index η are ensemble properties which take into account the density factor $\frac{1}{N}$; the correspondent microscopic properties are respectively the dipole moment μ and the microscopic polarizability α.

Solvents	ε_r	η	P(ε_r)	R(η)
Methanol	32.7	1.328	0.91	0.20
Acetonitrile	37.5	1.344	0.92	0.21
Diethyl-ether	4.33	1.352	0.53	0.22
n-Hexane	1.89	1.375	0.23	0.23
Tetrahydrofuran	7.58	1.407	0.69	0.25
Cyclohexane	2.02	1.426	0.25	0.26
Dichloromethane	8.93	1.424	0.72	0.26
Carbon tetrachloride	2.24	1.460	0.29	0.27
Chloroform	4.81	1.446	0.56	0.27
Dimethyl sulfoxide	46.7	1.478	0.94	0.28

Table 3.1: Solvent polarity P(ε_r) and polarizability R(η) at 293 K, ordered by increasing R(η).

From equation 3.3, it appears that the square of the refractive index η^2 should equal the relative dielectric constant ε_r at wavelengths where the extinction coefficient K(ω) is zero. However, P(ε) and R(η) values reported in table 5.1 are different. Differences rise because equations 3.1 and 3.2 were originally introduced considering non-interacting spherical molecules: it is worth noting that the values of the two quantities are closer in non-polar solvents.

$$\sqrt{\varepsilon_r(\omega)} = \eta(\omega) - iK(\omega) \tag{3.3}$$

As it will be discussed later, collected data suggest a complex behavior, depending on both solvent polarity and polarizability. A classification of used solvents based directly on the dielectric constant flattens all differences in the polarizability term and allows only for the distinction between strongly polar and non-polar solvents, considering a ε_r threshold of 15 (figure 3.2 B). In this way, the polarity term of slightly polar but highly polarizable solvents such as chloroform, tetrahydrofuran, dichloro-methane and diethyl-ether results more similar to that of completely non-polar solvents (carbontetrachloride, n-hexane and cyclohexane). In order to to obtain comparable scales for polarity and polarizability, it is possible either to use a logarithmic scale or to adopt the asymptotic function 3.4. The Clausius-Mossotti and the Lorentz-Lorenz equations are formally equal to eq. 3.4.

$$\lim_{x\to\infty} \frac{x-1}{x+2} = 1 \tag{3.4}$$

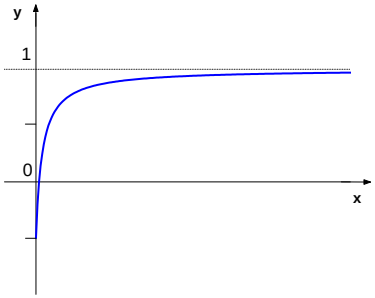

In order to discuss the effect of the different solvents on the excited state properties of *all* trans-β-apo-8'-carotenal we have divided them into different groups based on their polarity (eq. 3.1) and polarizability (eq.3.2):

- **highly polar solvents**: dimethyl-sulfoxide (circle), acetonitrile and methanol (squares).
- **polar solvents**: chloroform, tetrahydrofuran and dichloromethane (circles); dietylether (square).
- **non-polar solvents**: cyclohexane, n-hexane, carbon-tetra chloride (triangles).

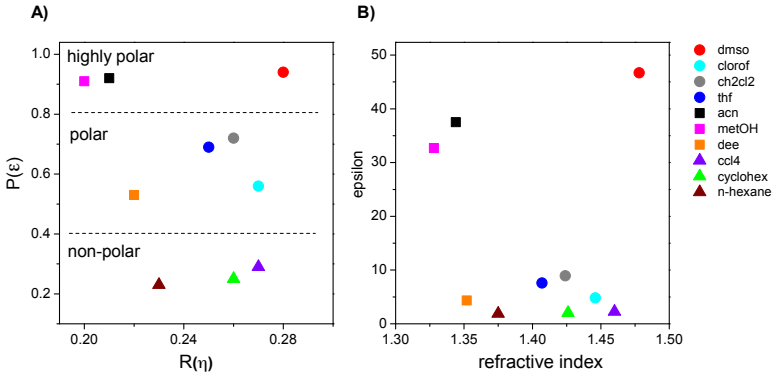

Figure 3.2: A) Classification of solvents accordingly to polarity P(ε) and polarizability R(η) by Clausius-Mossotti and Lorentz-Lorenz equations. B) The large difference in the dielectric constant ε and refractive index η scales overestimates the polarity effect.

Thresholds have been fixed at P(ε) values of 0.4 and 0.8, corresponding to ε 3 and 13.[41] Among polar solvents a further distinction between polarizable (circles) and not polarizable (squares) solvents is given. The polarizability threshold is fixed at R(η) = 0.24, in analogy with Bautista et al.[39] and according to the shift of the static maximum absorption wavelength as reported in figure 3.3.

3.2 Static UV-Vis and IR analysis

In figure 3.3 static visible absorption spectra in different solvents are reported. In case of an idealized C_{2h} symmetry, the UV-Vis absorption band corresponds to the $S_0(1A_g^-) \rightarrow S_2(1B_u^+)$ transition. As expected,[88] the maximum absorption wavelength increases with the increasing solvent polarizability, due to dispersive interactions which stabilize the ionic S_2 state respect to the S_0 state.

While in symmetric carotenoids, like in β-carotene, a linear trend of the absorption maximum with polarizability is observed, in case of asymmetric polar carotenoids, such as Peridinin, the linearity is retained only in non-polar solvents.[39] Recently,[42] it has been shown that the Peridinin absorption is a linear function of the polarizabilty only if P(ε)-R(η)$<$0.6, thus only in environments that are either non-polar or slightly polar but highly polarizable. We observed a similar behavior in *all*-trans-β-apo-8'-carotenal, although at different P(ε)-R(η) values (see figure 3.3).

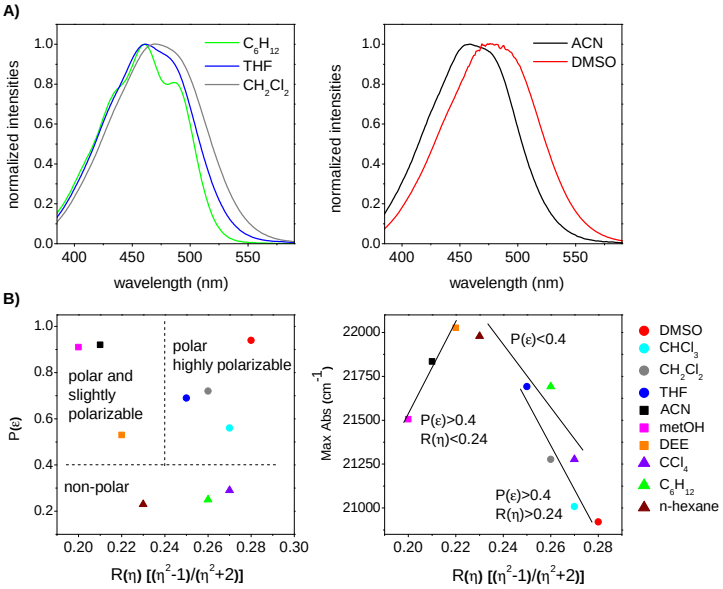

Figure 3.3: A) Left panel: static absorption spectra of all trans-β-apo-8'-carotenal in solvents with similar polarizability and different polarity. Right panel: solvents with similar polarity and different polarizability. B) Left panel: solvent groups according to polarity P(ε) and polarizability R(η). Right panel: distinct trends of the maximum absorption in various solvents as function of the solvent polarizability (see table 3.2).

On the left panel of figure 3.3 A, a polarity induced 10 nm red-shift is observed among solvents with similar polarizability (cyclohexane, dichloro-methane and THF). The right panel reports the absorption spectra in two highly polar solvents (ACN and DMSO) differing in polarizability. In the more polarizable DMSO the spectrum red-shifts by 20 nm, showing that the solvent induced stabilization on the S_2 state is mainly regulated by polarizability. In figure 3.3 B, when $R(\eta)>0.24$ the peak frequency decreases with increasing polarizability. In polar and slightly polarizable solvents, however, the absorption energy strikingly increases. Evidently, more complicated and specific solute-solvent interactions occur in lowering the excited state energy (e.g. hydrogen bonds in methanol).

Solvents	ω_{maxass} (cm^{-1})
Methanol	21505
Acetonitrile	21834
Diethyl-ether	22026
n-Hexane	21978
Tetrahydrofuran	21692
Cyclohexane	21692
Dichloromethane	21277
Carbon tetrachloride	21277
Chloroform	21008
Dimethyl sulfoxide	20920

Table 3.2: Frequency position of the static Vis maximum absorption.

In table 3.2 we report the values of the maximum absorption at the Franck-Condon transition, generally not coincident with the 0-0 transition. This is evident in the case of non-polar solvents, as in cyclohexane (figure 3.3 A), where a vibronic structure in the absorption band is clearly visible. The horizontal displacement of the minimum of the S_2 potential energy surface (PES) with respect to the minimum of the S_0 PES suggests that a geometrical rearrangement occurs at the relaxed excited state. In polar solvents, the static

absorption band broadens and the vibronic structure is lost. The band appears asymmetrically broadened on the red-tail, which is most likely due to the presence of slightly different conformers in the ground state[35]. This asymmetric red-tail has been observed also in case of non-carbonyl carotenoids. In case of β-carotene, it has been attributed to the presence of multiple orientations of the terminal β-rings with respect to the conjugated C=C chain.[12] The most stable conformer was calculated to have the double bond on the β-ring in s-cis configuration with respect to the chain.[89]

The assignment, reported in literature, of the vibrational modes active in the IR spectrum of carotenoids and polyenes in the ground state is unambiguous for the 6 μm region.[33,45] Four bands are present in the spectral region between 1450 and 1800 cm^{-1}. Figure 3.4 shows the FT-IR spectra in cyclohexane and in chloroform. The narrow C=O stretching mode at 1680 cm^{-1} in cyclohexane down-shifts by 20 cm^{-1} in the more polar chloroform, where it significantly broadens (FWHM goes from 17 to 25 cm^{-1}). In the 1550-1650 cm^{-1} region, two bands have been assigned to two asymmetric C=C stretching modes and, finally, at 1525-1530 cm^{-1}, the symmetric C=C stretching mode has been assigned, as also confirmed by Raman experiments.[60,61,90]

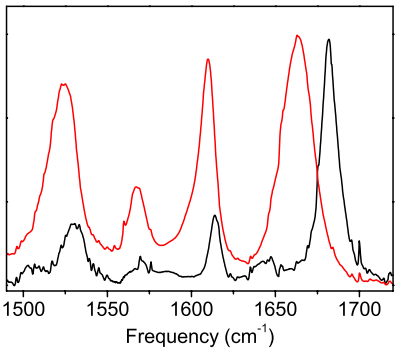

Figure 3.4: FT-IR spectra in chloroform (red line) and cyclohexane (black line).

3.3 Transient UV-Vis analysis

Transient visible spectra change remarkably with solvents.[91] All the spectra shown (figure 3.5) present a negative signal below 500 nm, due to the ground state bleaching and to the stimulated emission from the bright S_2 state at early pump-probe delays, and a positive signal at longer wavelengths. The position of the most intense positive excited state absorption (ESA) band depends on the solvent. As also observed for the ground state, this absorption gradually red-shifts as the solvent polarizability increases (558 nm in ace-

tonitrile and 573 nm in chloroform and DMSO), while the solvent polarity has only a minor effect on its position (the band is peaked at 557 nm both in cyclohexane and acetonitrile). This band is commonly assigned to the $S_1(2A_g^-) \rightarrow S_n(nB_u^+)$ transition. Besides this band, a shoulder on its blue-side and other positive components above 600 nm are visible.

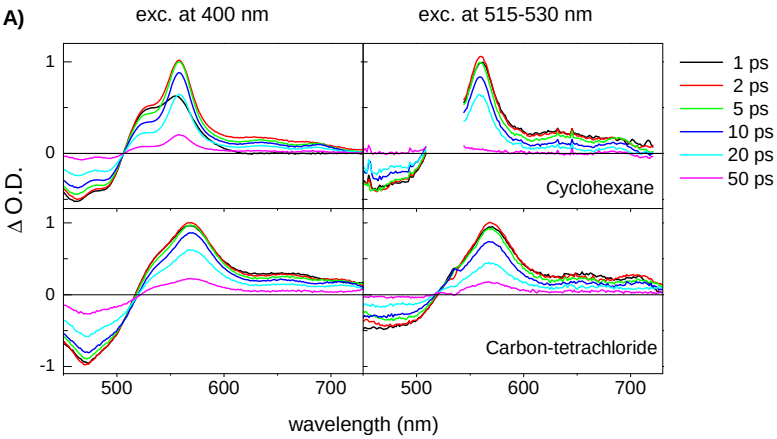

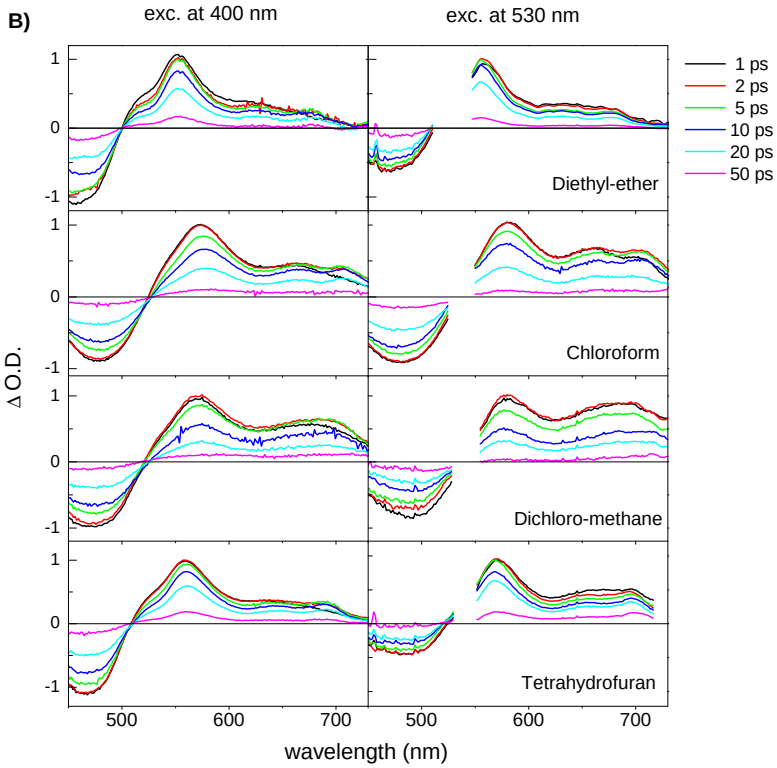
B)
exc. at 400 nm
exc. at 530 nm
1 ps
2 ps
5 ps
10 ps
20 ps
50 ps
Diethyl-ether
Chloroform
Dichloro-methane
Tetrahydrofuran
Δ O.D.
wavelength (nm)
1
0
-1
500
600
700

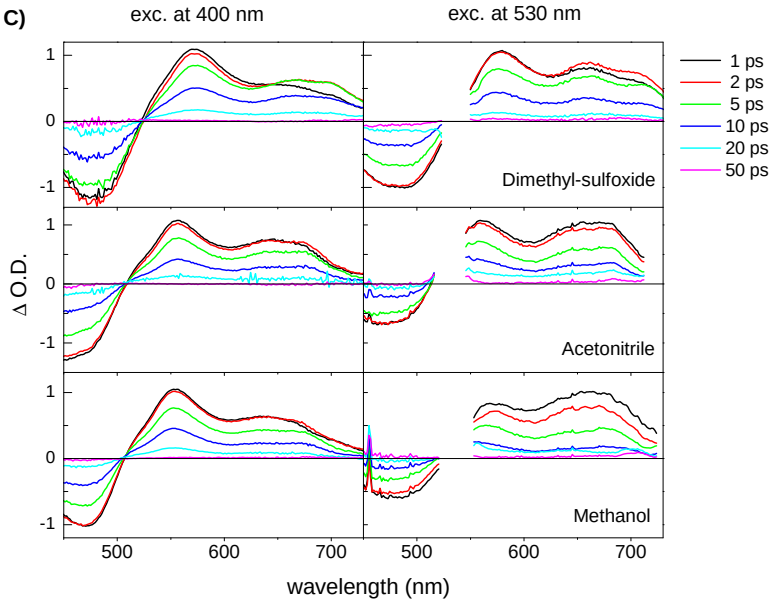

Figure 3.5: Transient Uv-Vis absorption spectra reported at different pump-probe delays in A) non-polar, B) polar and C) highly polar solvents.

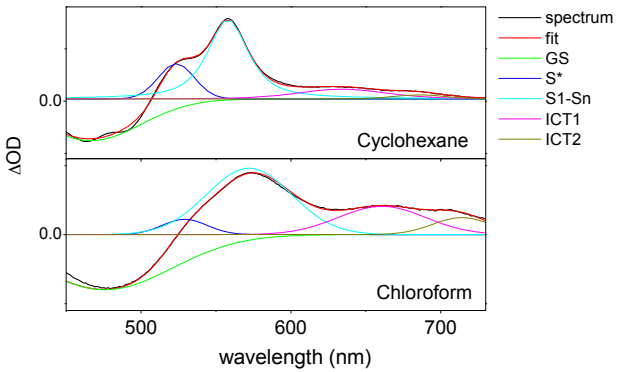

Figure 3.6: Gaussian fit of transient UV-Vis absorption spectra recorded at 2 ps pump-probe delay, upon 400 nm excitation, in two representative solvents: cyclohexane (non polar) and chloroform (polar and polarizable).

The curve fitting (figure 3.6), with a combination of Gaussian profiles, shows that a positive band on the high-energy side of the main ESA band and two positive bands above 600 nm are needed to reproduce the spectral shape of the transient signal. The shoulder on the blue-side, often attribute to some other, not well characterized, S* excited state, was observed in many non-carbonyl open chain carotenoids and in β-carotene,[31,92] but its nature is still matter of debate. Twisted conformers, ground state hot bands, presence of dark

states have been invoked to explain its origin. Many experimental indications suggest that this band is associated to the formation of a triplet state in LH complex-bound carotenoids,[23,93,94] however it has been also demonstrated that in carotenoids no appreciable triplet states are formed in solution.[29] As for the positive bands above 600 nm, the reported data unequivocally show that their intensity is strongly sensitive to the solvent, and that it is enhanced in solvents with high polarity. Two bands are easily recognized in non-polar and slightly polar solvents, while a unique broad band is visible in highly polar solvents. The position of the bands in the high wavelength region shifts according to solvent polarizability, similarly to what observed for the $S_1 \rightarrow S_n$ ESA band. The enhanced intensity in polar solvents, together with the shortening of the excited state lifetime (see also figure 3.7), confirms previous assignment of this ESA to the ICT$\rightarrow S_{n'}$ transition.

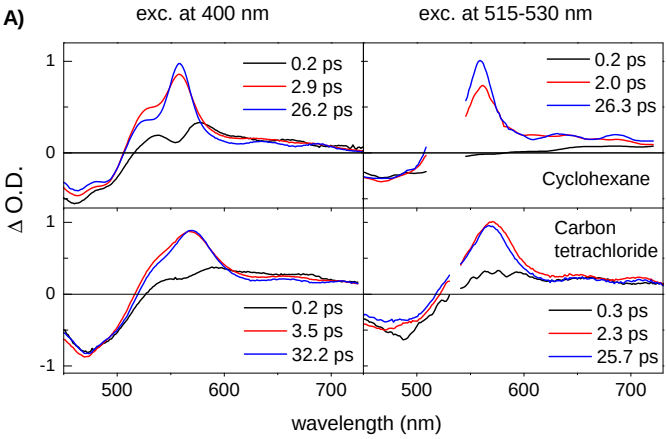
A)
exc. at 400 nm
exc. at 515-530 nm
0.2 ps
2.9 ps
26.2 ps
0.2 ps
2.0 ps
26.3 ps
Cyclohexane
Carbon
tetrachloride
0.2 ps
3.5 ps
32.2 ps
0.3 ps
2.3 ps
25.7 ps
Δ O.D.
wavelength (nm)

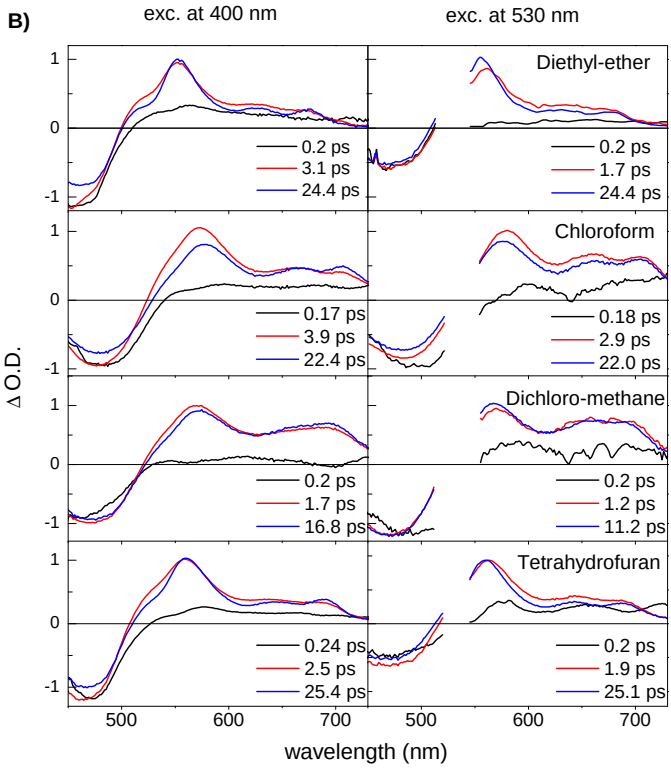
B)
exc. at 400 nm
exc. at 530 nm
Diethyl-ether
0.2 ps
3.1 ps
24.4 ps
0.2 ps
1.7 ps
24.4 ps
Chloroform
0.17 ps
3.9 ps
22.4 ps
0.18 ps
2.9 ps
22.0 ps
Dichloro-methane
0.2 ps
1.7 ps
16.8 ps
0.2 ps
1.2 ps
11.2 ps
Tetrahydrofuran
0.24 ps
2.5 ps
25.4 ps
0.2 ps
1.9 ps
25.1 ps
Δ O.D.
wavelength (nm)

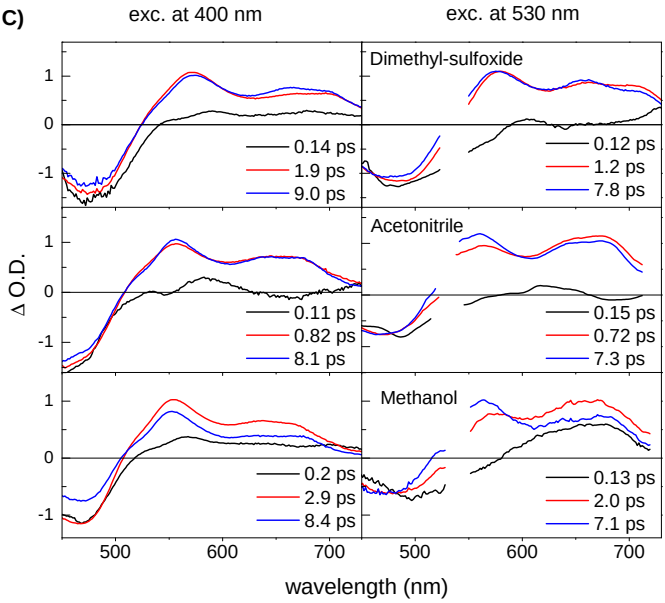

Figure 3.7: Global analyzed transient Uv-Vis absorption spectra in A) non-polar, B) polar and C) highly polar solvents.

In order to investigate the nature of the ICT state, we performed experiments at two excitation wavelengths: at 400 nm, to deposit an excess of vibrational energy in the S_2 state, and at 515-530 nm, tuning the excitation on the very red tail

of the static absorption spectrum in each solvent. Measured transient spectra look qualitatively similar (figure 3.5), however slightly faster dynamics and relatively more intense ICT bands with respect to the S_1 absorption are observed when the excitation is on the red-side of the absorption spectrum.

Differences in the spectral evolution depending on both polarity and polarizability are directly observed in the reported transient spectra. Those differences are better highlighted if we consider the evolution associated difference spectra (EADS) resulting from the global analysis and reported in figure 3.7. Global analysis was performed after SVD decomposition and by assuming first-order kinetics; a three-exponential sequential model was applied (only in few cases a forth exponential was added). Although the Glotaran fitting algorithm takes into account the frequency-dispersed instrumental response function, still the latter can affect the spectral shape of the first EADS. Thus, in some cases, the first time constant was fixed to a 0.2 ps value. In all cases, we observe a very fast sub-picosecond component, followed by an intermediate 2-4 ps contribution, corresponding to the simultaneously rise of the S_1 and ICT excited state bands. A third longer timescale component is finally present, whose exact time constant is highly dependent on the solvent polarity and goes from 25 ps in non-polar solvents up to 8 ps in polar ones.

In non-polar solvents (figure 3.7 A) the intensity of the ICT bands is about 16% of the intensity of the main ESA band at 557 nm in the second spectral component. These bands decay on a 3 ps timescale, while the S_1 band rises in intensity and blue-shifts: this behavior can be associated to vibrational cooling in the S_1 state. In carbon-tetrachloride, all bands are broader compared to cyclohexane, because of the slightly higher polarity.

In the slightly polarizable diethyl-ether (figure 3.7 B), the spectral evolution is similar to what observed in non-polar solvents, while in solvents with similar polarity but higher polarizability, such as chloroform, THF and dichloro-methane, differences are remarkable. In these cases, the relative intensity of ICT bands with respect to the S_1-S_n absorption is 30-80% in the second EADS, with even higher values when the excitation is at 530 nm. Moreover, upon 400 nm excitation, the ICT absorption shows a 2-3 ps rising component while the S_1 band decays.

In highly polar solvents (figure 3.7 C), above the remarkable shortening of the long living component, intense ICT bands are generally observed within the first picosecond. Their relative intensity with respect to the S_1 band is always above the 60% and, when the excitation is at 530 nm in methanol and acetonitrile, the ICT bands are even more intense than the S_1 absorption. While the polarizable DMSO behaves sim-

ilarly to chloroform, with an increase of the ICT absorption intensity on a 1-2 ps timescale, in acetonitrile, methanol and diethyl-ether the spectral evolution is minimal and goes in the opposite direction: in the first few picoseconds, the ICT bands decay while S_1 absorption rises.

In order to highlight the polarizability effect on the 1-3 ps timescale, kinetic traces at the S_1 and ICT absorption wavelengths are reported in figure 3.8 for chloroform and diethyl-ether solutions, where this effect seems to be magnified.

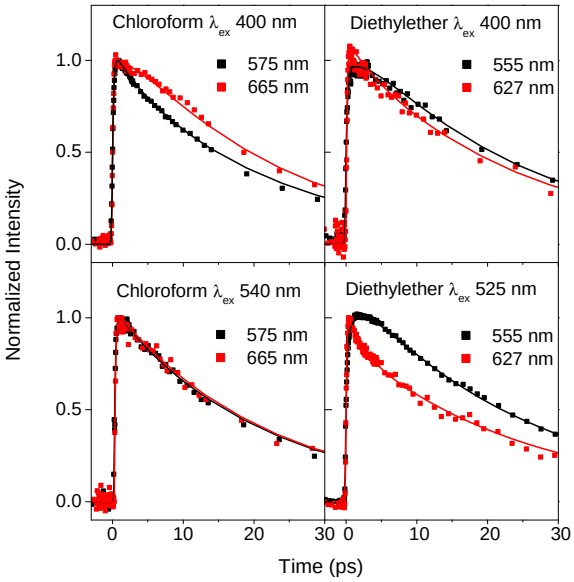

Figure 3.8: Kinetic traces of the S_1 and ICT excited state absorption bands in chloroform and diethyl-ether, respectively at 575-555 nm and 665-627 nm (scattered points) and related fits from global analysis (solid lines).

3.4 Transient IR analysis

As we reported in a previous paper,[33] the transient infrared spectrum of the *all* trans-β-apo-8'-carotenal in cyclohexane and chloroform, upon 400 nm excitation, undergoes large changes when the pump-probe delay varies. Here we extend the investigation to several other solvents and at two excitation wavelengths, with the intent of better understanding the nature of the ICT state and the mechanisms of its formation. Transient IR spectra measured in all analyzed solvents are reported in figure 3.9.

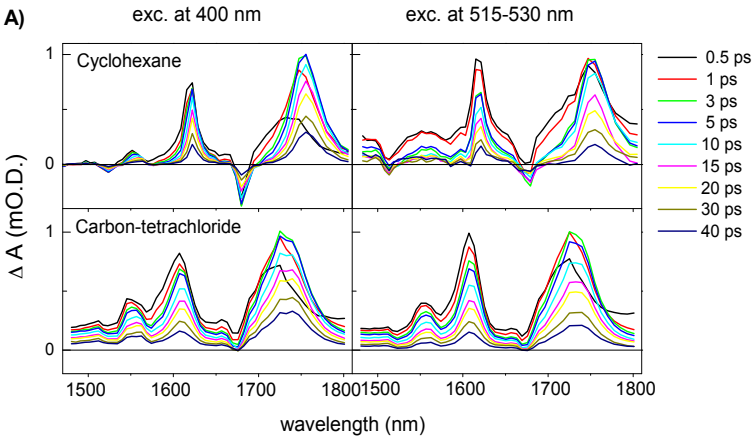

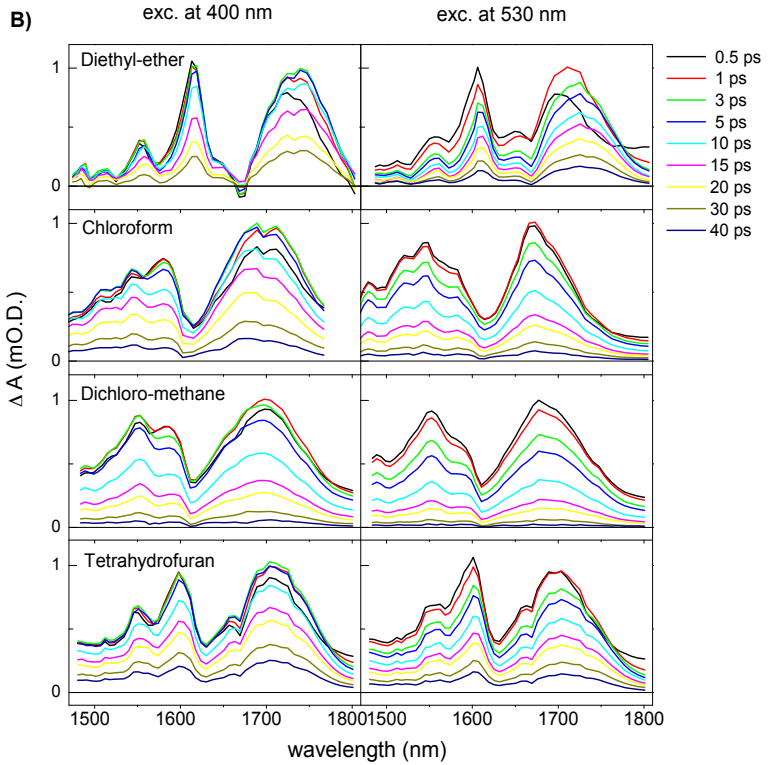
B)
exc. at 400 nm
exc. at 530 nm
Diethyl-ether
Chloroform
Dichloro-methane
Tetrahydrofuran
0.5 ps
1 ps
3 ps
5 ps
10 ps
15 ps
20 ps
30 ps
40 ps
Δ A (mO.D.)
wavelength (nm)
1500
1600
1700
1800
0
1

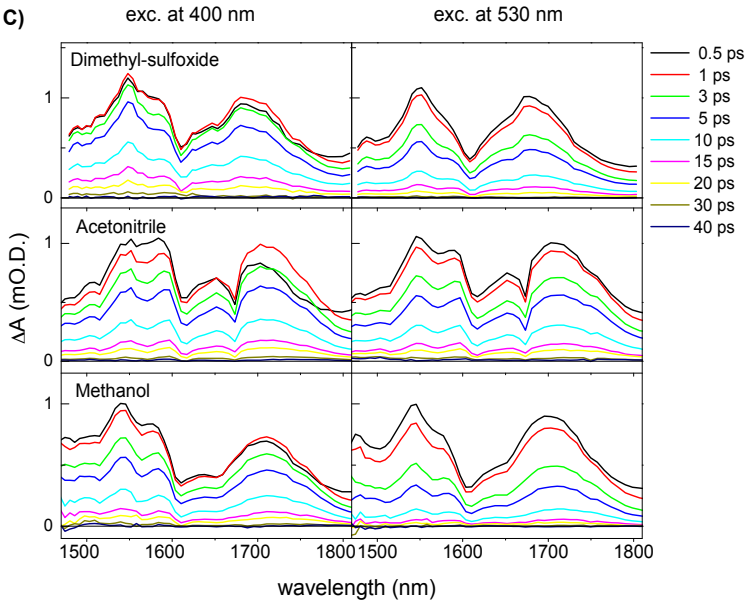

Figure 3.9: Transient IR absorption spectra in A) non-polar, B) polar, C) highly-polar solvents.

From the FTIR spectrum in cyclohexane (figure 3.4) we know that the C=O stretching is at 1680 cm^{-1}; at 1615 and 1565 cm^{-1} there are two C=C asymmetric stretching modes of the chain and at 1530 cm^{-1} the symmetric one; in polar

solvents all modes down-shift by about 20 cm^{-1}. Ground state vibrations are expected to appear as negative bands on transient spectra, as observed in cyclohexane for the C=O and the symmetric C=C stretching (figure 3.9 A). Nonetheless, in more polar solvents they only appear as weak dips on an overall positive transient signal.

The IR mode activity upon visible excitation is related to the perturbed electronic charge density distribution. Depending on where the charge accumulates, vibrational modes of specific functional groups can equally up or down-shift with respect to the ground state frequency position. Our measurements[33,69] and literature data[61,90] suggest that the excited state C=O stretching mode down-shifts by about 40 cm^{-1}, while the symmetric C=C stretching mode up-shifts more than 100 cm^{-1} in the 1700 cm^{-1} region, where no ground state modes are present. The assignment in the overcrowded lower frequency part of the spectrum is not straightforward, because of many excited state chain modes[95] and dips caused by ground state vibrations.

Due to its large sensitivity to solvent polarity, the 1700 cm^{-1} band is the most informative regarding the excited state dynamics of the system and the ICT formation.

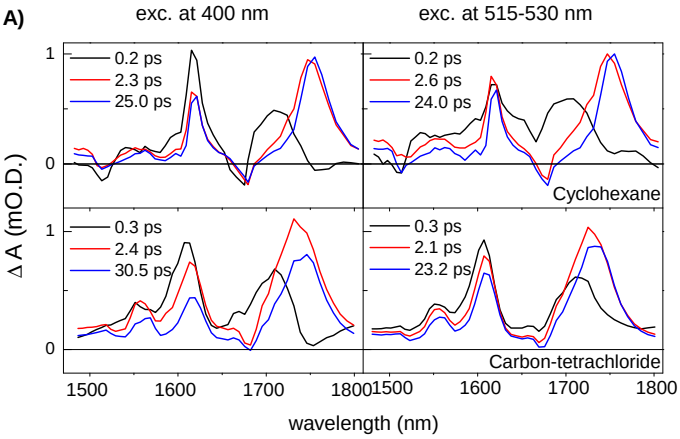
A)
exc. at 400 nm
exc. at 515-530 nm
0.2 ps
2.3 ps
25.0 ps
0.2 ps
2.6 ps
24.0 ps
Cyclohexane
0.3 ps
2.4 ps
30.5 ps
0.3 ps
2.1 ps
23.2 ps
Carbon-tetrachloride
Δ A (mO.D.)
1
0
1
0
1500
1600
1700
1800
1500
1600
1700
1800
wavelength (nm)

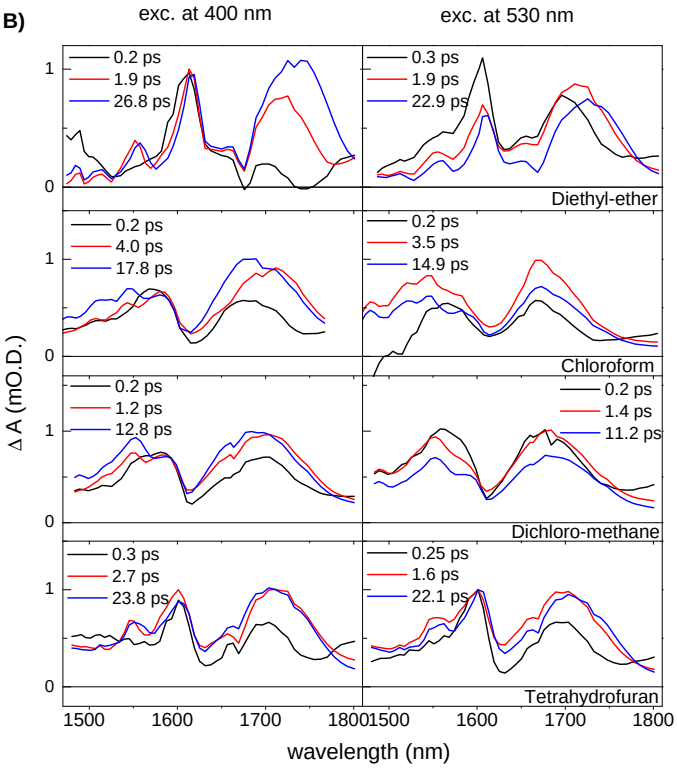
B)
exc. at 400 nm
exc. at 530 nm
0.2 ps
1.9 ps
26.8 ps
0.3 ps
1.9 ps
22.9 ps
Diethyl-ether
0.2 ps
4.0 ps
17.8 ps
0.2 ps
3.5 ps
14.9 ps
Chloroform
0.2 ps
1.2 ps
12.8 ps
0.2 ps
1.4 ps
11.2 ps
Dichloro-methane
0.3 ps
2.7 ps
23.8 ps
0.25 ps
1.6 ps
22.1 ps
Tetrahydrofuran
Δ A (mO.D.)
wavelength (nm)
1500
1600
1700
1800
0
1

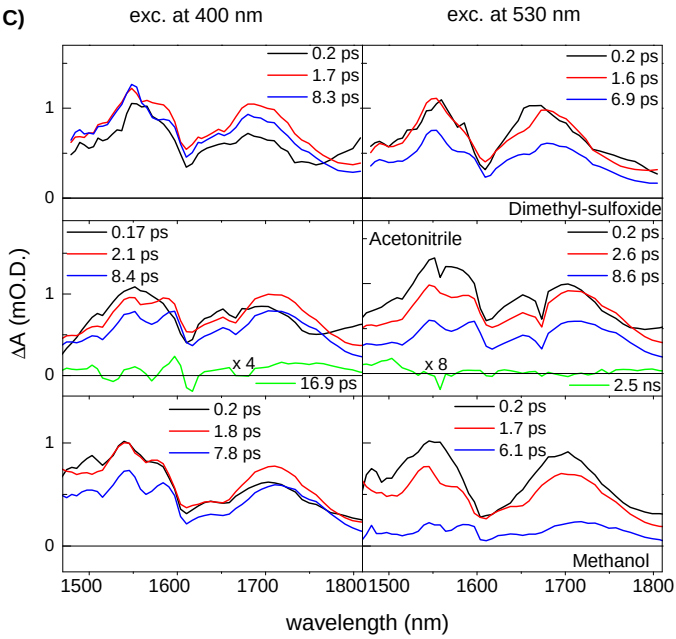

Figure 3.10: Transient IR absorption spectra in A) non-polar solvents, B) polar solvents, C) highly polar solvents.

In non-polar solvents (figure 3.9 A and 3.10 A), this band is quite narrow, peaked at 1755 cm^{-1} and shows a limited time evolution.The minor blue-shift observed on a 2-3 ps timescale

can be related to vibrational cooling on the $S_1(2A_g^-)$ state. Within the first picosecond, a broad band around 1735 cm^{-1} is visible right after excitation, which is likely due to the symmetric C=C stretching in the S_2 state. This band, which is clearly distinguishable in the spectrum recorded in cyclohexane exciting at 400 nm, is evident in the first EADS of all analyzed solvents. In agreement with calculations,[33] the C=C stretching mode up-shifts in the ionic $S_2(1B_u^+)$ state less than in the covalent $S_1(2A_g^-)$ state.

In polar solvents (figure 3.9 B), this band shifts appreciably to lower frequencies. In the polar and slightly polarizable diethyl-ether, the high-frequency band is significantly broad and a double peak can be observed at 1720 and 1745 cm^{-1}. Looking at the low-frequency part of the spectrum, bands are as narrow as in cyclohexane. From the global analysis (figure 3.10 B), a progressive evolution toward higher frequencies with a shift of more than 20 cm^{-1} is visible on a 2 ps timescale, at both excitation wavelengths. In the more polarizable chloroform, THF and dichloro-methane, the opposite behavior is observed, especially upon 400 nm excitation. All bands are broad and the band-shape significantly changes with the excitation wavelength. Exciting at 400 nm, the band above 1700 cm^{-1} first moves to the blue on a sub-picosecond timescales and then to the red (around 1680 cm^{-1}) on the 2-4 ps timescale. It finally decays to the ground state with a *ca* 15-20 ps time constant. At 530 nm, similarly to

what observed in the visible measurements, all dynamics are slightly faster, however the observed band-shape evolution around 1700 cm^{-1} is minimal. The excited state C=C band is as broad as upon 400 nm excitation but it is asymmetrically peaked on its low-energy side already at early pump-probe delays. From global analysis, only a minor blue-shift between the 2^{nd} and the 3^{rd} EADS due to the vibrational cooling can be appreciated.

In highly polar solvents (figure 3.9 C and 3.10 C) the last spectral component is remarkably faster. Although in DMSO it is still possible to observe a change in the band shape at different excitation wavelengths (see figure 3.11), similarly to what observed in slightly polar but polarizable solvents, in highly polar but less polarizable solvents like ACN and methanol the broad and structureless bandshape is the same at both excitation wavelengths. The evolution in these solvents is minimal and only a minor blue-shift, ascribable to vibrational cooling, is visible on a 2 ps timescale. As reported for other carbonyl carotenoids,[54] the broadening of vibrational bands in highly polar solvents is due to the presence of a distribution of conformers in the ground state, which are stabilized by specific dipole-dipole interactions or by H-bonds in protic solvents.

The effect of the excitation wavelength on the spectral shape is better shown in figure 3.11 for three representative

solvents: cyclohexane (non-polar), chloroform (polar and polarizable) and DMSO (highly polar).

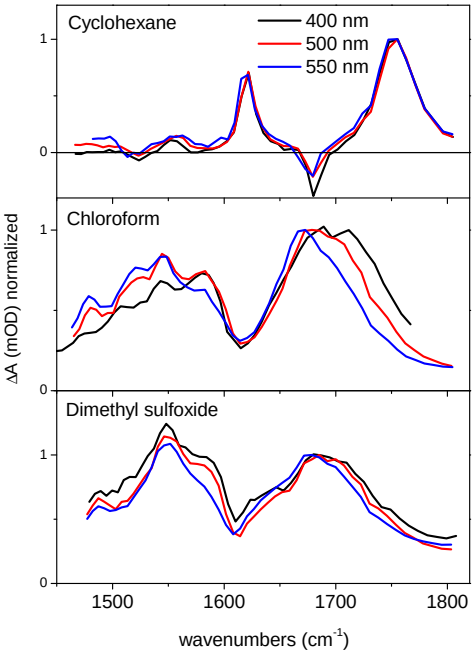

Figure 3.11: Effect of excitation wavelength on transient infrared spectra registered in cyclohexane and chloroform at 3 ps pump-probe delay and in DMSO at 1 ps pump-probe delay. All spectra are normalized on the 1680-1700 cm^{-1} band.

In figure 3.11, samples were excited on the red and blue tails of the static absorption spectrum, respectively at 400 and 530-550 nm, and close to the maximum absorption around 500 nm. At increasing excitation wavelength, thus moving to the red-side of the absorption band, a broadening on the low-frequency side of the 1700-1750 cm^{-1} band is hardly detectable in cyclohexane, more appreciable in DMSO and definitely evident in chloroform.

The spectral evolution and the large excitation wavelength dependence observed in slightly polar solvents suggest that two bands, with different rising times, are hidden under the broad envelope of the 1700 cm^{-1} band. In order to confirm the presence of two bands around 1700 cm^{-1} and highlight the opposite kinetic behavior occurring in polar solvents with different polarizability, kinetic traces in chloroform and diethyl-ether taken at the two sides of the band are reported in figure 3.12. A similar kinetic behavior was observed on the S_1 and ICT excited state absorption maxima in transient visible measurements (figure 3.8). Comparing IR and the VIS kinetic traces, it is possible to assign the higher-frequency IR component in the 1700 cm^{-1} region to the C=C stretching of the $S_1(2A_g^-)$ state and the lower-frequency component to the same vibration in the ICT state. It is worth pointing out that the latter has a very similar frequency position to that previously attributed to the $S_2(1B_u^+)$ state.

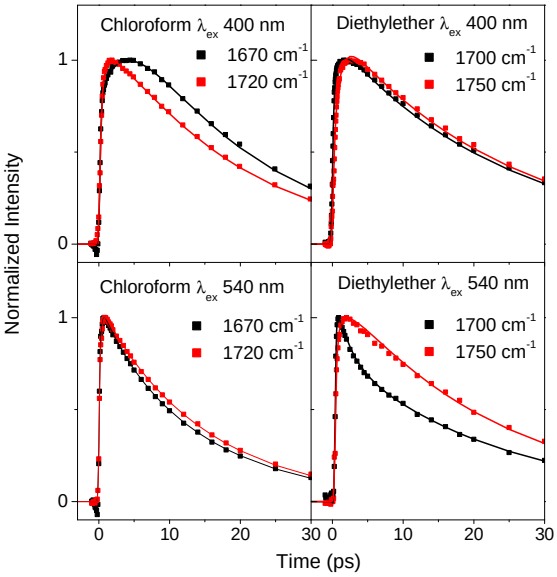

Figure 3.12: Kinetic traces at the two sides of the excited state C=C symmetric stretching band around 1700 cm^{-1} in chloroform and diethyl-ether (scattered points). Fitting curves from global analysis are reported as solid lines.

3.5 Excited state vibrational mode assignment

In the previous paragraph we pointed out that the most informative spectral region to follow excited dynamics in the IR is that where the C=C and C=O stretching modes appear.

Harmonic vibrational frequencies for the carbonyl and for the symmetric C=C stretching modes were previously calculated in the ground and low-lying excited states.[33] According to those results, the carbonyl mode is expected to down-shift in both $1B_u^+$ and $2A_g^-$ states, while the C=C symmetric stretching mode should up-shift more than 150 cm^{-1} in the $2A_g^-$ state and only 50 cm^{-1} in the $1B_u^+$ state.

In the following, we bring new experimental evidences which confirm previous assignment. We carried out Vibrational IR Labeling and Transient Stimulated Raman experiments in order to localize, respectively, the IR active C=O and the Raman active C=C symmetric stretching modes in the excited state. We repeated the measurement in a polar (chloroform) and in a non-polar (cyclohexane) medium.

3.5.1 IR Labeling

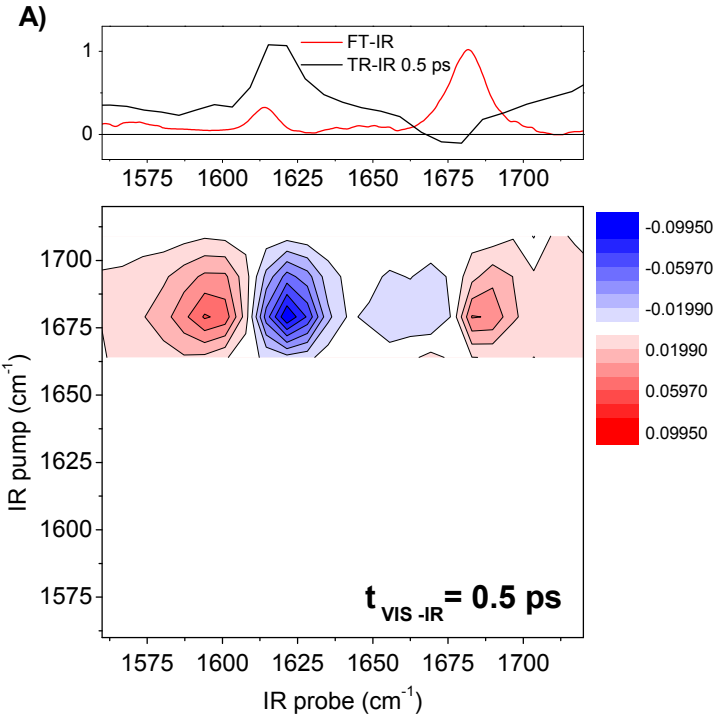

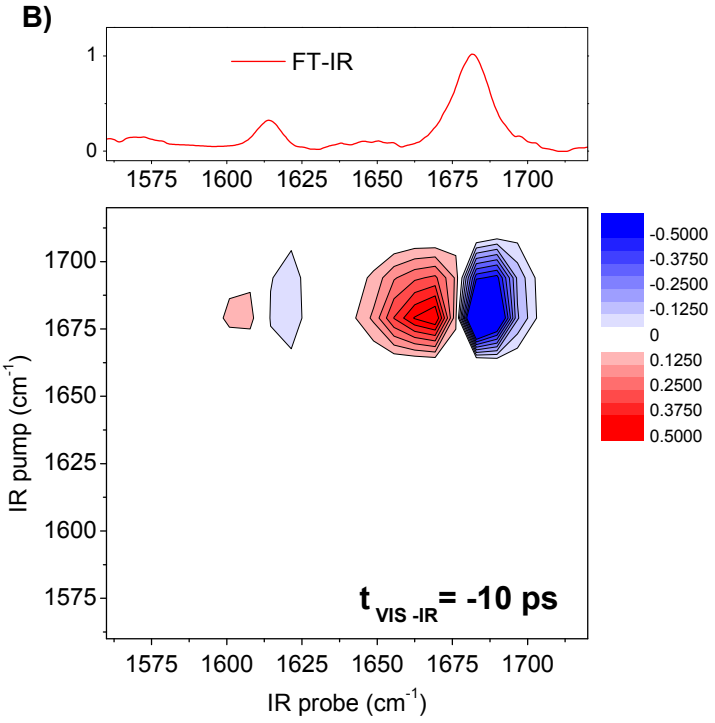

Figure 3.13: A) IR labeling spectrum of *all* trans-β-apo-8' carotenal in cyclohexane, recorded at 0.5 ps from the visible excitation at 530 nm. On top, the corresponding FT-IR spectrum and the linear transient IR signal at 0.5 ps. B) Background spectrum taken at $t_{VISpump-IRprobe}$= -10 ps, which corresponds to the ground state 2D-IR spectrum at 1 ps from the IR excitation.

Figure 3.13 A reports the 2D-labeling spectrum of the C=O stretching mode in the *all* trans-β-apo-8' carotenal in cyclohexane, registered exciting the sample in the visible at 530 nm. As previously discussed (see paragraph 2.5.2), the IR labeling technique is included among 5^{th} order spectroscopies, with three beams impinging on the sample from different directions. The pulse sequence used in the experiment is shown in figure 2.9. Both infrared and visible excitations precede the probe pulse.

As in a 1D transient IR measurement performed on a vibrationally hot ground state, the C=O stretching ground state mode at 1680 cm^{-1} (figure 3.13 B) is selectively excited. After 0.5 ps, the visible pump promotes population to an electronic excited state starting from an out-of-equilibrium ground state, where vibrational cooling has not completed yet. Within the vibrational lifetime, it is thus possible to look for the same mode in the excited state.

Like in a 2D-IR experiment, time resolution depends on the Fourier Transform of the IR pump bandwidth (*ca* 17 cm^{-1} $\approx$800 fs), which has been made narrow by a Fabry-Perot interferometer and whose frequency has been tuned throughout the C=O band. The delay between IR pulses was set at 1 ps and never changed, while the delay between the Vis pump and the IR probe was scanned from negative time delays (figure 3.13 B) up to + 0.5 ps, with the Vis excitation

falling in between of IR pulses (spectrum A). Finally, a broad band IR pulse probes the perturbed system in the 1560-1720 cm^{-1} region.

In figure 3.13 A, results are reported after background subtraction (fig. B). At negative time delays, before the visible excitation, all the population is in the relaxed ground state. For this reason, diagonal ground state peaks have an inverted sign in the double difference spectrum at positive time delays. The corresponding excited state mode is expected to show up in the off-diagonal region, with regular signs: blue for the excited state bleaching and stimulated emission, red for the vibrational excited state absorptions. Figure 3.13 A , reporting the spectrum registered 0.5 ps after the VIS excitation, shows that an off-diagonal peak is indeed observed and assigned to the C=O stretching in the excited state. In the same figure we notice that it down-shifts from 1680 to 1620 cm^{-1} in the excited state, confirming the assignment of the excited state C=O stretching to 1620 cm^{-1} in transient IR spectra in non-polar solvents and in diethyl-ether. Due to solvent polarity, the same excited state mode is expected to down-shift to $\sim$1600 cm^{-1} in polar solvents.

The FT-IR spectrum in the upper panel of figures 3.13, shows that the asymmetric C=C stretching mode at 1615 cm^{-1} is almost coincident with the excited state C=O mode. The off-diagonal peak observed in the background spectrum

reported in figure 3.13 B can be attributed to the coupling of the carbonyl stretching mode to the C=C asymmetric stretching. Figure 3.14 compares the signal at negative time delays (black line), where all population is in the ground state, to that measured at positive delays (red line), where contributions from both the ground and excited states are present. Upon background subtraction (red line minus black line), in the off diagonal region, around 1620 cm^{-1}, the intensity of the ground state cross peak is overestimated, because at positive time delays part of the population is not anymore at the ground state but it has been promoted to the excited state by the visible excitation. Therefore, the excited state C=O mode reported in figure 3.13 A should be even more intense. In order to estimate the amount of the visible excited population, we looked at the diagonal peak. At 1680 cm^{-1}, the bleaching intensity of the ground state mode reduces of 5% after the visible arrival. Spectra at positive delays should be subtracted of a background whose intensity is reduced of 5% to completely eliminate ground state contributions.

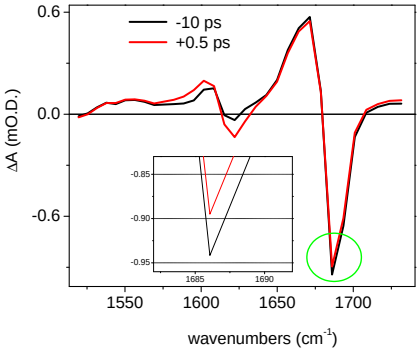

Figure 3.14: Background of the labeling experiment recorded at t_{VIS-IR}= -10 ps (black line) and labeling signal at t_{VIS-IR}= +0.5 ps (red line). Both epsctra have been acquired with a narrowband IR pump centered at 1680 cm^{-1}.

We repeated the same experiment in chloroform. The FTIR spectra (figure 3.4) shows that infrared transitions are sensitive to solvent polarity and that the down-shift is about 20 cm^{-1}.

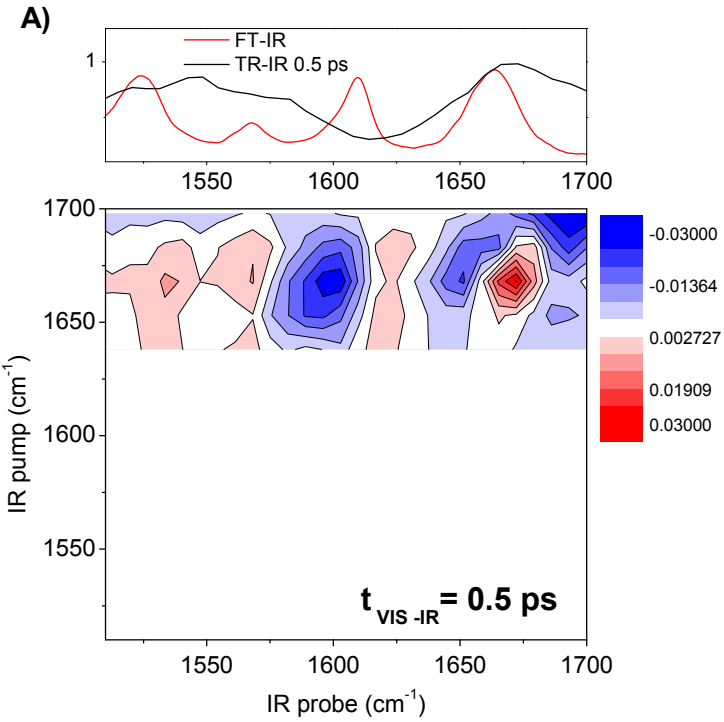

In figure 3.15 we report the labeling spectra measured in chloroform. While in cyclohexane the transient shape of the C=O excited state band is well defined, with both positive and negative parts of the signal well distinguishable (see

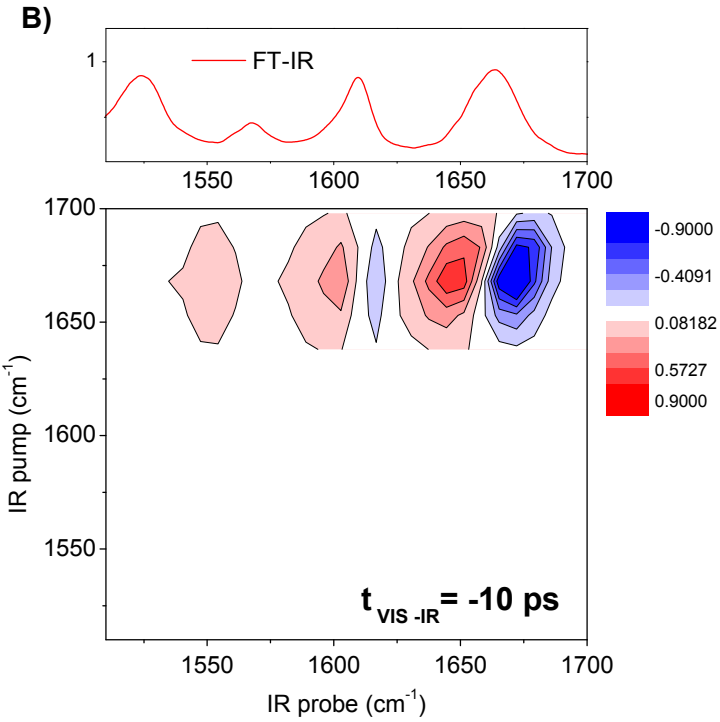

Figure 3.15: A) IR labeling spectrum of *all* trans-β-apo-8' carotenal in chloroform, recorded at 0.5 ps from the visible excitation at 530 nm. On top, the correspondent FT-IR spectrum and the linear transient IR signal at 0.5 ps. B) Corresponding background spectrum taken $t_{VISpump-IRprobe}$= -10 ps.

fig.3.13 A), in chloroform only the negative part of the signal appears. Actually, similarly to the corresponding mode in the ground state, the excited state C=O band is expected to be quite broad. In addition, the spectrum in chloroform is much more congested. In fact, in the ground state, two cross peaks due to coupling of C=O and C=C stretching modes are observed at 1610 and 1570 cm^{-1} (figure 3.15 B). In the excited state, the upshifted C=C symmetric stretching partially overlaps to the ground state C=O band (see the black line reported on top of fig. 3.15 A). All this spectral congestion complicates the assignment and hides the positive lobe of the off-diagonal excited state C=O at positive delays. In any case, the comparison with the spectrum recorded in cyclohexane suggests that upon visible excitation the C=O stretching down-shifts from 1680 cm^{-1} in the ground state to ca. 1600 cm^{-1} in the excited state. We identify it with the intense negative signal at 1600 cm^{-1}, which shows two lateral weak positive features that we attribute to overlapping off-diagonal C=O/C=C cross peaks in the ground state. These positive bands almost disappear when we correct for the excited state population. As shown in cyclohexane, here the visible excitation induces a 2.6% of ground state bleaching.

3.5.2 Transient Stimulated Raman

In figure 3.16, the ground state stimulated Raman spectrum of apo-8'-carotenal recorded in cyclohexane and in chloroform in the 6 μm region is reported. The most intense band is observed at 1524 cm^{-1} in cyclohexane and at 1516 cm^{-1} in chloroform and assigned to the symmetric C=C stretching mode of the polyene chain.

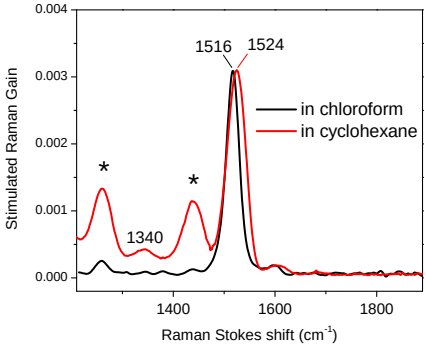

Figure 3.16: Stimulated Raman spectra of *all* trans-β-apo-8' carotenal in cyclohexane (red line) and in chloroform (black line). Solvent transitions are marked with an asterisk (*).

Thanks to the high temporal resolution reached by Femtosecond Stimulated Raman Spectroscopy, it is possible to trace the C=C frequency position as the electronic energy relaxation proceeds. In figure 3.17 we report Transient Stimulated Raman spectra recorded within the first picosecond from the 400 nm actinic excitation, which excites molecules to the hot $S_2(1B_u^+)$ state. The reported spectra have been calibrated using the 1444 and 1266 cm^{-1} cyclohexane transitions as inner standard. We corrected the spectra by subtracting a negative spectral component due to the presence of an underlying transient absorption signal. If this latter is simultaneously recorded (by changing the position of the chopper and closing the Raman pump beam) and then subtracted, still the baseline results partially altered.

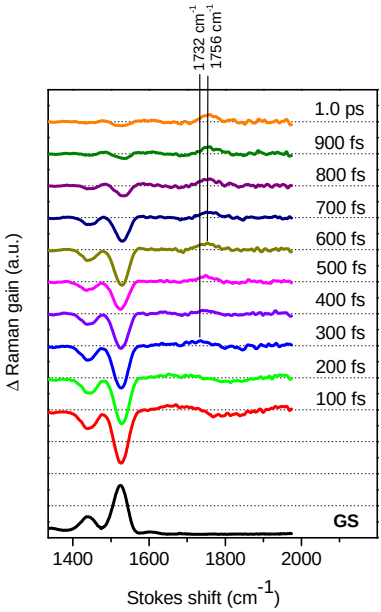

Figure 3.17: Femtosecond stimulated Raman spectra of *all* trans-β-apo-8' carotenal in cyclohexane, at different delays from the 400 nm actinic excitation and within the 1 ps of evolution.

In figure 3.17, a spectral evolution within the first picosecond is observed. The negative peak at 1524 cm^{-1} corresponds to the symmetric C=C stretching mode in the ground state. At 1444 cm^{-1} a solvent band is also visible, due to the change

in the molecular density factor caused by a local heating on the laser spot. At positive delays, after about 500 fs from the actinic excitation, a positive peak is clearly distinguished around 1756 cm^{-1}. On shorter timescales, instead, a broad dispersive line shape is present around 1732 cm^{-1}.

In chapter 2 we noticed that Raman bands have a dispersive line shape when their vibrational dephasing time is comparable or even longer than the time constant of the electronic relaxation.[85,86] Since the photo-excited S_2 state rapidly decays to S_1 with a $\approx$ 200 fs time constant comparable to (and probably shorter than) the vibrational lifetime, the 1732 cm^{-1} band can be reliably attributed to a vibration in the S_2 state. Due to the very short lifetime of the electronic state, this vibration evolves toward higher frequencies, finally acquiring a symmetric line shape, that we attribute to the same mode in the long living S_1 state ($\tau \approx$25 ps). In order to compare Raman and Infrared results (see transient IR measurements recorded in cyclohexane upon 400 nm excitation, figure 3.9 A), in figure 3.17 the 1732 and 1756 cm^{-1} frequency positions are marked.

Thanks to the Raman selectivity for symmetric modes, these bands are attributed to the C=C symmetric stretching mode in the S_2 state, around 1732 cm^{-1}, and in the S_1 state at 1756 cm^{-1}. It's worth noting that the progressive shift toward higher frequencies and the evolving line shape

are consistent with the calculated C=C frequency position in the $2A_g^-$ (S_1) and $1B_u^+$ (S_2) energy minima.[33]

We tried to repeat the same measurement in chloroform, but no excited state signal in the 1700 cm^{-1} region could be identified. In chloroform, where bands are broader, a partial distortion of the molecule in the excited state could take place upon 400 nm excitation, and thus the Raman activity of the C=C mode could decrease. Considering that Raman Gain intensities recorded in cyclohexane are on the order of 10^{-4} of magnitude, signals in chloroform are hard to be detected. Furthermore, in case of cyclohexane, it is possible that a pre-resonance condition in the high-energy excited state manifold is reached using a 800 nm Raman pump. Since in this type of carotenoids the excited energy levels depend on the polarity of the solvent, it is possible that the pre-resonance condition is not anymore satisfied in chloroform.

4 Excited State Dynamics of Peridinin*

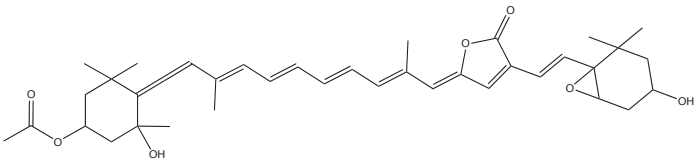

Peridinin is a C_{37} highly substituted carbonyl carotenoid which includes an allene group and a lactone ring conjugated to the polyene chain and two terminal cyclohexane rings: one on the allene side with an ester and a tertiary alcohol group, the other on the opposite side with an epoxy and a secondary alcohol group. Peridinin conjugation length can be shortly indicated as N=7OA, indicating the number of

*This chapter is based on ref.[96]

CC double bonds (7) and the presence of a carbonyl (O) and an allene (A) group conjugated to the chain. Similarly, the conjugation length on the *all*-trans-β-apo-8'-carotenal can be defined as N=8O, with 8 carbon-carbon double bonds and a terminal carbonyl group conjugated to the chain. Peridinin conjugation length is thus shorter than that of apo-8'-carotenal, although the allene group partially extends the conjugation.[12] As expected for shorter carotenoids, the relaxation dynamic in peridinin is slower than in apo-8'-carotenal: it relaxes with a 160 ps time constant in cyclohexane and 10 ps in methanol,[42] thus showing more sensitivity to solvent polarity.

In the following an Infrared and Raman band assignment for both the ground and the excited states will be presented. The characterization has been conducted in polar (chloroform), non-polar (cyclohexane) and protic (methanol) solvents. We will compare the spectroscopic behavior of peridinin with that of the all trans-β-apo-8'-carotenal in the attempt to unveil the nature of the ICT state.

4.1 Sample Handling

Peridinin samples, extracted from PCP protein, was kindly provided by Prof. Hiller in vials each containing dried pure

substance. The sample has an absorbance of 10 OD (for an optical path 1 cm) at 472 nm in ethanol (the molar extinction coefficient reported in literature[97] is ε_{472nm} = 83.6 x $10^3 M^{-1} cm^{-1}$). Samples were dissolved in HPLC purity grade solvents purchased from Sigma Aldrich and used without further purification. Sample concentrations were regulated as to obtain 0.1 OD at the maximum absorption wavelength, respectively at 460 and 472 nm in cyclohexane and in chloroform, for a 50 μm optical path. For transient IR (TRIR) measurements, ≈0.2 mM solutions were prepared, while for transient 2D-IR measurements the concentration was doubled. All samples were prepared under nitrogen atmosphere in sealed dry-box in order to minimize the presence of dissolved oxygen in solution, which rapidly causes degradation of peridinin.[98] The sample cell used for both TRIR and 2DIR measurements consists of two CaF_2 windows of 2 mm of thickness separated by a 50 μm Teflon spacer. For stimulated Raman experiments, 100 μL of sample were held in a 2 mm quartz cuvette. Due to the small amount of available sample and to its limited solubility in non-polar solvents, measurements have been carried out on representative solvents (cyclohexane, chloroform and methanol), chosen according to the classification presented in paragraph 3.1 and considering the sensitivity of the technique applied.

4.2 Ground state mode assignment

Infrared and Raman spectra of peridinin have been previously reported in literature in several solvents, but specific mode assignment is still incomplete.[95,99,100] Recently, it has been reconsidered by Bovi et al.[100] by means of ATR-IR, FT-Raman and Resonance Raman experiments with the support of DFT and QM/MM calculations. Their experiments were repeated both on solid state samples and in solution, considering the effect of solvent polarity and proticity. Measurements were repeated in different solvents as cyclohexane, acetonitrile and methanol.

Vibrational modes of peridinin are observed in three principal spectral regions. The high frequency region contains bands attributed to the allene asymmetric stretching mode, located at 1929 cm^{-1}. Bands observed around 1750 cm^{-1} were assigned to the lactone and the ester C=O stretching modes, with the ester carbonyl lower in frequency. In the 1500-1650 cm^{-1} region Bovi et al.[95] distinguished among seven specific modes of the polyene chain (prevalently C=C stretching modes coupled to in-plane deformations of the chain). Less detailed assignment was reported for the lower frequency region, where chain deformation modes are coupled to methyl and terminal ring vibrations.[99] In the following figures 4.1 and 4.2 we report the FT-IR and the Stimulated

Raman spectra registered for peridinin. The FTIR spectrum had been measured in methanol, while the Stimulated Raman measurement has been repeated both in chloroform and in cyclohexane.

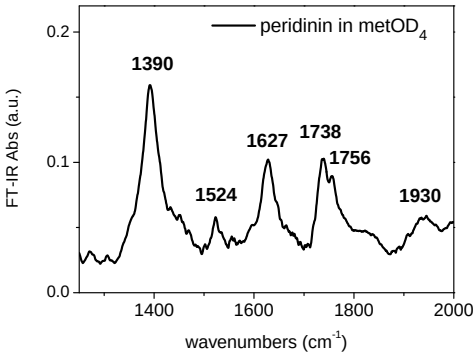

Figure 4.1: FT-IR spectrum of peridinin in full deuterated methanol.

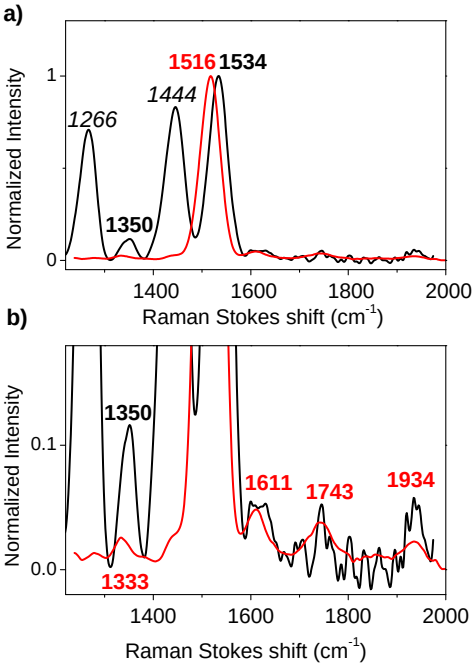

Figure 4.2: Ground state stimulated Raman spectrum of peridinin in cyclohexane (black line) and in chloroform (red line).

Due to the low solubility of peridinin in non-polar solvents, the vibrational spectrum in cyclohexane was recorded by means of the more sensitive Stimulated Raman technique

and compared to that measured in chloroform (figure 4.2). A down-shift of 18 cm^{-1} in the polar chloroform with respect to the non-polar cyclohexane is visible on the highest and narrow C=C symmetric stretching band around 1530 cm^{-1}, which agrees with solvent polarity induced shifts observed in apo-8'-carotenal (fig. 3.4). Much weaker bands are visible at the characteristic frequencies of the allene, carbonyl and asymmetric C=C stretching modes.

In the FT-IR spectrum in methanol, in the high-frequency region, a band at 1930 cm^{-1} is visible, which can be assigned to the allene transition.Furthermore, several bands in the 1500-1600 cm^{-1} can be distinguished, most probably due to chain modes. In particular, we observe a peak at 1524 cm^{-1} whose frequency corresponds to that previously assigned to the C=C symmetric stretching mode. A double band peaked at 1738 and 1756 cm^{-1} is also visible. These frequencies perfectly match the Raman frequencies reported by Bovi et al.,[95] who assigned these transitions to the H-bonded and to the non H-bonded form of the lactone carbonyl. The presence in methanol of differently solvated molecules had previously suggested to explain spectral changes in transient absorption spectra.[54] Bovi et al.[95] also excluded, on the basis of harmonic frequencies and Raman intensity calculations, the presence of the ester C=O in the Raman spectrum, since it is not conjugated to the polyene chain. The intense peak at 1738 cm^{-1} was then attributed to the single H-bonded form

of the lactone C=O, and the higher frequency peak to the non H-bonded form. Nonetheless, a double peak around 1770 cm^{-1} in cyclohexane was also found. In a recent work,Kish et al.[100] extended their analysis to more solvents. The presence of the doublet in non-polar solvents was discussed in terms of a Fermi resonance, occurring between the lactone C=O and the overtone of a lactone C-H wagging out-of-plane mode. This latter, fixed at 1777 cm^{-1}, shows to be insensitive to solvent polarity, while the carbonyl transition red-shifts with increasing polarity. In non-polar and slightly polar solvents, such as in cyclohexane, THF and diethyl-ether, the two bands forming the doublet peak structure are very close and they observed that the high frequency C-H wagging borrows intensity from the lactone C=O. In a polar environment, such as in ACN, the two bands split apart, the Fermi coupling strength decreases and a single C=O band at lower frequencies was observed. The Raman data seem to be consistent with the Fermi resonance explanation; however our 2D-IR spectra measured for peridinin in methanol (figures 4.3) and in deuterated chloroform (figure 4.4) do not show any evidence of Fermi resonances.

The identification of a Fermi resonance in a 2D-IR spectrum is generally straightforward[101,102]: the negative bleaching and stimulated emission signal (colored in blue in all the reported 2D-maps) of the enhanced overtone is expected along the diagonal, while its positive excited state absorption

peak (shown in red) should be at higher frequencies, thus on the right side of the diagonal blue peak. In our 2D spectra of peridinin in polar solvents no such evidences of Fermi resonance can be found. Unfortunately, we could not measure the 2D-IR spectrum of peridinin in non-polar solvents because of the limited solubility.

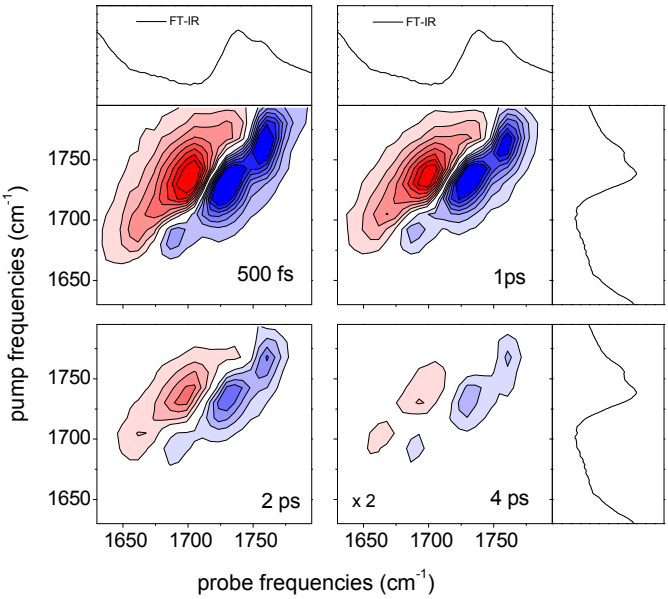

Figure 4.3: 2D-IR spectra of peridinin in methanol acquired at different pump-probe time delays. On top and on the right, the corresponding linear FT-IR spectrum. 16 contour levels have been cut between +0.3 and -0.3 signal intensity; at 4 ps the same number of contour levels has been cut between ±0.15.

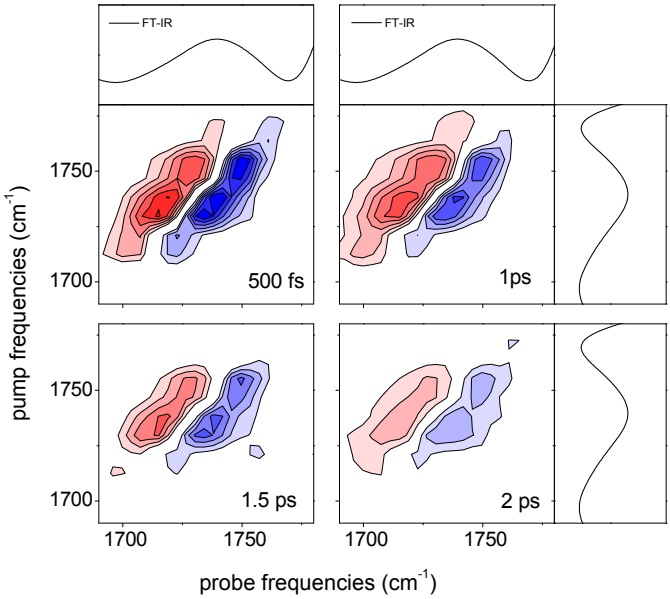

Figure 4.4: 2D-IR spectrum of peridinin in deuterated chloroform acquired at different pump-probe delays. On top and on the right, the corresponding linear FT-IR spectrum.16 contour levels have been cut between +0.26 and -0.26 signal intensity.

In the spectrum registered in methanol, shown in figure 4.3, two peaks with similar intensity are visible, respectively at 1730 and 1757 cm^{-1}. Furthermore, a third peak is observed at 1680 cm^{-1}. The two most intense peaks show a

similar behavior, with a population decay time T_1= 1.5 ps, which well correlates to the H-bonded carbonyl vibrational lifetime.[103] In methanol, each C=O group can be bound to one or even two solvent molecules, or being non H-bonded at all. The formation of an H-bond with one solvent molecule gives rise to a down-shift of about 20 cm^{-1}.[104,105] Based on the IR harmonic frequencies and intensities calculated by Bovi et al.,[95] the lactone and ester carbonyl stretching modes should have similar intensities and almost identical frequencies in polar solvents. In order to clarify the C=O assignment, we measured the 2D-IR spectrum of peridinin also in the aprotic deuterated chloroform (see figure 4.4). Because of our 4 cm^{-1} frequency resolution, we would expected to see only one broad band along the diagonal if the two C=O transitions strongly overlapped. On the contrary, as shown in figure 4.4, two peaks are visible at 1737 and 1750 cm^{-1}, which decay slightly faster than in methanol (T_1= 1.1 ps) and with a smaller frequency separation (13 cm^{-1}). Since peridinin has two carbonyl functional groups, the lactone and the ester, both IR active and no H-bond occurs in chloroform, the two components of the doublet can only correspond one to the ester C=O and one to the lactone C=O.

The two higher frequency modes observed in methanol (those at 1730 and 1757 cm^{-1}) are broader and spectrally more separated than the corresponding bands in chloroform: this may result from the existence of several overlapping

bands possibly due to different interactions with methanol. Furthermore a third less intense band is visible at 1680 cm^{-1} which could be due to H-bonded molecules. An unambiguous assignment could be obtained from ^{13}C or ^{18}O isotopic substitution, however the synthesis of labelled compounds is quite expensive. Nevertheless, a careful analysis of the time-resolved 2D-IR spectra could give additional information. By analysing the variation in time of the diagonal peak tilting it is possible to estimate the spectral diffusion time. Figure 4.5 reports the 2D-IR maps at several time delays, registered both in methanol and chloroform, showing the time evolution of the diagonal peaks tilt.

In a FT-IR spectrum, broad bands generally result from an inhomogeneous distribution of frequencies of the same mode, rising from different solute-solvent interactions or from the presence of different conformers in solution. On a 2D-IR spectrum, the same effect gives rise to an elongated peak along the diagonal. If the frequency correlation function, which depends on the dephasing time, decays within the vibrational lifetime, which depends on the population time, the diagonal peak becomes round-shaped and vertically tilted at increasing pump-probe delays. On the contrary, if the dephasing time is longer than the vibrational lifetime, the diagonal peak remains elongated at long timescale, and the system remains inhomogeneous. A narrow linear IR band generally results on the 2D spectrum vertically tilted and

round-shaped at early time delays: this can be due either to a pure natural homogeneous broadening (due to uncertainty principle) or to motional narrowing (when the frequency correlation time is smaller than the experimental time resolution).

As shown in figure 4.5, in both solvents, the peak at higher frequency is definitely much closer to the vertical direction than the other peak, already at 0.5 and 1 ps time delay. This is an indication that the corresponding molecular vibration has less inhomogeneous character. The lactone C=O is constrained by the ring and the nearby conjugated system to its position. On the other hand, the ester C=O is almost free to rotate around the single C-O bond, thus resulting in a higher number of conformations and in a larger inhomogeneous character of the vibration. Therefore, we assign the higher frequency band to the lactone carbonyl stretching mode (1757 cm^{-1} in methanol and 1750 cm^{-1} in chloroform) and that at lower frequency to the ester C=O (1730 cm^{-1} in methanol and 1737 cm^{-1} in chloroform). The peak at 1680 cm^{-1} in methanol could be due to a multiple H-bonded carbonyl. Finally, it is worth noticing that in both solvents other low intense bands are visible, such as the band at 1722 cm^{-1} in chloroform. These weak transitions can be due to overtones as well as combination bands.[106]

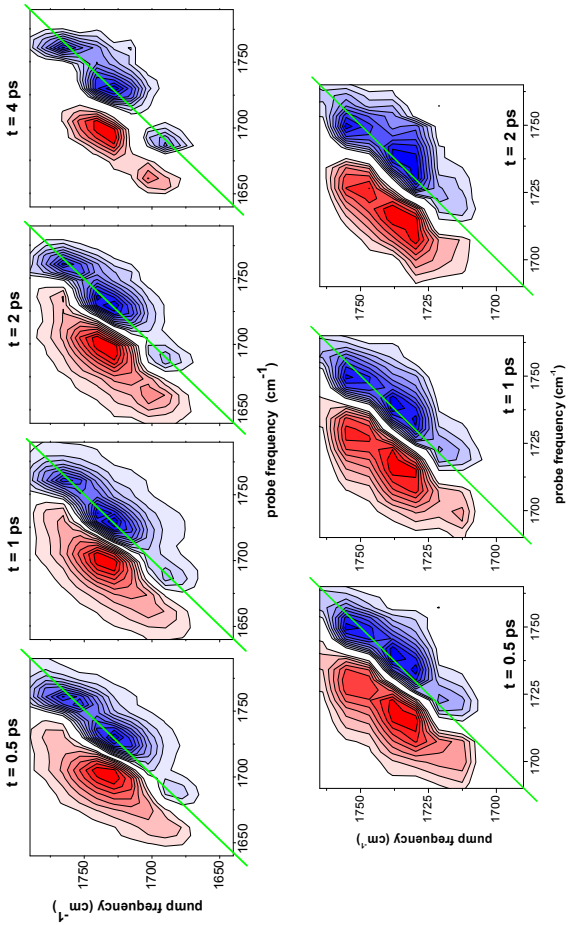

Figure 4.5: Time-resolved 2D-IR spectra in methanol (on top) and in deuterated chloroform (to the bottom): 20 contour levels have been cut between max/min of signal intensity at each delay.

4.3 Static Uv-Vis analysis

Peridinin Uv-Vis absorption spectra reported in figure 4.6 and in the literature,[39,42] as function of solvent polarity and polarizability, are similar to those of other carbonyl carotenoids (paragraph 3.2). Briefly, this group of molecules absorbs in the green-blue region of the visible spectrum and the absorption band shifts to the red with increasing solvent polarity. At the same time, as solvent polarity increases, the vibronic structure becomes unresolved and the absorption band broadens on its red tail, probably because of the presence of several slightly different conformers.

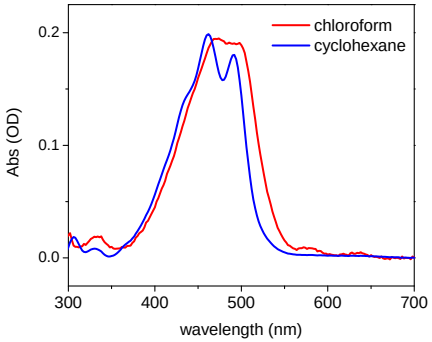

Figure 4.6: UV-Vis absorption spectra of eridinin in chloroform and cyclohexane.

4.4 Transient IR analysis

The excited state evolution of peridinin has been largely investigated in the literature. Several time resolved experiments based on the use of visible pulses, such as pump-dump-probe experiments[57,107], time-resolved fluorescence and transient absorption studies, have been carried out as function of solvent polarity[53], viscosity, excitation wavelength and temperature,[54] conjugation length,[52,108] side-groups,[56] and position of substituents along the chain.[50]

In this molecule, more than in other carbonyl carotenoids, the description of the excited states in terms of an idealized C_{2h} symmetry seems to be inappropriate, as demonstrated by its unusually high fluorescence yield (Φ_F=10^{-3} in polar solvents, higher than for the apo-8'-carotenal 10^{-5}),[39] which has been explained through a dual emission from both S_2 and S_1 states.[49] In polar solvents, charge transfer spectral features have been identified in the transient absorption signals observed above 600 nm, similarly to what observed in the *all* trans-β-apo-8'-carotenal, and in the near-IR region around 900-1000 nm,[42,53] where a negative transient signal characterized by a 1 ps rise has been assigned to the stimulated emission from the ICT state.

Less abundant are in the literature transient infrared studies on peridinin.[9,58] In this thesis, we measured transient

infrared spectra in the 1500-1800 cm^{-1} region, exciting the sample on the blue side (400 nm), close to the maximum (480 nm) and on the red side (515-530 nm) of the static absorption spectrum both in cyclohexane and chloroform (figure 4.7). we chose these solvents as representative for non-polar and polar-slightly polarizable environments, respectively. The spectra collected in both solvents at the three excitation wavelengths are reported in figure 4.7.

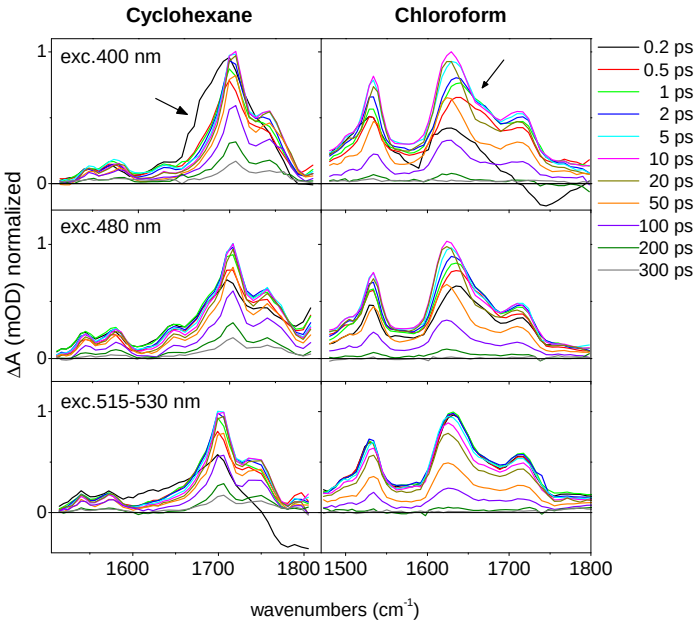

Figure 4.7: Normalized transient infrared spectra acquired at different pump-probe delays, exciting on the blue-side (400 nm), close to the top (480 nm) and on the red-side (515-530 nm) of static absorption spectrum in cyclohexane and in chloroform. Arrows indicate the opposite shifts observed on the main ESA band in the two solvents at increasing pump-probe delays.

In all the transient spectra shown in figure 4.7, negative signals due to the ground state depletion are not distinguished over the excited states absorption positive signal, if not at very early time delays for carbonyl stretching modes around 1740 cm^{-1} in chloroform (see the FT-IR broad band reported on top of figure 4.4) and around 1770 cm^{-1} in cyclohexane[95]. As already noticed in the previous chapter in case of apo-8'-carotenal, also for peridinin the excited state absorptions are remarkably more intense than ground state signals, and generate an overall positive transient signal, where ground state transitions are visible only as dips.

In cyclohexane, the most intense absorption bands are peaked at 1740 and 1703 cm^{-1}, while at lower frequencies less intense bands are observed at 1630, 1570 and 1540 cm^{-1}. In this non-polar solvent, spectral evolution is limited to a small narrowing of the band at 1703 cm^{-1} toward higher frequencies. Also, changes in the spectral shape at different excitation wavelengths are barely appreciable (fig.4.8).

In chloroform, bands are broader and about 30 cm^{-1} downshifted with respect to the corresponding bands in cyclohexane. Three intense excited state absorptions appear around 1710, 1630 and 1535 cm^{-1}. With increasing pump-probe delay and by moving the excitation wavelength to the red, the 1630 cm^{-1} band shifts to the red. In any case, independently from the excitation wavelength, it reaches the 1620

cm^{-1} value at long delays. A third band around 1670 cm^{-1} is also visible, whose intensity is higher when the excitation is at 400 nm.

Band narrowing and frequency shifts as a function of the excitation wavelength are better shown in figure 4.8.

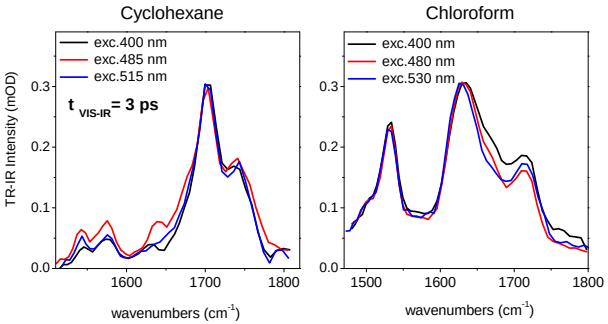

Figure 4.8: Normalized transient infrared spectra acquired at 3 ps pump-probe delay and reported as function of the excitation wavelength in cyclohexane and chloroform.

In order to analyze the relaxation dynamics in the two solvents, time-resolved spectra have been globally analyzed imposing a sequential decay scheme with increasing lifetimes. The singular value decomposition (SVD) isolated three components to satisfactorily fit data. The evolution associated

difference spectra (EADS) obtained from global analysis are reported in figure 4.9.

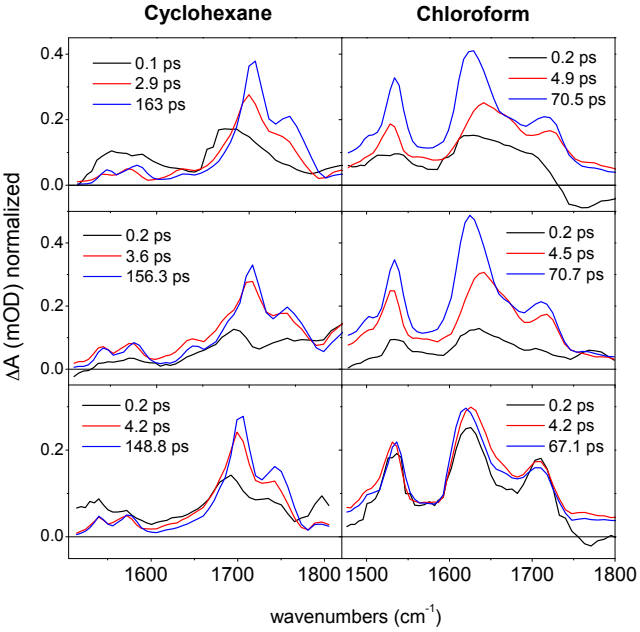

Figure 4.9: Evolution associated difference spectra of transient infrared signals reported in figure 4.7.

According to the well-known dependence on the solvent polarity, the longest lifetime extracted from the fit is remarkably shorter in chloroform and further decreases exciting at

515-530 nm. The same dependence on the excitation wavelength was observed in the apo-8'-carotenal. The first decay component, with lifetime around 100-200 fs, can be associated to the decay in the initially excited S_2 state. The second spectral component, on the 3-5 ps timescale, undergoes large spectral changes depending on the solvent.

In cyclohexane, a broad absorption peaked at 1680-1690 cm^{-1} rises right after excitation and in a sub-picosecond timescale upshifts more than 20 cm^{-1}. In the following EADS, this band narrows and increases in intensity on its blue-side, consistently with the vibrational cooling in the low-lying excited state, before the ground state recovers in 150-160 ps.

In chloroform, in the first EADS, bleaching of ground state vibrations are visible in the carbonyl region and two broad absorption bands appear at 1530 and 1620 cm^{-1}. With a 0.2 ps time constant, the system evolves to the second spectral component: at all the excitation wavelengths, the peak at 1530 cm^{-1} increases in intensity and slightly blue-shifts, while the bands at 1600-1700 cm^{-1} remarkably upshift upon 400 and 480 nm. With a 4-5 ps time constant, the band around 1630 cm^{-1} further increases in intensity, narrows and shifts back to lower frequencies. When the excitation wavelength is set at 530 nm the spectral evolution in the high frequency region is not observed.The same *red-blue-red* evolution in the 1630-1670 cm^{-1} upon 400 and 480 nm was ob-

served for the excited state C=C symmetric stretching mode of the apo-8'-carotenal in chloroform around 1670-1720 cm^{-1} . Therefore, the excited state absorption bands at 1630-1670 cm^{-1} observed in peridinin can be tentatively assigned to the same excited state C=C mode.

While the observed evolution in cyclohexane is consistent with a sequential relaxation scheme $S_2 \rightarrow S_1 \rightarrow S_0$, characteristic of non-polar carotenoids, in chloroform a new relaxation scheme has to be considered to explain observed spectral changes.

In order to better analyse the evolution of the tentatively assigned excited state C=C band, we have compared in figure 4.10 the kinetic traces respectively taken on the red-side of the main absorption band (1620 cm^{-1}) and on its blue-shoulder (1670 cm^{-1}). As it is evident, the two kinetics are different, with the low frequency trace rising slower than the high frequency one. The slower rising component on the low frequency side excludes a perfect sequential relaxation scheme and suggests the involvement of a further electronic state, the ICT state, in the relaxation dynamics. Although more emphasized by the 400 nm excitation, the slow rising component at 1620 cm^{-1} is present also when the excitation is at 530 nm. As in apo-8'-carotenal, it is worth noticing that by up-shifting and then red-shifting back in frequency, on the long time scale, the excited state C=C band recovers the fre-

quency position observed at early times, when the molecule is in the S_2 state.

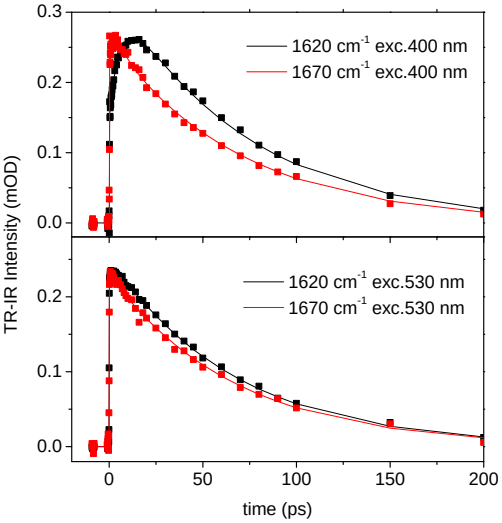

Figure 4.10: Kinetic traces taken at 1620 and 1670 cm^{-1} in chloroform upon 400 nm (on top) and 530 nm (bottom) excitation.

4.5 Excited state vibrational mode assignment

4.5.1 Transient 2D-IR spectra

In the linear transient IR spectrum recorded in chloroform, exciting at 400 nm, a broad band peaked at 1630 cm^{-1} and asymmetrically broaden on the high-frequency side has been found (fig.4.7). The band shape noticeably changes at increasing pump-probe delays, suggesting that two excited state bands with different kinetic behaviors underlie the broad envelope.

The selective IR excitation used to collect a 2D spectrum allows for the disentanglement of sub-bands, if they are enough separated in frequency. In order to resolve multiple bands possibly hidden under the broad band peaked at 1630 cm^{-1}, we have collected transient 2D-IR spectra at different Vis pump/IR probe delays and with the IR pump/IR probe delay fixed at 0.5 ps. The acquired spectra measured exciting the sample at both 400 and 530 nm, are reported in figure 4.11 and 4.12. Here we look for the presence of two diagonal peaks around 1630 and 1660 cm^{-1} and for two independently kinetic traces, not altered by the overlap.

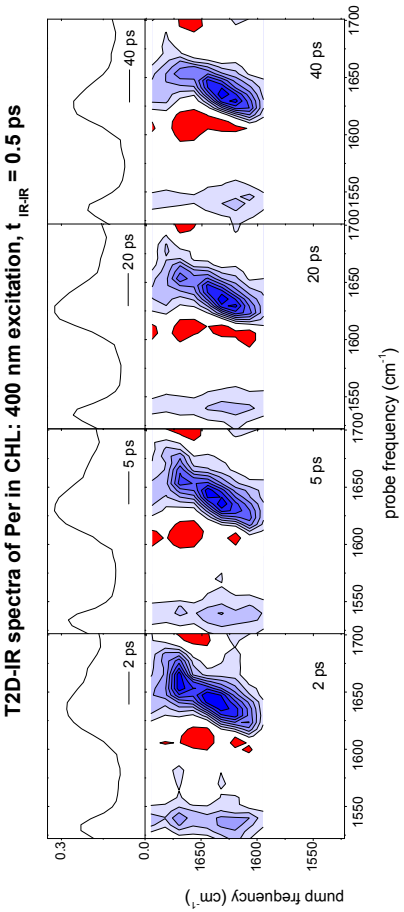
T2D-IR spectra of Per in CHL: 400 nm excitation, t IR-IR = 0.5 ps
2 ps
5 ps
20 ps
40 ps
0.3
0.0
1650
1600
1550
1700
1650
1600
1550
probe frequency (cm-1)
pump frequency (cm-1)

Figure 4.11

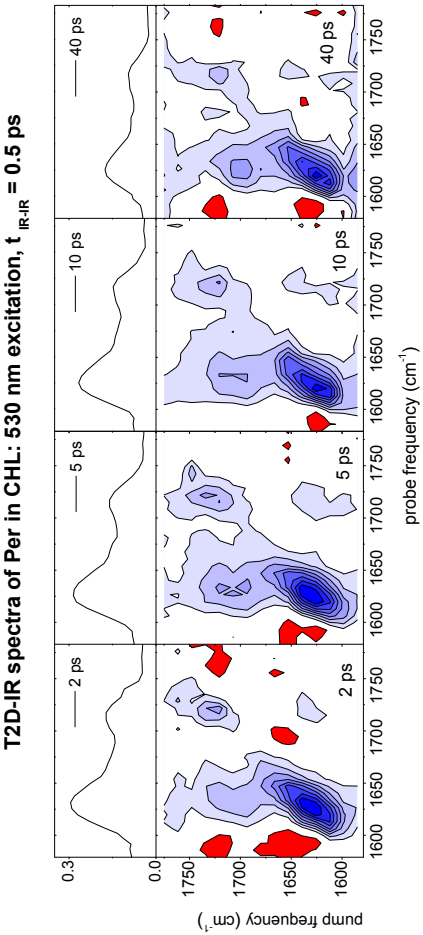
T2D-IR spectra of Per in CHL: 530 nm excitation, t IR-IR = 0.5 ps
2 ps
5 ps
10 ps
40 ps
0.3
0.0
1750
1700
1650
1600
pump frequency (cm-1)
probe frequency (cm-1)

Figure 4.12

Since T2D-IR spectra rise from a double difference of the row spectra, intensity of transient bands is very low (≈0.15 mOD for the bleaching band). In order to acquire 2D spectra of a good quality, the signal to noise ratio has to be optimized and the baseline stable. In the condition of our experiments we obtained a noise level of ±0.006 mOD. In figure 4.11 and 4.12 we report on top of each 2D spectrum the corresponding linear TR-IR spectrum measured at the same Vis-pump/IR-probe delay.

As it can be clearly noticed by inspecting figure 4.11, when the sample is excited at 400 nm, two diagonal peaks at 1630 and 1660 cm^{-1} along the diagonal are clearly identified. Furthermore, the excited state cross peaks with the 1530 cm^{-1} transition are well visible. When the visible excitation is moved to 530 nm, only a broad diagonal peak is visible at 1630 cm^{-1}, besides another band at 1710 cm^{-1} (notice that the IR probe has been set to a different frequency window). These findings are in line with the band narrowing observed in the TRIR spectrum registered upon 530 nm excitation: in this case however there is no evidence of a separate band peaking at 1660-1650 cm^{-1}. As already seen from the TRIR results, the intensity of the blue-shoulder on the 1630 cm^{-1} band decreases moving excitation to the red, thus resulting in a broadening of the intense ESA band on its blue-side. This asymmetric broadening is also visible on the 2D spectrum, especially on the long timescale, where a progressive

narrowing of the band toward the low frequency side can be appreciated.

In figure 4.13 we compare the kinetic traces registered at 1620/1630 and 1660 cm^{-1} in the linear transient infrared spectra with those recorded in the transient 2D measurement. In this region, as shown by the T2D spectrum excited at 400 nm, two bands largely overlap so that independent dynamics of the two components can be measured only making use of selective IR excitation, i.e. from 2D spectra.

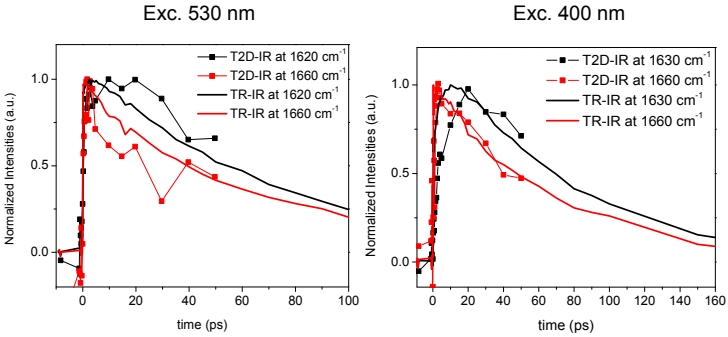

Figure 4.13: Transient IR and 2D-transient IR kinetic traces taken at 1620-1630 cm^{-1} and at 1660 cm^{-1}. Exciting with a selective IR pump, the low-frequency band shows a rising component even slower than what previously observed (fig.4.10).

The kinetic comparison shows that the rise component of the peak at 1630 cm^{-1} is even slower when measured with the selective IR pump than what previously reported (see figure 4.9). From the global analysis on linear transient IR spectra a time constant of 4-5 ps was found for the rise component of the 1630 cm^{-1} band. Here, the maximum of the intensity at the same wavelength is reached 20-30 ps after Vis excitation, instead of 10 ps. We can conclude that the rising time constant is twice longer than the one determined from 1D spectra.

4.5.2 Transient Stimulated Raman

To gain more insights on the assignment of vibrational bands in the excited state, transient IR data have been integrated with their Raman counterpart. The mode with the highest Raman activity is the symmetric C=C stretching, located around 1530 cm^{-1} in the ground state and expected to upshift more than 100 cm^{-1} in asymmetric carotenoids in the excited state.[61]

The transient Raman spectrum reported on top of figure 4.14) has been collected in cyclohexane, after 10 ps from the actinic excitation centered at 400 nm and using a Raman pump at 800 nm. The corresponding ground state stimulated Raman spectrum is reported to the bottom of the same figure.

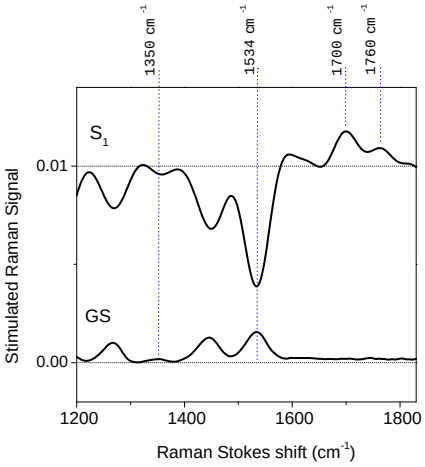

Figure 4.14: Ground state stimulated Raman spectrum of peridinin in cyclohexane (black line, GS) and transient stimulated Raman Gain signal (red line, S_1) recorded at 10 ps from the 400 nm excitation.

The transient Raman spectrum shown in figure 4.14 is relative to the S_1 state. Negative signals rise from both the depletion of the peridinin ground state (at 1530 and 1350 cm^{-1}) and the loss in the molecular concentration due to a local heating laser effect. Because of the local expansion of the liquid, two solvent bands are also visible at 1444 and 1266 cm^{-1}. Above 1600 cm^{-1}, ground state modes do not have

appreciable Raman activity; however, on the S_1 Raman spectrum two excited state bands are clearly observed at 1700 and 1760 cm^{-1}. Their frequencies and spectral shapes are close to those observed in the transient IR spectrum in cyclohexane (fig.4.7): we tentatively assign the most intense band at 1700 cm^{-1} to the excited state C=C symmetric stretching mode and the band around 1760 cm^{-1} to the lactone C=O mode. The latter can possibly acquire some Raman activity in the excited state through the conjugation to the polyene chain.

The carbonyl mode is expected to down-shift in the excited state, as observed in labeling experiments on apo-8'-carotenal (fig. 3.13) and reported in the literature.[9] In case of peridinin, we notice a 20 cm^{-1} downshift in cyclohexane (from 1780 cm^{-1} to 1760 cm^{-1}, as observed in TR-IR and FSRS experiments). In case of apo-8'-carotenal, our labeling experiments show that the carbonyl frequency downshifts by 60 cm^{-1}. The up-shift of the excited state C=C symmetric stretching mode further confirms the analogy observed between apo-8'-carotenal and peridinin. However, while in cyclohexane this mode up-shifts in apo-8'-carotenal from 1530 to 1750 cm^{-1} (+220 cm^{-1}), in peridinin it goes from 1534 to 1704 cm^{-1} (+170 cm^{-1}). In the same way other vibrational modes undergo larger shifts for apo-8'-carotenal than for peridinin upon visible excitation. This difference is due to the lower degree of symmetry of the structure of peridinin

if compared with other carbonyl carotenoids.

Described in detail by Noguchi et al.,[61] here we briefly explain why a lower symmetry causes smaller shifts of excited state bands with respect to the corresponding ground state position. Departing from the diabatic frequency Ω of a given vibrational mode, its adiabatic frequency ω_i on the i-th electronic state can be expressed as:

$$\omega_i = \Omega[1 + \sum_{i \neq j} 2V_{ij}^2 (E_i - E_j)^{-1} \Omega^{-1}]^{1/2} \tag{4.1}$$

The mode frequency position in S_0 and S_1 states corrected for all the possible vibronic couplings among the three lowest singlet states $S_0(1A_g^-)$, $S_1(2A_g^-)$ and $S_2(1B_u^+)$ is:

$$\omega_{S0} = \Omega[1 - 2V_{01}^2 (E_1)^{-1} \Omega^{-1} - 2V_{02}^2 (E_2)^{-1} \Omega^{-1}]^{1/2} \tag{4.2}$$

$$\omega_{S1} = \Omega[1 + 2V_{01}^2 (E_1)^{-1} \Omega^{-1} - 2V_{12}^2 (E_2 - E_1)^{-1} \Omega^{-1}]^{1/2} \tag{4.3}$$

In an idealized C_{2h} symmetry, modes in the $S_2(1B_u^+)$ state do not couple with modes in the S_0 and S_1 A_g^- states, thus V_{02} and V_{12} are equal to zero and ω_{S0} and ω_{S1} only depend on the V_{01} coupling. In case of carotenoids, the effect of the S_0-S_1 coupling is to further split apart ground and excited state transitions.

When the C_{2h} symmetry is broken, also the V_{12} coupling term becomes appreciable, while the $V_{02}E_2^{-1}$ contribute is small due to the large state energy difference. The effect of the V_{12} coupling on the frequency position in the S_1 state is to reduce the shift induced by the V_{01} coupling. Thus, while the ground state frequency position remains unchanged, S_1 excited state modes move closer to corresponding ground state modes, decreasing the molecular degree of symmetry.

In the case of carotenoids, the S_0-S_1 coupling is strong and the $S_1 \rightarrow S_0$ internal conversion proceeds primarily through the a_g^- C=C symmetric stretching mode. Since V_{01} is positive, the C=C mode largely upshifts in the S_1 excited state, as it has been observed by Time-Resolved Resonant and Stimulated Raman experiments on β-carotene and on other carotenoids.[61,62,75]. In less symmetric carotenoids, such as peridinin, the S_2-S_1 coupling increases and reduces the shift induced by the S_0-S_1 coupling. It is worth noticing that the S_2-S_1 coupling is strongly solvent dependent, because sensitive to the E_2-E_1 energy gap. At increasing solvent polarity, in fact, the S_2 excited state is more stabilized than the S_1 state, thus resulting in a further redshifted excited state C=C mode in chloroform with respect to the same transition in cyclohexane.

5 Discussion of experimental results

The experimental results presented in the previous chapters evidenced that the dynamical behaviour of peridinin and *all* trans-β-apo-8'carotenal presents several common aspects. The analysis of transient spectra, both in the visible and infrared regions allowed for identifying similar marker bands, which, for both molecules, can be ascribed to an intramolecular charge transfer (ICT) state. We have investigated the solvent dependence of the bandshape and their dynamic evolution and we concluded that both solvent polarity and polarizability has to be considered.

In this chapter we will present a relaxation model that allows to reasonably interpret all the visible, infrared and Raman data reported in this PhD work and to explain several observation previously made in the literature.

From the IR data presented in paragraph 3.4 and 4.4, we

have seen that the band which could give more information about the presence of an ICT state in polar media is the excited state C=C absorption. This band has been assigned to a broad feature peaking around 1700 cm^{-1} in the apo-8'-carotenal and to a similarly broad envelope peaking at 1630 cm^{-1} in peridinin. The analysis of transient 2D-IR spectra revealed that in both systems two peaks underlie this broad absorption, whose dynamic evolution is clearly different. Based on the solvent analysis and on the excitation wavelength dependence of the excited state C=C absorption band, we attribute the lowest frequency peak, at ≈1680 cm^{-1} in the apo-8'-carotenal and at ≈1630 cm^{-1} in peridinin, to the ICT excited state and the highest frequency peak, located at ≈1710 cm^{-1} in the apo-8'-carotenal and at ≈1660 cm^{-1} in peridinin, to the S_1 state.

It remains to clarify the electronic nature of the ICT state. We have seen that the ICT marker bands in polar and polarizable solvents generally recover at longer timescales the initial position right after excitation, that to say in the S_2 state. Being the $S_2(1B_u^+)$ itself a ionic state, we suggest that this state gives the major contribution to the later appearance of the ICT state. It is necessary at this point to illustrate a molecular mechanism by which this ionic $1B_u^+$ state can be repopulated on a time scale of a few picoseconds, since it is well known from many previous studies on carotenoids that the initially populated $S_2(1B_u^+)$ rapidly relaxes on a sub-ps

timescale into the low lying $S_1(2A_g^-)$ state. In the following, we will discuss in details the dynamic evolution of carbonyl carotenoids in a non-polar and in a polar medium, basing observations on our transient spectroscopic data.

The analysis of the visible and infrared spectra of apo-8'-carotenal and peridinin **in non polar solvents**, such as cyclohexane, revealed no striking differences from neutral carotenoids. In this case, the bright $1B_u^+$ state relaxes in the $2A_g^-$ state in a sub-picosecond timescale. The following dynamics, taking place in a 2-3 ps timescale,can be safely interpret in terms of vibrational relaxation on the S_1 potential energy surface, since all transient data show no evidences for the involvement of an additional electronic state in the relaxation process. Finally, the ground state recovers in about 25 ps in the apo-8'-carotenal and in 160 ps in peridinin. All considered processes are non-radiative internal conversions.

From previous studies,[12] it is known that the increase in the conjugation length corresponds to a decrease in the lifetime, according to the energy gap law. The conjugation length in peridinin is smaller than in the apo-8'-carotenal, thus longer relaxation timescales experimentally found in our and previous studies perfectly agree with the expected trend.

The effect of the excitation wavelength in non-polar solvents deserves a few comments. As already noticed in tran-

sient visible spectra of the apo-8'-carotenal (paragraph 3.3), bands around 600-700 nm slightly increase in intensity when exciting the molecule at 515 nm. Moreover, in the infrared (paragraph 3.4), a small broadening on the low frequency side of the C=C excited state symmetric stretching mode is observed upon red excitation for both molecules. These observations suggest the presence of a small excited population with charge transfer character even in non-polar solvents, depending on the excitation wavelength.

When considering **highly polar solvents**, with the relative dielectric constant ε_r>15 (see Chap.3), our measurements and previous data[49,109] show that the polar B_u^+ state is stabilized over both covalent A_g^- states. In asymmetric carotenoids, like the investigated molecules, symmetry rules are not strictly applicable and ionic and covalent states mix in defining excited state wave functions. With increasing solvent polarity, the weight of the B_u^+ component in the lower excited state likely increases, thus explaining the fast recovering time observed in DMSO, acetonitrile and in methanol in both molecules ($\approx$ 8-10 ps) and the increased S_1 fluorescence yield.[49] The B_u^+ contribution would also result in an increased transition dipole moment between the ground and the lower excited state, as observed by recent calculations on peridinin.[110] Nonetheless, some molecular structural rearrangements must be involved, because no absorptions at lower frequency are observed on the steady-state spectrum

in the FC region. A completely planar molecular configuration is expected not to be stabilized in polar solvents, since the latter would preferentially solvate the carbonyl and other polar functional groups linked to the polyene inducing molecular distortions. It is thus expected that, right after excitation, the system moves away from the FC region on a fast sub-picosecond timescale. Confirming this expectation, ICT marker bands occur on transient visible and IR spectra in polar solvents at very short pump-probe time delays. In some cases (see for instance in methanol and ACN) the intensity of the ICT bands is even higher than that of the S_1 a_g^- bands, thus showing a predominant ionic b_u^+ character along with all the overall relaxation.

In solvents with **intermediate polarity**, the effect of polarizability becomes relevant. ICT marker bands, which are already present after the first 200 fs, change in their spectral shape and shift on 3-5 ps timescale for the apo-8' carotenal and on 5-10 ps timescale for peridinin. Also in this case, distorted molecules are stabilized by solvent rearrangement, however, in less polar solvents than DMSO and ACN, dynamics which involve a conformational change are slower. In slightly polarizable solvents, like in diethyl-ether, neither polarity nor polarizability of the solvent are able to stabilize distorted molecules so that a planar configuration results more stabilized.

Based on all these observations we could now elaborate a relaxation scheme allowing for taking into account the increase of the ionic character, thus the appearance of the charge transfer features in the low lying excited state in polar/polarizable solvents for the analysed carbonyl carotenoids. The suggested kinetic scheme is sketched in figure 5.1, where the relaxation pathways in both non-polar and polar media are described.

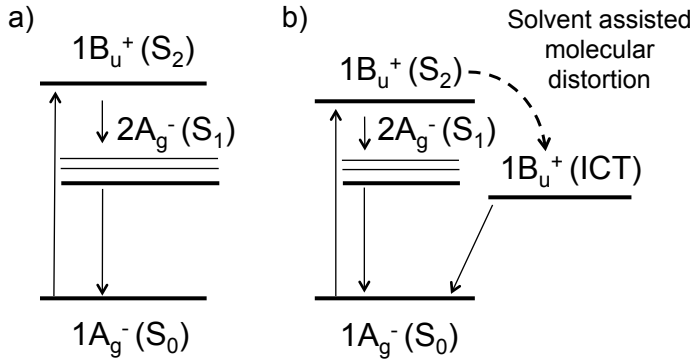

Figure 5.1: Proposed relaxation scheme in a non-polar (a) and in a polar/polarizable solvent (b).

As it is shown in figure 5.1 A, in non-polar solvents the electronic relaxation proceeds as for symmetric polyenes according to the C_{2h} description of excited state electronic manifold. A first order kinetic sequential scheme $S_2 \rightarrow S_1 \rightarrow S_0$ is

followed, so that EADS extrapolated from the global analysis ruled on transient visible and infrared data in non-polar solvents (figures 3.7 and 3.10 A for the apo-8'-carotenal and figure 4.9 for peridinin) can be considered as representative for the molecular system at the corresponding time constants.

In figure 5.1 B, all possible relaxation pathways favorite by polar/polarizable solvent rearrangements are sketched. While in highly polar solvents the S_2 and S_1 excited states are so close in energy that a strong mixing between the two states can be considered, in solvents with intermediate polarity, the relaxation pathway which predominates strongly depends on solvent polarizability. In polar and polarizable solvents, excited distorted conformers are stabilized through dispersive interactions with surrounding solvent molecules, while in less polarizable solvents, no dispersive interactions occur with the surrounding, so that the most stable planar conformation is the one which is favorited.

Based on previous reported experimental observations, we suggest that the major contribution to the ICT state is given by the ionic B_u^+ state. This state, initially populated by effect of light absorption, partially relaxes on a few ps timescale into the low lying S_1 ($2A_g^-$) state. However, since molecules rapidly move away from the FC region, the B_u^+ state can be repopulated on a few ps timescale through a mechanism involving molecular distortions. Resulting distorted molecules

are thus dynamically stabilized by the polar/polarizable solvent rearrangement, determining a definite increase of the ionic character into the low lying excited state.

In order to test our mechanistic hypothesis several quantum chemical calculations have been made in collaboration with the INSTM group of Pisa. In the following paragraph we will present the results of this theoretical analysis and we will give a brief overview of other theoretical analysis previously presented in the literature regarding carotenoids and linear polyenes.

5.1 Computational results

The first calculations on polyenes were reported in early '70s.[27,61,111–114] In the following years, several refinements have been added.[33,51,110,115,116] Many experimental findings justify why it is still so challenging to computationally describe the photo-dynamics of carotenoids. Difficulties rise from double excited electron configurations, necessary to properly describe low-lying excited states, and from the necessity to take into account solvent effects. In particular, the effect of the solvent polarization has been investigated only for shorter polyenes, like for retinal in the vision mechanism,[43] but its role has not been fully understood yet in longer polyenes.

In order to rationalize the experimental data on apo-8'-carotenal, our collaborators carried on a series of TD-DFT and MS-CASPT2//CASSCF calculations on both *all* trans-apo 8' and 12'-carotenals, in vacuum and in solution by applying the PCM model. First, the ground state molecular geometry was optimized at both DFT and CAS level of theory. Once defined the π-active space (12,12), they calculated 12 MOs and the vertical energies of all possible states. As also reported by Wagner et al.,[51] who ruled similar calculations on a peridinin model compound, at the FC geometry the bright $1B_u^+$ state is lower in energy than the $2A_g^-$ state and no other dark states are in between. Nevertheless, the vibrational relaxation on all the internal coordinates within each excited state leads to inverted 0-0 energy transitions, thus with the state ordering as the one reported in figure 5.1 A. Through CASSCF calculations, single and double excited configuration state functions (CSF) were calculated. It was found that the $S_0 \rightarrow S_1$ transition is mainly described by the double excited |HOMO,HOMO>→|LUMO, LUMO> transition and the $S_0 \rightarrow S_2$ transition by the |HOMO> →|LUMO+1> and the |HOMO-1>→|LUMO> transitions. Looking at the MOs pictures reported in Supporting Information of ref.[33], the HOMO-LUMO transition consists of a bond order reversal along the polyene chain and of an overall stretch of the molecule. According to this result, the excited state C=O and C=C modes should downshift due to the bond

elongation, however, considering also electronic correlation and multi-state interactions, while the C=O mode still down-shifts, the C=C a_g mode up-shifts due to the strong S_0-S_1 vibronic coupling. The description of excited state wavefunctions through CSFs leads to two quasi-degenerate low-lying adiabatic states for the apo-8'-carotenal, both characterized by an almost equivalent ionic and covalent character. These calculations agree with the idea that A_g^-/B_u^+ characters can strongly mix.

Once optimized the geometry on relaxed electronic excited states, it has been investigated how the energies of these states change as a function of a molecular distortion. In this way, potential energy surfaces of adiabatic states can be traced point by point following a single internal coordinate. In figure 5.2, the internal coordinate under investigation is a rigid torsion around the C_{13}-C_{14} bond on the apo-12'-carotenal. A_g^- and B_u^+ diabatic contributions to the adiabatic state can be evaluated looking at the evolution of their weights in the CSF composition of the excited state wavefunction.

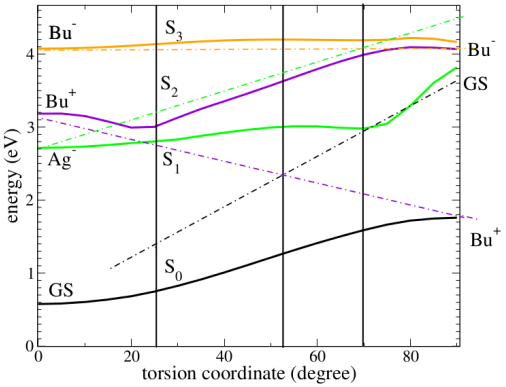

Figure 5.2: From Ref.[33]: torsion reaction path from the $2A_g^-$ minimum at the CASSCF/MS-CASPT2 level for app-12'-carotenal. Continuous lines represent adiabatic GS, S_1, S_2 and S_3 states, dashed line approximate the diabatic $1A_g^-$(black), $2A_g^-$(green), $1B_u^+$(violet) and $1B_u^-$(orange) contributions.

In figure 5.2 it can be seen that at increasing torsional angle the diabatic B_u^+ state is strongly stabilized and becomes predominant in the S_1 adiabatic state definition when the torsion angle is about 20°. The B_u^+ component even increases in the ground state, while all the A_g^- diabatic states are destabilized. Small rotations of 20° along the polyene chain are randomly possible in solution, especially in polar and polarizable solvents. Upon visible excitation on a prevalently ionic B_u^+ state, a small molecular distortion further stabi-

lizes the charge separation character. In polar and polarizable solvents, the excited distorted molecules are stabilized by dipole-dipole interactions and by the solvent rearrangement so that they directly relax to the ground state.

Likely, also at the ground state molecules can be in a distribution of distorted geometries. The presence of many slightly distorted molecules at the ground state explains why, upon 515-530 nm excitation, the ICT marker bands are more pronounced and relaxation dynamics are faster. The broadening of the steady-state visible absorption spectrum on the red-tail is generally attributed to the presence of many conformers in polar solvents. Moving excitation to the red, a distribution of distorted molecules will be directly promoted to the B_u^+ state.

5.2 Calculated excited state properties

Here we report about some calculated excited state properties both in the vacuum and in solvated systems, which allow for further justify the proposed relaxation scheme. The excited state dipole moments, the oscillator strength, the composition of excited state wavefunctions in terms of single and double excited configurations and, finally, the S_2-S_1 energy

gap have been calculated as function of the torsional angle in the apo-8'-carotenal[33] and of the BLA coordinate in peridinin.[110]

Also for peridinin, the theoretical work presented by Knecht et al.[110] shows no evidences of intermediate states between $2A_g^-$ and $1B_u^+$. The authors carried on ab initio multi-reference interaction configuration (DFT-MRCI) calculations both in vacuum and in the polar solvent acetonitrile. A similar HOMO-LUMO single and double excited configuration composition is reported for the two low-lying excited states, which result to be strongly connected by the bond length alternation (BLA) coordinate. The latter is a structural parameter which allows for a quantification of the bond order reversal. Used to describe push-pull and polyene compounds, it allows for the description of the limit resonant forms of the molecule and goes from a perfect delocalized π-conjugated system to a system with localized partial charges on single and double bonds. The BLA is defined as the difference between the average length of the carbon-carbon single and double bonds and assumes a zero value when the charge is homogeneously delocalized and positive values in presence of localized partial charges.

From Knecht's calculations, the excited-state wavefunctions result strongly dependent on structural parameters, thus supporting the idea that small variations from the FC

geometry lead to a mixing of ionic and covalent characters. At increasing BLA, the adiabatic S_1 and S_2 states come closer in energy due to the increasing similarity in the single and double excited configuration composition. Also, the S_1 oscillator strength, which is a measure of the brightness of the state, and the S_1 dipole moment, which relates to the state sensitivity to the environmental polarity, increase at increasing BLA. Increasing BLA values correspond to a decrease in the degree of the conjugation extension, which can be likely achieved through small torsions along the chain.

Same excited state properties have been calculated by Di Donato et al.[33] for the all trans-β-apo-12'-carotenal at the CASSCF//MSCASPT2 level of theory (see figure 5.3). It has been found that the ground state is mostly insensitive to small structural distortion and to solvent polarity: its dipole moment remains almost constant over a large range of torsional angle values and it slightly increases passing from cyclohexane (6.97 D) to methanol (7.78 D). Similar values are reported for peridinin in acetonitrile (5.5-8.8 D). On the contrary, excited states dipole moments strongly change increasing the torsional angle, with the adiabatic S_1 state which becomes polar while the covalent component in S_2 increases. Correspondingly, also oscillator strengths change with the S_1 state which becomes less dark and the S_2 state less bright. All these computational results strongly support the relaxation scheme presented in figure 5.1.

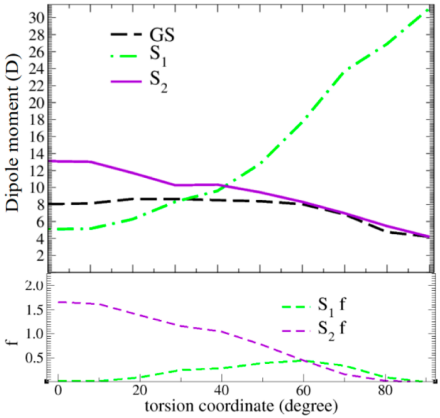

Figure 5.3: From Ref.[33]: electric dipole moments and oscillator strengths of adiabatic ground, S_1 and S_2 states as function of the torsional coordinate.

Conclusions

In this thesis we have presented a series of experimental results based on the measurement of transient spectra both in the visible and infrared spectral ranges and of 2D-IR spectra both in the ground and excited states for the *all* trans-β-apo-8'-carotenal and peridinin.

We analysed the dynamical evolution of these molecular systems and its dependence on solvents and excitation wavelenght. By analysing data, we correlated the electronic dynamics observed in transient infrared spectra with that observed in the visible region and assigned the ICT marker bands in both spectral regions. Different spectral behaviours have been described as a function of solvent polarity and polarizability. By considering all experimental data, we suggested a relaxation scheme which explains all the observed effects and elucidates the nature of the ICT state. We concluded that the major contributor to the ICT state is the ionic B_u^+ state, which in polar solvents, is repopulated through a

relaxation mechanism which involves a structural distortion of the molecule favoured by solvent rearrangements.

We furthermore clarified the role of solvent polarizability, which dynamically stabilizes the B_u^+ ionic component over the covalent A_g^-. The dynamical stabilization of the B_u^+ component, on a 2-3 ps timescale in the apo-8'-carotenal and in 4-6 ps in Peridinin (or even longer as seen by T2D measurements), leads to the ICT formation. The efficiency of this relaxation pathway, and thus of the ET to Chl a in the PCP protein, strongly depends on both environmental polarity and polarizability. Polarizability generally relates to the molecular anisotropy. The observation that this solvent property has an effect on the photo-dynamics further confirms the involvement of a molecular distorsion occurring to stabilize charge separation.

As concerns the excitation wavelength dependence observed on transient IR and visible spectra, in both molecules, the increasing ICT component upon red excitation might be explained considering the conformational disorder at the ground state. As already discussed, the broadening on the red-tail of absorption spectra is generally related to a larger conformational distribution at the ground state. This effect is observed in polar solvents, where the dielectric stabilizes slightly distorted molecules. Rotational conformers have a ground state zero point energy higher than the corresponding planar form

(fig.5.2), thus they selectively absorbs toward the charge-separated state exciting at higher wavelengths, also explaining the reported faster dynamics.

All the observations concerning the solvent effects can help in rationalizing the efficiency of peridinin-chlorophyll energy transfer in PCP. It is worth noticing, in fact, that at the PCP protein binding sites, the presence of inequivalent Peridinin molecules has been already suggested from static absorption spectra recorded on frozen solutions, confirming the presence of slightly distorted molecules or different polar/polarizable amino acidic surroundings.[9,117,118]

As a future perspective, the analysis of a single PCP domain should give us more information about short and long range interactions which occur among close packaged peridinins. From a spectroscopic point of view, a domain deprived of the chlorophyll molecules would surely help both in the IR band assignment and in the time-resolved analysis, because of the suppression of the competitive ET pathway. As concerns the photovoltaic applicability, thanks to the large tunability of the ICT state in carbonyl carotenoids, new matrixes with specific polar and polarizable properties could be engendered in order to enhance the ET and simultaneously avoid the carotenoid photo-degradation.

Appendix

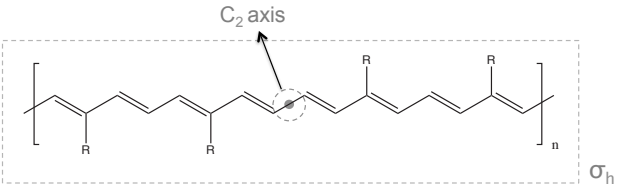

Figure 5.4: C_{2h} symmetry of the polyene associated to conjugated chain of carotenoids.

C_{2h}	E	C_2	i	σ_h	Translations and Rotations
A_g	1	1	1	1	R_z
B_g	1	-1	1	-1	R_x, R_y
A_u	1	1	-1	-1	z
B_u	1	-1	-1	1	x, y

Table 5.1: C_{2h} point group symmetry character table for translations and rotations.

The C_{2h} point group contains the following symmetry operations: the identity E, the 180° rotation (C_2) around the principle molecular axis, the centre of inversion i and the reflection across the horizontal plane that contains nuclei (σ_h). Characters ± 1 indicates if the sign of the molecular wavefunction changes upon the symmetrical operation. A and B are the Mulliken labels for the irreducible representations of the group, with A the symmetric and B the antisymmetric character to the proper rotation around the C_2 axis. The subscripts g / u, which stand for the german gerade (even) and ungerade (odd), can be defined only in symmetric molecules and represent the parity with respect to the centre of inversion The superscripts +/- represent the parity with respect to the reflection across the plane.

Bibliography

[1] Masson, G.; Orlandi, S.; Rekinger, M. *Global Market Outlook for Photovoltaics 2014-2018;* European Photovoltaic Industry Association EPIA, 2014.

[2] Lewis, N. S.; Crabtree, G. Basic Research Needs for Solar Energy Utilization Technical report, U.S. Department of Energy, **2005**.

[3] Pillai, S.; Ravensbergen, J.; Antoniuk-Pablant, A.; Sherman, B. D.; van Grondelle, R.; Frese, R. N.; Moore, T. A.; Gust, D.; Moore, L.; Kennis, J. T. M. *Physical Chemistry Chemical Physics* **2013**, *15*, 4775–4784.

[4] Maiuri, M.; Snellenburg, J. J.; van Stokkum, I. H. M.; Pillai, S.; Wongcarter, K.; Gust, D.; Moore, T. A.; Moore, A. L.; van Grondelle, R.; Cerullo, G.; Polli, D. *The Journal of Physical Chemistry B* **2013**, *117*(46), 14183–14190.

[5] O'Reagan, B.; Grätzel, M. *Nature* **1991**, *353*, 737–740.

[6] Hofmann, E.; Wrench, P. M.; Sharples, F. P.; Hiller, R. G.; Welte, W.; Diederichs, K. *Science* **1996**, *272*(5269), 1788–1791.

[7] Polivka, T.; van Stokkum, I. H. M.; Zigmantas, D.; van Grondelle, R.; Sundström, V.; Hiller, R. G. *Biochemistry* **2006**, *45*, 8516–8526.

[8] Bautista, J. A.; Hiller, R. G.; Sharples, F. P.; Gosztola, D.; Wasielewski, M.; Frank, H. A. *The Journal of Physical Chemistry A* **1999**, *103*, 2267–2273.

[9] Bonetti, C.; Alexandre, M. T. A.; van Stokkum, I. H. M.; Hiller, R. G.; Groot, L.; van Grondelle, R.; Kennis, J. T. M. *Physical Chemistry Chemical Physics* **2010**, *12*, 9256–9266.

[10] Scholes, G. D.; Fleming, G. R.; Olaya-Castro, A.; van Grondelle, R. *Nature Chemistry* **2011**, *3*(10), 763–774.

[11] Berg, J. M.; Tymoczko, J. L.; Stryer, L. *Biochemistry;* W. H. Freeman: New York, 6th ed., 2002.

[12] Polívka, T.; Sundström, V. *Chemical Reviews* **2004**, *104*(4), 2021–2071.

[13] Ziolek, M.; Pawlowicz, N.; Naskrecki, R.; Dobek, A. *The Journal of Physical Chemistry B* **2005**, *109*(38), 18171–18176.

[14] Scheuring, S.; Sturgis, J. N. *Science (New York, N.Y.)* **2005**, *309*(5733), 484–7.

[15] Demmig-Adams, B.; Adams, W. W. *Nature* **2000**, *403*(6768), 371–374.

[16] Edge, R.; McGarvey, D. J.; Truscott, T. G. *Journal of Photochemistry and Photobiology B: Biology* **1997**, *41*(3), 189–200.

[17] Frank, H. A.; Cogdell, R. J. *Photochemistry and Photobiology* **1996**, *63*(3), 257–264.

[18] Ruban, A.; Horton, P. *Plant physiology* **1999**, *119*(2), 531–42.

[19] Di Valentin, M.; Salvadori, E.; Agostini, G.; Biasibetti, F.; Ceola, S.; Hiller, R.; Giacometti, G. M.; Carbonera, D. *Biochimica et Biophysica Acta* **2010**, *1797*(10), 1759–1767.

[20] Lunch, C. K.; Lafountain, A. M.; Thomas, S.; Frank, H. A.; Lewis, L. A.; Cardon, Z. G. *Photosynthesis Research* **2013**, *115*, 139–151.

[21] van Amerongen, H.; van Grondelle, R. *The Journal of Physical Chemistry B* **2000**, *105*(3), 604–617.

[22] Collini, E. *Chemical Society Reviews* **2013**, *42*(12), 4932–4947.

[23] Ostroumov, E. E.; Mulvaney, R. M.; Cogdell, R. J.; Scholes, G. D. *Science* **2013**, *340*(6128), 52–56.

[24] Romero, E.; Augulis, R.; Novoderezhkin, V. I.; Ferretti, M.; Thieme, J.; Zigmantas, D.; van Grondelle, R. *Nature Physics* **2014**, *10*, 676–682.

[25] Ferretti, M.; Novoderezhkin, V. I.; Romero, E.; Augulis, R.; Pandit, A.; Zigmantas, D.; van Grondelle, R. *Physical Chemistry Chemical Physics* **2014**, *16*(21), 9930–9939.

[26] Hudson, B. S.; Kohler, B. E. *Chemical Physics Letters* **1972**, *14*(3), 299–304.

[27] Tavan, P.; Schulten, K. *Physical Review B* **1987**, *36*(8), 4337–4358.

[28] Polivka, T.; Frank, H. A. *Accounts of chemical research* **2010**, *43*(8), 1125–1134.

[29] Gradinaru, C. C.; Kennis, J. T. M.; Papagiannakis, E.; van Stokkum, I. H. M.; Cogdell, R. J.; Fleming, G. R.; Niederman, R. A.; van Grondelle, R. *Proceedings of the National Academy of Sciences U.S.A.* **2001**, *98*(5), 2364–2369.

[30] Ostroumov, E.; Müller, M.; Marian, C.; Kleinschmidt, M.; Holzwarth, A. *Physical Review Letters* **2009**, *103*(10), 108302.

[31] Ostroumov, E. E.; Müller, M. G.; Reus, M.; Holzwarth, A. R. *The journal of physical chemistry. A* **2011**, *115*(16), 3698–712.

[32] Macernis, M.; Sulskus, J.; Malickaja, S.; Robert, B.; Valkunas, L. *The Journal of Physical Chemistry A* **2014**, *118*, 1817–1825.

[33] Di Donato, M.; Segado Centellas, M.; Lapini, A.; Lima, M.; Avila, F.; Santoro, F.; Cappelli, C.; Righini, R. *The Journal of Physical Chemistry B* **2014**, *118*(32), 9613–9630.

[34] Van Tassle, A. J. *Excited State Structural Dynamics of Carotenoids and Charge Transfer Systems* PhD thesis, University of California, Berkeley, **2006**.

[35] Pang, Y.; Jones, G. a.; Prantil, M. a.; Fleming, G. R. *Journal of the American Chemical Society* **2010**, *132*(7), 2264–73.

[36] Gaier, K.; Angerhofer, A.; Wolf, H. C. *Chemical Physics Letters* **1991**, *187*(1-2), 103–109.

[37] Andersson, P. O.; Bachilo, S. M.; Chen, R.-L.; Gillbro, T. *The Journal of Physical Chemistry* **1995**, *99*(44), 16199–16209.

[38] Frank, H. a.; Josue, J. S.; Bautista, J. a.; van der Hoef, I.; Jansen, F. J.; Lugtenburg, J.; Wiederrecht,

G.; Christensen, R. L. *The Journal of Physical Chemistry B* **2002**, *106*(8), 2083–2092.

[39] Bautista, J. A.; Connors, R. E.; Raju, B. B.; Hiller, R. G.; Sharples, F. P.; Gosztola, D.; Wasielewski, M. R.; Frank, H. A. *The Journal of Physical Chemistry B* **1999**, *103*, 8751–8758.

[40] Bautista, J. a.; Connors, R. E.; Raju, B. B.; Hiller, R. G.; Sharples, F. P.; Gosztola, D.; Wasielewski, M. R.; Frank, H. a. *The Journal of Physical Chemistry B* **1999**, *103*(41), 8751–8758.

[41] Frank, H. a.; Bautista, J. a.; Josue, J.; Pendon, Z.; Hiller, R. G.; Sharples, F. P.; Gosztola, D.; Wasielewski, M. R. *The Journal of Physical Chemistry B* **2000**, *104*(18), 4569–4577.

[42] Niedzwiedzki, D. M.; Kajikawa, T.; Aoki, K.; Katsumura, S.; Frank, H. a. *The journal of physical chemistry. B* **2013**, *117*(23), 6874–87.

[43] Polívka, T.; Kaligotla, S.; Chábera, P.; Frank, H. a. *Physical chemistry chemical physics : PCCP* **2011**, *13*(22), 10787–96.

[44] Enriquez, M. M.; Fuciman, M.; LaFountain, A. M.; Wagner, N. L.; Birge, R. R.; Frank, H. a. *The journal of physical chemistry. B* **2010**, *114*(38), 12416–26.

[45] Pang, Y.; Prantil, M. A.; Tassle, A. J. V.; Jones, G. A.; Fleming, G. R. *The Journal of Physical Chemistry B* **2009**, *113*, 13086–13095.

[46] Ehlers, F.; Wild, D. A.; Lenzer, T.; Oum, K. *The Journal of Physical Chemistry A* **2007**, *111*, 2257–2265.

[47] Kopczynski, M.; Ehlers, F.; Lenzer, T.; Oum, K. *The journal of physical chemistry. A* **2007**, *111*(25), 5370–81.

[48] Mimuro, M.; Nishimura, Y.; Nagashima, U.; Yamazaki, I.; Katoh, T. *Journal of Luminescence* **1992**, *51*, 1–10.

[49] Mimuro, M.; Nagashima, U.; Nagaoka, S.-i. *Chemical physics ...* **1992**, *191*(3), 219–224.

[50] Enriquez, M. M.; Hananoki, S.; Hasegawa, S.; Kajikawa, T.; Katsumura, S.; Wagner, N. L.; Birge, R. R.; Frank, H. a. *The journal of physical chemistry. B* **2012**, *116*(35), 10748–56.

[51] Wagner, N. L.; Greco, J. A.; Enriquez, M. M.; Frank, H. A.; Birge, R. R. *Biophysical Journal* **2013**, *104*(6), 1314–1325.

[52] Magdaong, N. M.; Niedzwiedzki, D. M.; Greco, J. a.; Liu, H.; Yano, K.; Kajikawa, T.; Sakaguchi, K.; Katsumura, S.; Birge, R. R.; Frank, H. a. *Chemical Physics Letters* **2014**, *593*, 132–139.

[53] Zigmantas, D.; Polívka, T.; Hiller, R. G.; Yartsev, A.; Sundström, V. *The Journal of Physical Chemistry A* **2001**, *105*(45), 10296–10306.

[54] Zigmantas, D.; Hiller, R. G.; Yartsev, A.; Sundstro, V. *The Journal of Physical Chemistry B* **2003**, *107*, 5339–5348.

[55] Kosumi, D.; Kajikawa, T.; Okumura, S.; Sugisaki, M.; Sakaguchi, K.; Katsumura, S.; Hashimoto, H. *The Journal of Physical Chemistry Letters* **2014**, *5*, 792–797.

[56] Zigmantas, D.; Hiller, R. G.; Sharples, F. P.; Frank, H. A.; Sundström, V.; Polivka, T. *Physical Chemistry Chemical Physics* **2004**, *6*, 3009–3016.

[57] Papagiannakis, E.; Larsen, D. S.; van Stokkum, I. H. M.; Vengris, M.; Hiller, R. G.; van Grondelle, R. *Biochemistry* **2004**, *43*(49), 15303–15309.

[58] Van Tassle, A. J.; Prantil, M. A.; Hiller, R. G.; Fleming, G. R. *Israel Journal of Chemistry* **2007**, *47*(1), 17–24.

[59] Pang, Y.; Fleming, G. R. *Physical chemistry chemical physics : PCCP* **2010**, *12*(25), 6782–6788.

[60] Kardaś, T. M.; Ratajska-Gadomska, B.; Lapini, A.; Ragnoni, E.; Righini, R.; Di Donato, M.; Foggi, P.;

Gadomski, W. *The Journal of Chemical Physics* **2014**, *140*(20), 204312.

[61] Noguchi, T.; Hayashi, H.; Tasumi, M.; Atkinson, G. H. *The Journal of Physical Chemistry* **1991**, *95*(15), 3167–3172.

[62] Kukura, P.; McCamant, D. W.; Mathies, R. A. *The Journal of Physical Chemistry A* **2004**, *108*(28), 5921–5925.

[63] Gentili, P. L.; Bussotti, L.; Ruzziconi, R.; Spizzichino, S.; Foggi, P. *The journal of physical chemistry. A* **2009**, *113*(52), 14650–6.

[64] Iagatti, A. *Charge and Energy Transfer in Complex Systems* PhD thesis, Università di Firenze, LENS, **2013**.

[65] Snellenburg, J. J.; Laptenok, S.; Seger, R.; Mullen, K. M.; van Stokkum, I. H. M. *Journal of Statistical Software* **2012**, *49*(3), 1–22.

[66] Mullen, K. M.; van Stokkum, I. H. M. *Journal of Statistical Software* **2007**, *18*(1), 1–5.

[67] van Stokkum, I. H. M.; Larsen, D. S.; van Grondelle, R. *Biochimica et biophysica acta* **2004**, *1657*(2-3), 82–104.

[68] Azzaroli, N.; Lapini, A.; Donato, M. D.; Dei, A.; Righini, R. *The Journal of Physical Chemistry B* **2013**, *117*, 15492–15502.

[69] Ragnoni, E.; Di Donato, M.; Iagatti, A.; Lapini, A.; Righini, R. *The Journal of Physical Chemistry B* **2014**.

[70] Hamm, P.; Lim, M.; Hochstrasser, R. M. *The Journal of Physical Chemistry B* **1998**, *102*, 6123–6138.

[71] Hausherr, M. *Development of an interferometer-based transient two-dimensional infrared Spectrometer* PhD thesis, University of Zurich, **2011**.

[72] Bredenbeck, J.; Helbing, J.; Behrendt, R.; Renner, C.; Moroder, L.; Wachtveitl, J.; Hamm, P. *The Journal of Physical Chemistry B* **2003**, *107*(33), 8654–8660.

[73] Bredenbeck, J.; Helbing, J.; Kolano, C.; Hamm, P. *Chemical Physics and Physical Chemistry* **2007**, *8*, 1747–1756.

[74] Bredenbeck, J.; Helbing, J.; Hamm, P. *Journal of the American Chemical Society* **2004**, *126*(4), 990–1.

[75] McCamant, D. W.; Kukura, P.; Mathies, R. A. *The Journal of Physical Chemistry A* **2003**, *107*(40), 8208–8214.

[76] Lee, S.-Y.; Zhang, D.; McCamant, D. W.; Kukura, P.; Mathies, R. a. *The Journal of Chemical Physics* **2004**, *121*(8), 3632–42.

[77] McCamant, D. W.; Kukura, P.; Yoon, S.; Mathies, R. a. *The Review of scientific instruments* **2004**, *75*(11), 4971–4980.

[78] Kukura, P.; McCamant, D. W.; Yoon, S.; Wandschneider, D. B.; Mathies, R. a. *Science* **2005**, *310*(5750), 1006–1009.

[79] Weigel, A.; Dobryakov, A.; Klaumünzer, B.; Sajadi, M.; Saalfrank, P.; Ernsting, N. P. *The journal of physical chemistry. B* **2011**, *115*(13), 3656–80.

[80] Smeigh, A. L.; Creelman, M.; Mathies, R. a.; McCusker, J. K. *Journal of the American Chemical Society* **2008**, *130*(43), 14105–7.

[81] Han, F.; Liu, W.; Fang, C. *Chemical Physics* **2013**, *422*, 204–219.

[82] Lee, D.; Albrecht, A. C. *A Unified View of Raman, Resonance Raman, and Fluorescence Spectroscopy (and their Analogues in Two-Photon Absorption) in Advances in Infrared and Raman Spectroscopy;* John Wiley & Sons, Inc.: Chichester, 1985.

[83] McHale, J. L. *Molecular Spectroscopy;* Prentice Hall: New Jersey, pearson ed ed., 1999.

[84] Pontecorvo, E.; Ferrante, C.; Elles, C. G.; Scopigno, T. *Optics express* **2013**, *21*(6), 6866–72.

[85] Dorfman, K. E.; Fingerhut, B. P.; Mukamel, S. *The Journal of chemical physics* **2013**, *139*(12), 124113.

[86] Ando, H.; Fingerhut, B. P.; Dorfman, K. E.; Biggs, J. D.; Mukamel, S. *Journal of the American Chemical Society* **2014**, *136*(42), 14801–10.

[87] Mallick, B.; Lakhsmanna, A.; Umapathy, S. *Journal of Raman Spectroscopy* **2011**, *42*(10), 1883–1890.

[88] Andersson, P. O.; Gillbro, T.; Ferguson, L.; Cogdell, R. J. *Photochemistry and Photobiology* **1991**, *54*, 353–360.

[89] Schlucker, S.; Szeghalmi, A.; Schmitt, M.; Popp, J.; Kiefer, W. *Journal of Raman Spectroscopy* **2003**, *34*(6), 413–419.

[90] McCamant, D. W.; Kim, J. E.; Mathies, R. A. *Journal of Physical Chemistry A* **2002**, *106*(25), 6030–6038.

[91] Durchan, M.; Fuciman, M.; Slouf, V.; Polívka, T. *The Journal of Physical Chemistry A* **2012**, *116*, 12330–12338.

[92] Niedzwiedzki, D.; Koscielecki, J. F.; Cong, H.; Sullivan, J. O.; Gibson, G. N.; Birge, R. R.; Frank, H. a. *The journal of physical chemistry. B* **2007**, *111*(21), 5984–98.

[93] Papagiannakis, E.; Kennis, J. T. M.; van Stokkum, I. H. M.; Cogdell, R. J.; van Grondelle, R. *Proceedings of the National Academy of Sciences of the United States of America* **2002**, *99*(9), 6017–6022.

[94] Papagiannakis, E.; van Stokkum, I. H. M.; Vengris, M.; Cogdell, R. J.; van Grondelle, R.; Larsen, D. S. *The journal of physical chemistry. B* **2006**, *110*(11), 5727–36.

[95] Bovi, D.; Mezzetti, A.; Vuilleumier, R.; Gaigeot, M.-P.; Chazallon, B.; Spezia, R.; Guidoni, L. *Physical chemistry chemical physics : PCCP* **2011**, *13*(47), 20954–64.

[96] Di Donato, M.; Ragnoni, E.; Lapini, A.; Foggi, P.; Hiller, R. G.; Righini, R. *The Journal of Chemical Physics submitted*.

[97] Jeffrey, S. W.; Wright, S. W. In *Phytoplankton pigments in oceanography.;* UNESCO: Paris, 1997; pages 327–360.

[98] Pinto, E.; Catalani, L. H.; Lopes, N. P.; Di Mascio, P.; Colepicolo, P. *Biochemical and Biophysical Research Communications* **2000**, *268*, 496–500.

[99] Dietzek, B.; Chábera, P.; Hanf, R.; Tschierlei, S.; Popp, J.; Pascher, T.; Yartsev, A.; Polívka, T. *Chemical Physics* **2010**, *373*(1-2), 129–136.

[100] Kish, E.; Mendes Pinto, M. M.; Bovi, D.; Basire, M.; Guidoni, L.; Vuilleumier, R.; Robert, B.; Spezia, R.; Mezzetti, A. *The journal of physical chemistry. B* **2014**, *118*(22), 5873–81.

[101] Edler, J.; Hamm, P. *The Journal of Chemical Physics* **2003**, *119*(5), 2709.

[102] Hamm, P.; Zanni, M. *Concept and Methods of 2D Infrared Spectroscopy;* Cambridge University Press: New York, 2011.

[103] Woutersen, S.; Mu, Y.; Stock, G.; Hamm, P. *Chemical Physics* **2001**, *266*, 137–147.

[104] Barth, A.; Zscherp, C. *Quarterly Reviews of Biophysics* **2002**, *35*(4), 369–430.

[105] Candelaresi, M.; Pagliai, M.; Lima, M.; Righini, R. *The journal of physical chemistry. A* **2009**, *113*(46), 12783–90.

[106] Wotiz, J. H.; Mancuso, D. E. *Journal of Organic Chemistry* **1957**, *22*(February), 207–211.

[107] Papagiannakis, E.; Vengris, M.; Larsen, D. S.; Stokkum, I. H. M. V.; Hiller, R. G.; Grondelle, R. V.

The Journal of Physical Chemistry B **2006**, *110*(512), 512–521.

[108] Niedzwiedzki, D. M.; Chatterjee, N.; Enriquez, M. M.; Kajikawa, T.; Hasegawa, S.; Katsumura, S.; Frank, H. a. *The journal of physical chemistry. B* **2009**, *113*(41), 13604–12.

[109] Mimuro, M.; Nishimura, Y.; Takaichi, S.; Yamano, Y. *Chemical Physics Letters* **1993**, *213*(5-6), 1–5.

[110] Knecht, S.; Marian, C. M.; Kongsted, J.; Mennucci, B. *The journal of physical chemistry. B* **2013**, *117*(44), 13808–13815.

[111] Orlandi, G.; Zerbetto, F. *Chemical Physics* **1986**, *108*, 187–195.

[112] Schulten, K.; Karplus, M. *Chemical Physics Letters* **1972**, *14*, 305–309.

[113] Schulten, K.; Ohmine, I.; Karplus, M. *The Journal of Chemical Physics* **1976**, *64*, 4422–4441.

[114] Orlandi, G.; Zerbetto, F.; Zgierski, M. Z. *Chemical reviews* **1991**, *91*, 867–891.

[115] Shima, S.; Ilagan, R. P.; Gillespie, N.; Sommer, B. J.; Hiller, R. G.; Sharples, F. P.; Frank, H. A.; Birge, R. R. *The Journal of Physical Chemistry A* **2003**, *107*, 8052–8066.

[116] Coccia, E.; Varsano, D.; Guidoni, L. *Journal of Chemical Theory and Computation* **2014**, *10*, 501–506.

[117] Kleima, F. J.; Wendling, M.; Hofmann, E.; Peterman, E. J. G.; Grondelle, R. V.; Amerongen, H. V. *Biochemistry* **2000**, *39*, 5184–5195.

[118] Damjanovic, A.; Ritz, T.; Schulten, K. *Biophysical Journal* **2000**, *79*, 1695–1705.